Development of Multimodal Spectroscopy for the Detection of Vulnerable Atherosclerotic Plaques

by

Obrad R. Šćepanović

Submitted to the Department of Electrical Engineering and Computer Science
in partial fulfillment of the requirements for the degree of

Doctor of Philosophy in Electrical Engineering and Computer Science

at the

MASSACHUSETTS INSTITUTE OF TECHNOLOGY

June 2008

Author .....
Department of Electrical Engineering and Computer Science
May 14, 2008

Certified by .....
Michael S. Feld
Professor of Physics and Director of G. R. Harrison Spectroscopy Laboratory
Thesis Supervisor

Accepted by ...
Terry P. Orlando
Chairman, Department Committee on Graduate Students

Development of Multimodal Spectroscopy for the Detection of Vulnerable Atherosclerotic Plaques

by

Obrad R. Šćepanović

Submitted to the Department of Electrical Engineering and Computer Science
on May 14, 2008, in partial fulfillment of the
requirements for the degree of
Doctor of Philosophy in Electrical Engineering and Computer Science

Abstract

The combination of reflectance, fluorescence, and Raman spectroscopy - which is termed multimodal spectroscopy (MMS) - provides complementary and depth-sensitive information about tissue composition. As such, MMS can provide biochemical and morphological information useful in detecting vulnerable atherosclerotic plaques, that is, plaques most prone to rupture and causing sudden death. Early detection of these vulnerable plaques is critical to reducing patient mortality associated with cardiovascular disease. In developing MMS into a clinical diagnostic modality, several scientific and engineering directions are explored in this work: the physical motivation for MMS, the framework of quantitative extraction of spectral parameters, the spectral probes that enable the efficient collection of data, a clinical instrument able to provide real-time diagnosis, and, finally, a clinical implementation of the entire methodology. The motivation for MMS is shown through a pilot *in vitro* study using carotid artery specimens, which shows the promise for MMS to detect features of vulnerable plaque. Having established the motivation, the next step describes the mathematical tools used to extract quantitative spectral parameters and, moreover, to assess the uncertainty and confidence of the spectral information. In order to implement MMS, the development of an efficient, specialized MMS probe for data acquisition and a compact and practical clinical MMS instrument are described. Lastly, *in vivo* and *ex vivo* results from a relatively large clinical study of vulnerable plaque in humans show excellent agreement between MMS and histopathology. Specifically, MMS is shown to have the ability to detect a thin fibrous cap, necrotic core or superficial foam cells, and thrombus. In addition, these studies show that vulnerable plaques could be detected with a cross validated sensitivity of 89-96%, specificity of 72-78%, and a negative predictive value of 89-97%. These very encouraging results serve as an important step in bringing MMS into the clinical arena as a powerful diagnostic technique.

Thesis Supervisor: Michael S. Feld
Title: Professor of Physics and Director of G. R. Harrison Spectroscopy Laboratory

Acknowledgments

This research and achievements would not have been possible without the help and support of my advisors, colleagues, friends, and family.

First and foremost, I am indebted to my advisor, Prof. Michael Feld, for his vision, guidance, and for never avoiding to ask the hard questions. Michael, thank you for pushing me when I needed it and, at other times, for giving me the space to work things out on my own. You really are a true believer in spectroscopy and I will buy a used car from you any day. I would also like to thank Dr. Ramachandra Dasari for teaching me how to deal with technical problems and how to negotiate. Ramachandra, thank you for always having your office door open when I needed to talk.

I thank the members of my thesis committee, Prof. Roger Mark, Prof. George Verghese, and Prof. Kamran Badizadegan, for providing helpful comments and insights that have strengthened my research. Prof. Mark, I also thank you for opening my eyes to leadership opportunities and pushing me to fully realize myself both in academic and extracurricular circles; you have been like a second father to me.

I thank all of my colleagues, past and present, at the Spec Lab for being supportive and helpful: George Angheloiu, Samir Awasthi, Ishan Barman, Kate Bechtel, Luis Galindo, Saumil Gandhi, Joseph Gardecki, Abigail Haka, Chae-Ryon Kong, Condon Lau, Sasha McGee, Jelena Mirković, Jason Motz, Jonathan Nazemi, Wei-Chuan Shih, Gajendra Singh, and Zoya Volynskaya. Zoya, thanks for putting up with my eccentric personality for all these years and being a great office mate. Chae-Ryon, I owe you one for waking up at crazy hours to go to the hospital with me. Kate, thanks for rubbing off on me your perfection-oriented attitude about research and standards of quality. I am also grateful to Dr. Maryann Fitzmaurice for being a wonderful collaborator and teacher. Maryann, you taught me to how to make sense out of complicated data and never give

up hope. I thank Dr. Arnold Miller for enabling our clinical research and Dr. John Kramer for his clinical and scientific guidance. In addition, I thank all my friends for support, particularly my first lab partner, Ali Motamedi. Babba, it all started with the "giant laser" and you've been my older brother ever since.

My brother, Danilo, has been my biggest inspiration of diligence and scientific pursuit. Brate, I'm not just thanking you for *fig2num2.m* or *endnoteToBib.m* or logistic regression, but your entire attitude toward learning which truly motivated me. I thank my best friend, Sourav Dey, for teaching me math and using his energy to excite me about research. Suresh, it all started when we went to India together and I wouldn't have gotten through grad school without you; sorry I Indoed you about Utah. My girlfriend, Azra Pravdić, has been my confidant and pillar of support through the thick and thin of grad school, life, and love. Maleno, thanks for always being there for me.

Finally, I thank my whole family and especially my loving parents, Bojana and Ranko, for supporting me fully in all of my life pursuits.

Funding for this work has been generously provided by the National Institutes of Health and the Lester Wolfe fellowship.

Contents

List of Figures

List of Tables

Chapter 1

Introduction

In this work, we propose a minimally-invasive spectroscopic approach to disease diagnosis, particularly to the detection of vulnerable atherosclerotic plaques. The spectroscopic approach utilizes the information provided by different spectral modalities, together with robust interpretation of data, and the development of appropriate instrumentation and probes that demonstrate the clinical viability of the methodology.

1.1 Disease diagnosis

Spectroscopy provides a powerful means to obtaining quantitative chemical and morphological information about tissue that is critical to disease diagnosis. To illustrate the methodology in this work, we will focus on the application of diagnosing atherosclerosis and, more specifically, detecting vulnerable plaques. However, the ideas, technology, and methods are more generally applicable to studying the progression and severity of other diseases such as cancer.

1.1.1 Atherosclerosis

Significance

Cardiovascular disease is the leading cause of death in the nation despite significant resources allocated for improved diagnosis and treatment. The current prevalence of cardiovascular disease

in the United States is 79.4 million. Mortality due to cardiovascular diseases represented 36.3% of total mortality in 2004, a number almost double that of cancer, the second leading cause of death. The direct and indirects costs associated with cardiovascular disease were estimated to be $432 billion in 2007 [1] and continue to rise. It is predicted that by 2020 cardiovascular disease will surpass infectious disease to become the leading cause of death worldwide [2].

Atherosclerosis accounts for the vast majority of cardiovascular morbidity and mortality. It is a systemic disease, but the most common sites are the coronary, carotid and superficial femoral arteries and subrenal aorta. Atherosclerotic coronary artery disease (CAD) accounts for the majority of acute ischemic coronary syndromes, such as sudden cardiac death, acute myocardial infarction and unstable angina. As such, it is responsible for approximately 450,000 deaths per year, which translates into one American dying of myocardial infarction caused by CAD every minute [1]. In addition, atherosclerosis involving the carotid and femoral arteries is also a major cause of stroke, accounting for 270,000 deaths in 2002, and peripheral vascular disease such as gangrene, respectively [1].

Anatomy

Three concentric layers comprise the artery wall: the intima, media, and adventitia. In normal arteries, the intima measures between 50 and 300 μm in thickness and is composed of endothelial cells threaded with collagen and elastin fibers, and some proteoglycans. The endothelium bounds the arterial lumen and furnishes several functions, which include providing a smooth surface for blood flow, producing extracellular matrix components, expressing factors which inhibit blood coagulation, and controlling the passage of materials into and out of the bloodstream [3]. It is *endothelial dysfunction*, or the loss of proper endothelial function, that ultimately leads to atherosclerosis. In

a diseased artery, the intima produces an extracellular network of fibrillar proteins that comprise a fibrous cap, which is predominantly composed of collagen. The dense internal elastic lamina separates the intima from the media. The media of large elastic arteries, such as the aorta and carotids, is primarily composed of elastin fibers and some smooth muscle cells, which enable these vessels to to respond to highly pulsatile blood flow. In medium-sized muscular arteries, which include coronaries, the media contains more smooth muscle cells that control blood flow through vasoconstriction and vasodilation. The media and adventitia are separated by the external elastic lamina. The outermost adventitial layer contains a network of connective tissue along with adipocytes, nerve fibers, and vasa vasorum in the case of larger vessels.

Pathology

In atherosclerosis, arterial luminal obstruction is caused by the development of plaque, which typically progresses slowly over several decades. The initial phases of plaque formation are characterized by lipoprotein infiltration of the intima, followed by recruitment of leukocytes, especially monocytes, on the luminal surface of the dysfunctional endothelium, and migration of these cells to the intima through the mediation of cytokines such as monocyte chemoattractant protein-1. Once inside the intima, the monocytes engulf lipoproteins, express scavenger A and CD36 receptors that accelerate the process of lipid endocytosis, and turn into foam cells (FC) under the influence of mediators such as macrophage colony-stimulating factor [4]. Simultaneously, smooth muscle cells (SMC) migrate from the media to the intima and proliferate locally, while FCs are degraded by apoptosis, contributing to the formation of a necrotic core (NC) [5]. Smooth muscle cells subsequently lay down elements of the extracellular matrix such as collagen and proteoglycans, which form a fibrous cap covering the NC. A balance between the production and degradation of collagen

in the fibrous cap is regulated by molecules such as INF-γ and matrix metalloproteinases (MMP-1, -2, -8, -9, -13) [6]. Under certain circumstances collagen breakdown prevails, followed by thinning, fissuring and eventual rupture of the fibrous cap. In addition, the plaque can undergo dystrophic mineralization through the deposition of calcium salts [7].

■ 1.1.2 Vulnerable plaque

The severity of atherosclerotic lesions has traditionally been assessed by imaging their location and percentage of intraluminal stenosis. However, landmark studies over the past 10 years have shown that up to 70% of acute cardiac ischemic events results from the rupture of previously sub-symptomatic lesions, ending in thrombotic occlusion and, often, myocardial infarction [8, 9]. The vast majority of these thrombosed coronary artery plaques exhibit less than 75% stenosis [10], the figure often used to define a clinically significant lesion. Thus, plaques that are not critically stenotic can still cause acute ischemic events [11, 12].

These *vulnerable plaques* (also known as *culprit* or *unstable* plaques) often exhibit rupture of a so-called thin cap fibrous atheroma: i.e. a plaque with a thin (< 65 μm) fibrous cap overlying a large (> 2 mm) necrotic core [10]. A recent consensus paper by cardiovascular pathologists [13, 14] has reported that additional morphological features may be associated with thrombosis, such as erosion or denudation of the intimal endothelial layer. In both ruptured and eroded plaques, the fibrous cap [9, 10] or superficial intima [12] is frequently infiltrated by inflammatory cells, most often macrophages and foam cells. Exposed calcifications [10] and acute intraplaque hemorrhage or dissection [9, 15, 16] are other common features of thrombosed plaques. In addition, the presence of a non-occlusive intraluminal thrombus from a previous plaque rupture is another feature of vulnerability as it leaves the plaque prone to subsequent thrombosis [17, 13]. Figure 1-1 shows the

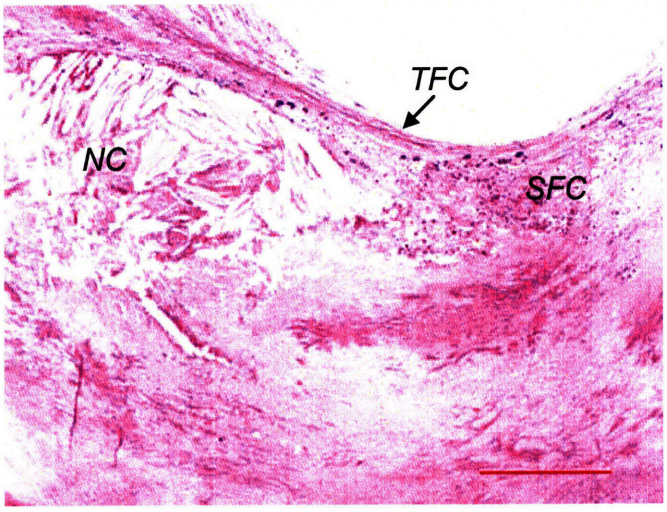

Figure 1-1. Morphologic features of a vulnerable carotid plaque. Thin fibrous cap (TFC), necrotic core (NC) and superficial foam cells (SFC) are indicated. Hematoxylin and eosin stain. The scale bar indicates a 1 mm length.

histology of a carotid artery that exhibits features of a prototypical vulnerable plaque. The diseased intima is separated from the lumen by only a thin fibrous cap, and there is a large cholesterol-rich NC and many superficial foam cells (SFC).

At present, there does not exist a scheme for assessing the relative vulnerability of different lesions. To address this limitation, a quantitative approach to ranking plaque vulnerability, called the vulnerable plaque index, is proposed in Sec. 6.2.4.

■ 1.1.3 Competing technologies

There is currently great interest in developing new techniques for clinical detection and imaging of vulnerable plaque. These include x-ray angiography, angioscopy, intravascular ultrasound (IVUS), thermography, nuclear magnetic resonance imaging (MRI), computed tomography (CT), optical coherence tomography (OCT), nonlinear optical microscopy, and optical spectroscopy [18]. A brief summary of each is given below.

X-ray angiography

X-ray angiography, the gold standard for diagnosing atherosclerosis, uses x-ray transmission to image vessel narrowing and blood flow. Contrast is obtained by injecting a radio-opaque medium into the artery lumen. This technique can quantify the severity of stenosis and identify occlusive thrombi and dense calcifications. However, it is unable to identify the marginally stenotic vulnerable plaques that give rise to the majority of acute ischemic events [19, 20, 21, 22, 23].

Angioscopy

Although not commonly used in general practice in this country, angioscopy has been widely applied for evaluation of coronary atherosclerosis outside the United States [24, 25]. By visualizing the arterial surface with white light illumination through a miniature endoscope ("angioscope"), atherosclerotic plaques and surface complications such as rupture and thrombosis can be identified. However, angioscopy cannot probe subsurface changes such as the thinning of the fibrous cap that are critical to identifying vulnerable plaque before rupture or thrombosis has occurred, nor can it provide chemical information about lesion composition [20, 26, 27].

Intravascular ultrasound (IVUS)

IVUS overcomes some of the limitations of angiography and angioscopy [28, 19, 29, 30, 31, 32, 33]. Relying on changes in tissue density, that affect the reflection of sound waves, IVUS can image several features of subsurface plaque architecture, such as fibrous cap thickness and NC depth. However, other key features, such as the presence of inflammation or SFCs, cannot be assessed. Again, this technique cannot provide chemical information. Interestingly, IVUS is frequently used as a reference to evaluate pilot studies for new imaging technologies. For example, comparisons

with IVUS have been made to validate studies using Raman spectroscopy and OCT for arterial imaging [34, 35].

Thermography

Thermography, one of the few imaging techniques specifically targeted to vulnerable atherosclerotic plaques, is based on detection of heat released by inflammatory cells within vulnerable plaque. This technique is still in early stage development [36, 37].

Nuclear magnetic resonance imaging (MRI)

MRI uses radio waves to induce spin flips of (water molecule) protons in a tissue sample placed in a high magnetic field. By applying a spatial field gradient, changes in tissue density can be imaged. Although, in principle, MRI can provide chemical information (by targeting nuclei other than water), in practice this is not feasible because of the relatively low concentrations of other molecules, which translates into inadequate sensitivity. Thus, conventional MRI produces only anatomical images. As with IVUS, MRI angiography has been used to distinguish features of atherosclerotic plaque such as fibrous cap and NC in human cadaveric carotid endarterectomy specimens [38] and patients undergoing carotid endarterectomy [39]. Recent studies indicate that MRI can identify thrombus [40] and intraplaque hemorrhage [41, 42] in carotid arteries. However, imaging coronary arteries has proven to be more difficult, because of cardiac and respiratory motion. New black-blood, contrast-enhanced breath-holding and free-breathing respiratory-gated MRI techniques may help overcome these limitations [43]. However, because of the small caliber and tortuosity of coronary vessels and their close proximity to other cardiac structures, adequate spatial resolution cannot be achieved without the use of extremely high magnetic fields [44]. Recently developed intravascular MRI techniques may provide the spatial resolution required for imaging coronary atherosclerosis

[45, 46].

Computed tomography (CT)

Similar advances have been made in CT imaging of atherosclerosis. Multi-slice spiral CT is a high resolution imaging technique that has recently been applied to anatomic imaging of atherosclerotic plaque in the coronary, carotid and peripheral arteries [47]. Cardiac motion is still a problem but may be overcome by means of electrocardiographic gating. Ultrafast electron beam computed tomography (EBCT) has improved spatial resolution. However, it can only detect calcifications, and thus is blind to non-calcified plaques [12, 48, 49, 50]. As with the other more conventional imaging techniques, it cannot assess key features of vulnerable plaques.

Optical coherence tomography (OCT)

OCT is a promising technique actively being investigated for vascular imaging [51, 52]. It uses singly back-scattered light to obtain subsurface images as a function of depth. Similar to IVUS, which relies on density changes in the vessel wall, OCT relies on changes in refractive index. However, since OCT employs light rather than sound, images with much higher spatial resolution can be achieved, on the order of 10 μm. OCT has been applied successfully *in vivo* [53] and has shown the promising potential to detect key markers of vulnerable plaque including a thin fibrous cap [54, 53], macrophages [55, 56], calcium nodules [54], and thrombus [35]. However, OCT does not provide chemical information.

Nonlinear optical microscopy

Recently, nonlinear optical microscopy techniques have emerged as means to perform 3-D imaging of tissues, including artery tissue. These nonlinear techniques include two-photon excited fluo-

rescence (TPEF), second-harmonic generation (SHG), and coherent anti-Stokes Raman scattering (CARS). TPEF can be used to provide images of elastin fibers (as well as collagen and cellular components), SHG microscopy can probe collagen fibrils, while CARS is particularly sensitive to lipid-rich structures. Several studies have reported using nonlinear optical microscopy to provide high resolution images of human arteries and thus serve to assess the vulnerability of plaque morphology [57, 58]. However, as much as these imaging techniques may eventually replace histology, their feasibility as *in vivo* intravascular modalities is yet to be demonstrated. In addition, these techniques are most promising when they utilize sources of exogenous contrast, which have their own disadvantages.

Optical spectroscopy

Optical spectroscopy is also being studied for evaluation of these critical lesions. Several groups have explored the use of near-infrared spectroscopy (1-2.4 μm) to characterize atherosclerotic plaque, [59, 60], with a recent paper reporting promising results in detecting markers of plaque vulnerability such as a thin fibrous cap, lipid pools, and inflammation [61]. A commercial device using near-infrared spectroscopy has recently obtained FDA approval for intravascular imaging of coronary arteries [62]. In this wavelength range, absorption is due to molecular overtone/combination vibrations and can provide information about tissue composition. This technique is attractive because of the large signals and potentially low cost of the instruments. However, the spectral features are broad and overlapping, which decreases predictive ability. Further, water absorption in this wavelength range can distort the spectral features and reduce sampling depth to well below the intimal thickness.

Other spectroscopic techniques, including [ultraviolet-visible] diffuse reflectance, fluorescence, and Raman spectroscopy, being the subject of the present work, are discussed more thoroughly in

the next section.

1.2 Optical properties and spectroscopy

When light interacts with tissue, several physical processes determine how the incident energy is transformed. Some of the light is elastically scattered, either one or many times, before returning to the surface. During this process, some portion of the light may be absorbed by the endogenous absorbers in the tissue, while a portion of the absorbed light may be remitted as fluorescence after interacting with native fluorophores. Lastly, a small fraction of the light can be inelastically scattered through a molecule-specific process called Raman scattering. We now discuss reflectance, fluorescence, and Raman scattering in more detail.

1.2.1 Reflectance

Using diffuse reflectance spectroscopy (DRS), we study the spectrum of near UV-visible light (300 - 700 nm) traversing turbid biological tissue. The resulting spectrum exhibits features due to scattering and absorption of the incident light by the tissue. In atherosclerotic plaque, the structures that account for scattering are the morphological components such as foam cells, collagen matrix, and other structures that spatially vary the index of refraction. The main absorbers are hemoglobin, associated with thrombus or acute intraplaque hemorrhage, and β-carotene, whose absorption has been used previously for spectroscopic detection of atherosclerosis [63, 64]. A recent study of reflectance, in the extended range of 400 to 1700 nm, perhaps overcomes some of the mentioned shortcomings of near-infrared spectroscopy; the said study reported promising results in detecting a large lipid core in plaques, a key feature of vulnerability, using the contributions of β-carotene and hemoglobin [65].

In our laboratory, we have previously developed a model to analyze DRS spectra based on an analytical expression for diffusion of multiply-scattered light [66]. This expression is an appropriate simplification of a well established formula for diffuse reflectance developed by Farrell *et al.*, who calculated the diffuse reflectance from a narrow beam of light incident on the surface of a semi-infinite turbid medium under the diffusion approximation [67]. This modeling and analysis enables the extraction of the wavelength-dependent coefficients of scattering (μ_s') and absorption (μ_a). The *reduced scattering coefficient* μ_s' characterizes the scattering properties of tissue by specifying the number of scattering events that light would, on average, undergo as it traverses the medium, and it takes into account the anisotropy [68]. The *absorption coefficient* μ_a characterizes the absorbers in the tissue by specifying the average number of absorption events that would occur [68]. The diffusion approximation, which is used here, assumes that scattering dominates over absorption, $\mu_s' >> \mu_a$. A more detailed description of DRS modeling can be found in Sec. 4.3.1.

■ 1.2.2 Fluorescence

Fluorescence spectroscopy relies on the excitation of molecular electronic energy levels, giving rise to re-emission at wavelengths longer than the exciting light. The spectrum of the emitted light provides information about the fluorescing molecule (fluorophore). In addition, the emission spectrum can vary with excitation wavelength, providing additional molecular information. The primary fluorophores in arterial tissue are elastin, collagen, tryptophan, ceroid [69] and oxidized low density lipoprotein [70]. A number of research groups, including our own, have employed continuous wave [71, 72, 73], and time-resolved [74, 75] fluorescence spectroscopy to diagnose atherosclerosis, including the detection of a thin fibrous cap [70], lipid-rich lesions [76], disruption [77], and macrophages [78].

However, the broad overlapping spectral features of tissue fluorophores, further confounded by absorption and scattering, are a barrier to extracting spectral information with sufficient accuracy for quantitative analysis of vulnerable plaque. One recent study using fluorescence showed promising results in identifying thin fibrous cap atheromas, but a number of samples had to be eliminated from the analysis due to the inability to compensate for the spectral distortions caused by scattering and absorption [70]. Our laboratory has previously developed a method to remove these distortions using the information from the DRS spectrum, and thus extract the intrinsic fluorescence [79, 80], which can be decomposed into a linear combination of the spectra from fluorophores associated with morphological structures in the tissue. Intrinsic fluorescence spectroscopy (IFS) has been successfully employed in our laboratory for cancer diagnosis [81, 82]. A more detailed description of IFS modeling can be found in Sec. 4.3.2.

■ 1.2.3 Raman scattering

Raman spectroscopy detects molecules by exciting vibrations amongst bonds which are unique to each molecule, and has been used extensively in biomedicine [83, 84]. Raman spectroscopy is based on a scattering process in which monochromatic light incident on a sample sets the molecules into vibration. The vibrating molecule takes away a small amount of the incident photon energy, shifting the scattered light to lower frequency (i.e. longer wavelength). This frequency shift, usually measured in wave numbers (cm^{-1}), is equal to the molecular vibration frequency. As biological molecules have a number of vibrations, each with characteristic frequency and Raman scattering cross section, the Raman spectrum of a given molecule has a unique pattern. Raman signals are weak, and thus care is required to efficiently collect and optimize them. Note that, unlike fluorescence, the Raman spectrum manifests itself as shifts in frequency from that of the excitation

light frequency. Previous work by our group on Raman spectroscopy of atherosclerosis identified eight key morphological components in arterial pathogenesis that could be identified by their Raman spectral signatures: collagen fibers (CF), cholesterol crystals (CC), calcium mineralization (CM), elastic lamina (EL), adventitial adipocytes (AA), foam cells/necrotic core (FC/NC), beta-carotene crystals (β-CC), and smooth muscle cells (SMC)[85]. A diagnostic algorithm, using morphological information extracted with a linear combination model similar to that used for IFS, was able to classify *in vitro* coronary artery specimens as non-atherosclerotic, non-calcified plaque and calcified plaque with 94% accuracy [86]. The development of a small-diameter, high-throughput, filtered Raman probe [87] has resulted in the first *in vivo* clinical application of the Raman spectroscopy diagnostic algorithm in real-time [88] during carotid endarterectomy and femoral bypass surgeries [89].

1.3 MMS

One of the goals of the present work is to explore the diagnostic power of DRS, IFS and Raman spectroscopy together, which we term multimodal spectroscopy (MMS). The advantages of MMS are two-fold. First, MMS yields complementary biochemical and morphological information about arterial tissue that no individual modality can provide by itself. Second, the information obtained by these modalities is depth-sensitive, due to the inherently different tissue penetration by the various incident wavelengths employed.

1.3.1 Complementarity

The complementary tissue information that can be obtained from MMS is the following. DRS provides information about tissue scattering and absorption, as mentioned earlier, and allows for

the assessment of tissue turbidity. Scattering is indicative of the presence of index varying structures such as foam cells/macrophages while hemoglobin absorption provides information about the presence of blood, clotting, or hemorrhage. DRS is also critical in extracting the IFS signal from fluorescence, which provides relative amounts of tissue fluorophores that are present such as collagen, elastin, and low-density lipoprotein (LDL). Raman spectroscopy is very molecule specific and is particularly useful in identifying highly Raman active components such as calcification as well as necrotic core and foam cells. Taken together, the three modalities provides a more complete picture of the tissue state. There are also areas where some modalities overlap and this common information can be used to make the algorithms more robust. For example, both IFS and Raman spectroscopy can detect collagen, while both DRS and Raman are sensitive to hemoglobin.

■ 1.3.2 Depth sensing

The depth-sensing aspect of MMS comes from the relationship between tissue turbidity and wavelength. For IFS, typical wavelengths that are used are in the ultraviolet, such as 308 nm and 340 nm excitation. DRS uses the broad visible spectrum 400-700 nm while Raman spectroscopy uses near-infrared 830 nm excitation. Thus MMS information is spanned over a relatively large range of wavelengths, over which tissue properties vary significantly. In Fig. 1-2, the absorption coefficient μ_a and the reduced scattering coefficient $\mu_s^{'}$ of artery tissue are given in this range of wavelengths, obtained from data published by Keijzer *et al.* [90]. It is evident that both scattering and absorption decrease with increasing wavelength and thus artery tissue, as with most other tissues, is optically more transparent at longer wavelengths. Subsequently, the penetration depth of different wavelengths in artery tissue will increase with wavelength. As a result, the IFS will assess information at the most superficial level, DRS provides information at an intermediate depth, while

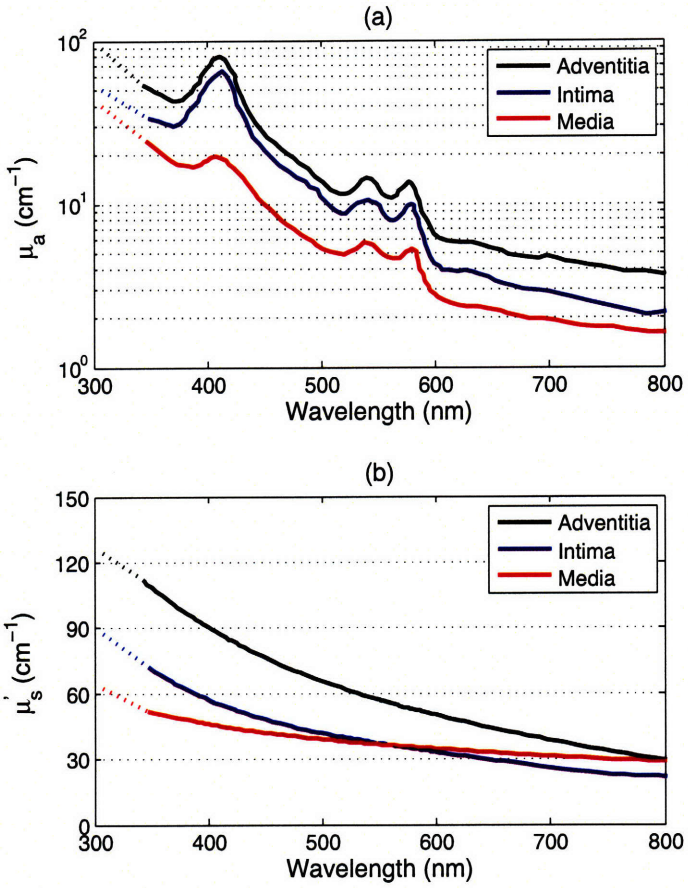

Figure 1-2. The optical properties of arterial tissue on 340-800 nm. Top graph in (a) shows the absorption coefficient μ_a and (b) shows the reduced scattering coefficient μ_s'.

Raman spectroscopy samples deepest in artery tissue. A more detailed and quantitative discussion of sampling depths is given in Sec. 2.2.1.

■ 1.4 Data analysis

Real-time analysis of spectroscopic measurements is essential in many applications, including pharmacokinetics [91], bioreactor monitoring [92], and medical diagnosis [93]. In our laboratory [94, 89] and others [95, 96], real-time analysis of spectroscopic measurements acquired *in vivo* is under study

to provide clinicians with immediate diagnoses, in lieu of histopathology. In medical applications, the confidence in the measurement of a particular diagnostic parameter can affect the course of disease management, with ramifications to the health of the patient. The uncertainties and the associated confidence intervals of the parameters extracted from spectroscopic measurements serve to assess the accuracy, stability, and diagnostic value of the data. The importance of uncertainty is related to other figures of merit commonly mentioned in the chemometrics field: signal-to-noise ratio, precision, limit of detection, sensitivity, error propagation and selectivity [97, 98]. Note that measurement uncertainty (precision) is different from measurement accuracy.

The most effective way to extract quantitative information from spectral data in a linear system is by utilizing the full spectrum (multivariate analysis) [99]. In this formalism, a spectrum, a series of intensity values at different wavelengths, is mathematically represented as a vector. Consider, for example, measurement of the concentration of a particular species or analyte. This requires a model that, when applied to a measured spectrum, yields the concentration of interest. In most cases, the model can be conveniently expressed in terms of a regression spectrum or "b-vector" for a particular analyte; the analyte concentration (c_k) of a prediction sample can then be expressed as the inner product of the measured spectrum ($\mathbf{s}$) and the analyte-specific b-vector ($\mathbf{b}_k$):

$$c_k = \mathbf{b}_k^T \mathbf{s}. \tag{1.1}$$

When all of the chemical components are known, the model can be based on the constituent spectra, measured directly, and ordinary least squares (OLS) analysis can be applied, yielding a b-vector for every component of interest. If the spectra cannot be measured directly, or if one or more components are not known, a calibration step is required to generate the b-vectors, and a direct

calibration scheme such as classical least squares (CLS) or indirect calibration schemes such as partial least squares (PLS) or principal components regression (PCR) can be used. The calibration step requires a set of spectra with reference concentrations of the analyte(s) of interest. Similar approaches can be used to measure parameters extracted from biological tissue spectra that are used in disease diagnosis [100, 85]. A concept closely related to the b-vector is the net analyte signal (NAS), introduced by Lorber [101], which is the portion of the signal for each analyte that is orthogonal to the other analyte spectra. The NAS is also useful in evaluating the figures of merit mentioned earlier [102].

In principle, one can evaluate the parameter uncertainty by repeating the measurement many times and analyzing the standard deviation of parameters extracted from each of these multiple measurements; however, this is not practical for applications such as medical diagnosis, in which only one or a few measurements can be acquired. Alternatively, one can use chi-squared (χ^2) analysis to calculate parameter uncertainties extracted from a single spectrum [103]. χ^2 analysis is a very useful technique, but it is statistical rather than analytical and provides little insight into the origins of uncertainty.

In addition, various research groups have worked on deriving analytical expressions for uncertainty. Lorber and Kowalski have presented a complete and elegant treatment of error propagation associated with multivariate calibration. They derived a prediction error (uncertainty) formula that depends on the noise in the spectrum of the prediction sample and the spectra and concentrations of the analyte of interest in the calibration set. The formula was successfully tested on near-infrared reflectance data analyzed by PCR [104]. One practical shortcoming of the formula is its complexity and the difficulty in readily applying it to experimental data. Other groups have taken similar approaches to error analysis [105, 106, 107]. One of the goals of the present work is

to develop a simple analytical expression for characterizing uncertainty that can be expressed in terms of physically relevant and understandable parameters and be practically useful for real-time data analysis.

1.5 Instrumentation and probes

There has been extensive work, in our group and others, in the areas of instrumentation and probe development relative to the different spectral modalities comprising MMS [108]. This section is broken down into two subsections, the first on previous reflectance/fluorescence instrumentation and the second on previous Raman instrumentation, as the two techniques have been pursued separately in the past. One of the goals of the present work is to develop an integrated clinical MMS instrument that could be used to collect data with a single MMS probe.

1.5.1 Reflectance/fluorescence instrumentation and probes

Our laboratory has previously developed a portable clinical instrument to collect fluorescence and reflectance spectra called the FastEEM, for fast excitation-emission matrix (EEM) [109, 110, 111]. A fluorescence EEM is produced by means of a rotating wheel containing laser dyes, pumped by a 308 nm XeCl excimer laser, which generates nine laser pulses at excitation wavelengths ranging from 340 to 500 nm which, including the 308 nm pulses, provides ten laser excitation wavelengths in all. In addition, a Xenon flash lamp produces white light pulses for reflectance. This light is delivered to the tissue via a thin, flexible optical fiber probe that contains a ring of six collection fibers surrounding a single delivery fiber. Spectra are collected with the probe tip in contact with the tissue. The probe tip contains a cylindrical quartz shield shield that provides a well-defined delivery-collection geometry for spectral data acquisition [112], and its length is chosen to

provide substantial overlap between the delivered light spot and the field of view of the collection fibers. Return light from the tissue is transmitted by the collection fibers to a spectrograph/CCD detector for analysis. A rotating filter wheel in the collection beam path, synchronized to the laser excitation pulses, prevents scattered excitation light from entering the spectrograph. Delivery of all 11 excitation light pulses and collection of the resulting 11 emission/reflectance spectra is accomplished in a fraction of a second, and data analysis is performed in real time (2-3 s). Our laboratory has used the FastEEM in clinical settings to collect DRS and IFS spectra for diagnosis of dysplasia in the esophagus, cervix and oral cavity [81, 82, 113].

■ 1.5.2 Raman instrumentation and probes

Clinical applications of Raman spectroscopy have been impeded by the lack of suitable optical fiber probes. In recent years, our laboratory has developed an efficient optical fiber Raman probe [87] that can be used together with a compact clinical Raman instrument capable of real-time application [88]. The instrument uses an 830 nm diode laser, delivered through the probe, to excite Raman scattering. The probe delivers to and collects light with the probe tip in contact with tissue. Conventional fluorescence/reflectance probes cannot be used as the tissue Raman signals are weak and are therefore easily be masked by the probe Raman background and the elastically scattered light. In our Raman probes, a central excitation fiber that delivers the light to tissue is surrounded by a ring of collection fibers that connect to the spectrograph. The distal tip of the probe contain specialized filters on both excitation and collection fibers which serve to reject probe (fused silica) background and elastically scattered light, respectively, thus enabling efficient collection of the Raman signals. A sapphire ball lens is tightly secured at the probe tip, and positioned an appropriate distance from the fibers to insure a collimated beam of excitation light

and optimal collection of light emitted from the tissue. The probe is 4 m long and less than 3 mm in overall diameter. The light collected by the probe is passed through a spectrograph and dispersed onto a CCD. Integrated software in the system enables rapid collection of Raman spectra (1 s) and real-time analysis (1-2 s) of the spectral parameters. The clinical Raman system has been used for previous studies of atherosclerosis and breast cancer [89, 94].

Another approach utilized by a different group avoids the problem of fused silica background by collecting Raman signals in the high wave number region (2400-3800 cm^{-1}) rather than the fingerprint region (400-1800 cm^{-1}) [114]. This approach enables the usage of a single unfiltered fiber for both excitation and collection; however, it comes at the expense of losing some, potentially critical, spectral information that is only present in the fingerprint region.

■ 1.6 Clinical work

This section briefly describes the previous *in vivo* clinical work of the different spectral modalities with relation to atherosclerosis and vulnerable plaque. One of the goals of the present work is to demonstrate clinical *in vivo* application of MMS as a diagnostic tool for detection of vulnerable plaques.

■ 1.6.1 Reflectance and fluorescence of arterial tissue

To our knowledge, no [ultraviolet-visible] DRS measurements have been done *in vivo* on human arterial tissue. Some clinical work has been done using near-infrared spectroscopy, as described earlier, and spectra were collected from exposed carotid arteries at the time of surgery [59]. Among the studies of atherosclerosis and vulnerable plaque using fluorescence mentioned earlier, no *in vivo* work in humans has been reported, with the mentioned *in vivo* studies utilizing an animal model

such as rabbits [73, 78]. Nevertheless, these studies, in which fluorescence spectra were collected either from exposed arteries or via intravascular fluorescence catheters, demonstrated the promising potential that fluorescence measurements, both continuous-wave and time-resolved, could be done in humans as well.

■ 1.6.2 Raman spectroscopy of arterial tissue

Previous *in vivo* Raman studies have been limited to directly accessible organs and tissues such as the skin, oral palate, cervix and sheep aorta. Some of these studies used large and impractical clinical systems, and those that used small diameter probes required long collection times and exhibited poor signal-to-noise ratio (SNR) [115, 116, 117, 118, 119, 120]. Our laboratory recently conducted the first *in vivo* Raman studies of human artery. The studies were conducted in the Vascular Surgery Department of MetroWest Medical Center in Natick, MA during carotid and peripheral vascular surgery [89]. Using the clinical Raman system and probe, 20 *in vivo* cases were conducted, six carotid endarterectomies and 14 femoral artery bypass procedures. Raman spectra were taken from 74 sites, 34 of which were then biopsied, and the specimens fixed, processed and histologically examined. The Raman model used to fit the data included the previously described morphological structures and, as well, the additional relevant Raman components associated with the probe and the *in vivo* environment: epoxy, sapphire, water, and oxy-hemoglobin. The fit coefficients associated with each morphological Raman structure extracted from the data were used with the diagnostic algorithm previously established *in vitro* [85]. The histology generally agreed with the Raman fit coefficients, and the overall diagnostic agreement was 74%, the discrepancies and misdiagnoses attributed to registration errors between spectroscopy and pathology, and the limited number of samples in the study. In addition to the classification of non-atherosclerotic,

non-calcified plaque, and calcified plaque, the ability to detect thrombosed and ruptured plaques, both types of vulnerable plaque, was demonstrated. Using logistic regression, the most important morphological fit coefficients in discriminating vulnerable and non-vulnerable plaques were Hb, CM, CF, and the sum of CC and FC/NC. Logistic regression and leave-one-out cross validation resulted in an algorithm that could correctly identify 11 out of 14 vulnerable and 17 out of 20 stable plaques, implying a sensitivity of 79% and specificity of 85%. This was an important first indication that Raman spectroscopy could potentially identify vulnerable plaque [89].

■ 1.7 Thesis outline

This thesis aims to achieve the following goals:

- Demonstrate that reflectance, fluorescence, and Raman spectroscopy all provide valuable diagnostic information about plaque vulnerability and should thus be combined as MMS
- Develop analytical tools for quantitative analysis of data and assessment of diagnostic confidence that can be applied to a single spectrum
- Develop an integrated spectral probe that can be used to efficiently collect all MMS modalities and accurately model its excitation/collection geometry
- Develop an integrated MMS instrument that is portable, meets clinical constraints and capable of real-time data collection and disease diagnosis
- Demonstrate that MMS can be implemented in a clinical setting and can, with high accuracy, detect vulnerable atherosclerotic plaques

This remainder of this thesis is structured as follows. Chapter 2 provides the motivation for MMS through an *in vitro* pilot study of excised tissue. Spectra are collected with two clinical

instruments (Raman and FastEEM) and two optical fiber probes (Raman and DRS/IFS probes). The extracted spectral parameters show correlation to the histological parameters indicative of plaque vulnerability and thus forms the basis for the development of MMS. Chapter 3 then provides the quantitative tools for robust data interpretation and calculation of uncertainty in extracted spectral parameters. Specifically, a formula is presented, along with its mathematical derivation and spectroscopic interpretation, that allows the quantification of uncertainty in extracted spectral parameters from a single measurement. This ability is critical when designing an MMS instrument that has limited time to acquire all spectral modalities but needs to provide quantitative spectral parameters in real-time. The development of the specialized MMS probe used to acquire data from tissue is detailed in Chapter 4. This probe is builds on the design of the Raman probe, since that modality is rate-limiting, to enable efficient excitation and collection of DRS and IFS. To enable the accurate extraction of spectral parameters, the modeling of DRS and IFS spectra collected with this probe was modified through calibration. Chapter 5 describes the clinical MMS instrument, a highly modular and portable system for practical applications. The automated system contains all the necessary excitation sources, that are sequentially coupled to the MMS probe via an optical fiber switch, and two CCDs. Moving to a clinical application, Chapter 6 discusses clinical results with the developed instrumentation and probes. Spectra were collected from patients undergoing vascular surgeries at a collaborative hospital. Comparing the spectroscopy to histology, an algorithm for detecting vulnerable plaque is developed that achieves excellent diagnostic accuracy. Lastly, Chapter 7 comments on the accomplishments of each of the specified goals of this thesis. Finally, Chapter 8 concludes with an outlook to future directions in the field.

Chapter 2

Pilot MMS study

2.1 Introduction

This chapter explores the potential of MMS to evaluate the morphological features of atherosclerotic plaque and assess plaque vulnerability, particularly by the detection of intraplaque hemorrhage, density and depth of superficial foam cells, fibrous cap thickness, and necrotic core size. The results of the following feasibility study indicate that MMS has the potential to accurately assess plaque vulnerability *in vivo*, in real-time and as a guide to future treatment. Thus, this chapter provides the motivational rationale for pursuing MMS as a diagnostic technique. There are two experimental subsections: 1) depth sensing, and 2) *in vitro* tissue study. Two relevant addenda are also included: 1) detecting fibrous cap thickness with fluorescence, and 2) freeze/thaw effects on spectroscopy.

2.2 Methods

2.2.1 Depth sensing

Light of different wavelengths penetrates tissue to different depths. The effective penetration depth is defined as the depth at which the power of light incident on a tissue sample falls to 1/e of its

incident value, and can be calculated from diffusion theory:

$$\delta = \frac{1}{\mu_{eff}} = \frac{1}{\sqrt{3\mu_a(\mu_a + \mu_s^{'})}}, \tag{2.1}$$

using the values for the reduced scattering coefficient $\mu_s^{'}$ and absorption coefficient μ_a of tissue [68]. Based on this equation, the literature on the optical properties of aorta indicates effective penetration depths of about 90, 140 and 1200 μm for light of wavelengths 308, 340 and 830 nm, respectively [121]. Another study indicates values 70, 90, and 800 μm for the effective penetration depths of 308, 340, and 830 nm in aortic tissue [90].

We performed experiments to verify these values using our instruments and probes. The penetration depths at different excitation wavelengths were measured by incrementally stacking 20 μm thick sections of aortic media. An optical fiber probe, placed in contact with the tissue, delivered the light and a power meter measured the transmitted power as a function of tissue thickness. Note that in the single-ended geometry of our artery studies (i.e. the probe both delivers and collects light from the same side of the tissue), we need to account for the propagation of both the excitation and emission light. Thus the sampling depth, δ_s, can be related by

$$\frac{1}{\delta_s} = \frac{1}{\delta_{ex}} + \frac{1}{\delta_{em}}, \tag{2.2}$$

where δ_{ex} and δ_{em} are the penetration depths of the excitation and emission light, respectively. Other groups have defined the sampling depth, or probing depth, as a depth from which 90% of the remitted fluorescence originates [122].

■ 2.2.2 Tissue study

We have performed a preliminary *in vitro* study to establish the effectiveness of DRS, IFS, and Raman spectroscopy for providing information about plaque morphology and vulnerability. Spectra were collected from excised human carotid endarterectomy specimens (n = 17) from 12 patients, obtained from the Cooperative Human Tissue Network. The snap-frozen specimens were thawed and rinsed in phosphate-buffered saline. The DRS and IFS spectra were obtained using a fast excitation-emission matrix (FastEEM) instrument and probe, described in Sec. 5.1.2 and elsewhere [110, 111]. The FastEEM probe was placed in gentle contact with the intimal layer of the tissue while DRS and IFS spectra were collected (1 second total acquisition time). The Raman signal was then acquired from the same location using a clinical Raman system and probe, described in Secs. 5.1.1 and 4.1, and elsewhere [87, 88] (1-5 seconds total acquisition time). Care was taken to insure the placement of the probes on the same tissue location.

Following spectral acquisition, the evaluation site was demarcated with India ink and the specimen was fixed in formalin, routinely processed, sectioned and stained with hematoxylin and eosin. Histopathology for each of the 17 specimens was performed by an experienced cardiovascular pathologist (Maryann Fitzmaurice) blinded to the spectroscopy results. The morphological features associated with plaque vulnerability were assessed: fibrous cap thickness, necrotic core size, superficial foam cells, intraplaque hemorrhage, and ulceration. In this study, we analyzed each of these vulnerability features independently, without going further to classify an overall lesion as vulnerable using some combination of these features, as we do eventually with the vulnerable plaque index (Sec. 6.2.4). The intimal or fibrous cap thickness was recorded as the range of thicknesses found underneath the ink dot. The necrotic core size was recorded as the maximum dimension of the core beneath the fibrous cap, if present. The foam cells were evaluated based on the most superficial

depth at which they were found and a density grade (0 = none; 1+ = isolated single foam cells; 2+ = small clusters of foam cells; 3+ = confluent sheets of foam cells). Intraplaque hemorrhage was identified as an accumulation of blood within the lesion, usually associated with the core. Plaque ulceration was graded based on whether the defect in the fibrous cap did (rupture) or did not extend (fissure) into the underlying atheroma core.

DRS spectra were used to extract the wavelength-dependent absorption coefficient μ_a and reduced scattering coefficient $\mu_s^{'}$ based on a diffusion theory model [66]. A more detailed description of DRS modeling can be found in Sec. 4.3.1. We modeled $\mu_a(\lambda)$ as a linear combination of two absorbers, oxy-hemoglobin and β-carotene:

$$\mu_a(\lambda) = [HbO_2] \cdot \epsilon_{HbO_2}(\lambda) + [\beta - car] \cdot \epsilon_{\beta-car}(\lambda), \tag{2.3}$$

with [HbO_2] and [β-car] the concentrations and ϵ_{HbO_2} and $\epsilon_{\beta-car}$ the extinction coefficients of oxy-hemoglobin and β-carotene, respectively (Fig. 2-2a). Deoxy-hemoglobin was not included in the model because this is an *in vitro* study of frozen-thawed tissues in which the hemoglobin was oxygenated by exposure to room air. We modeled the $\mu_s^{'}(\lambda)$ spectrum as an inverse power law:

$$\mu_s^{'}(\lambda) = A \cdot \left(\frac{\lambda}{\lambda_0}\right)^{-B}, \tag{2.4}$$

as reported elsewhere [123, 124], where A specifies the amplitude of scattering, B the power law decay, and $\lambda_0 = 1$ μm is a normalization factor.

IFS spectra were obtained by correcting the raw fluorescence for the effects of scattering and absorption [79, 80]. A more detailed description of IFS modeling can be found in Sec. 4.3.2. Based on literature values, IFS spectra excited at 308 and 340 nm have the shallowest sampling depths

and were used to assess the composition of the fibrous cap. Multivariate curve resolution (MCR), a chemometric technique used to extract the individual spectra of a known number of components from a mixture spectrum [125], was performed on the IFS spectra at each of the two excitation wavelengths. For IFS at 308 and 340 nm, a linear combination of two MCR components (MCR_1 and MCR_2, Figs. 2-2b and 2-2c) resulted in good fits to all 17 spectra. The fit coefficient of the blue-shifted and narrower MCR component (MCR_1) is reported as C_{308} and C_{340} for IFS at 308 and 340 nm, respectively.

Raman spectra were extracted from the raw signals by removing the Raman probe background using a calibration spectrum collected from an aluminum block, and removing the tissue fluorescence using a 6^{th} order polynomial fit [87]. Then, the Raman spectra were fit using a linear combination of basis spectra components of the eight morphological structures (CF, CC, CM, EL, AA, FC/NC, β-CC, and SMC) and hemoglobin (Fig. 2-2d). The Raman fit coefficients were normalized to sum to unity so that each fit coefficient specifies a percentage contribution to the fit by that respective basis spectrum, as previously described [86, 89, 126]. The hemoglobin contribution to the Raman spectra was zero in all of our samples as hemoglobin is a relatively weak Raman scatterer at 830 nm excitation. The spectral parameters obtained were then correlated with the presence (or absence) of the morphologic features of vulnerable plaque.

■ 2.3 Results

■ 2.3.1 Depth sensing

In our experiments, the effective penetration depths at 308 and 340 nm were measured as 85 and 105 μm, respectively. The corresponding fluorescence emission peaks were 400 and 410 nm, respectively, with effective penetration depths of 128 and 147 μm. Therefore, the sampling depths

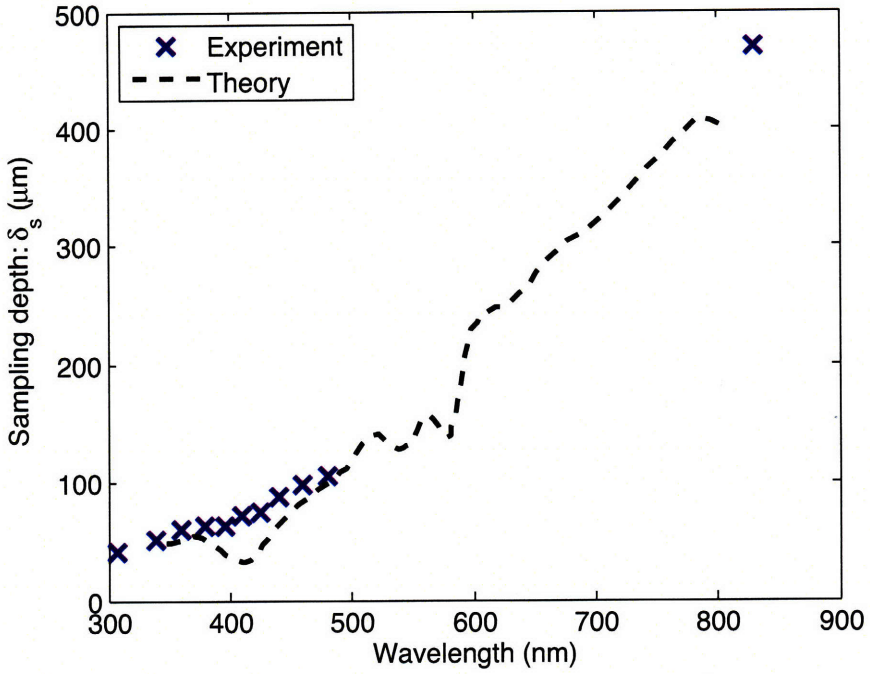

Figure 2-1. The sampling depth of light in aortic media as function of wavelength. The experimental values were obtained via transmission measurements of light through stacked slices of aortic media. The theoretical values were obtained using the values for μ_a and μ_s' from Fig. 1-2 and Eqs. (2.1) and (2.2).

for the IFS at 308 and 340 nm are 51 and 62 μm, respectively, accounting for the longer emission wavelength of the fluorescent light (Eq. 2.2). Similarly, different wavelength regions of the DRS spectra sample tissue at different depths (50 - 400 μm). A previous experiment estimated the sampling depth of 470 μm for 830 nm Raman excitation [127]. These results are summarized in Fig. 2-1. The above penetration depths, measured on aortic media, may vary with different types of lesions. Nevertheless, the trend of deeper sampling depth for longer wavelength excitation light still holds for each sample or atherosclerotic lesion.

Specimen number - -	SNOMed Classification - -	Intimal or fibrous cap thickness (microns)	Necrotic core thickness (microns)	Foam cell depth (microns)	Foam cell grade (0-3+) -	Intraplaque hemorrhage - -	Ulceration - -
1	IF	24-64	-	-	-	-	-
2	IF	40-80	-	-	-	-	-
3	ATS	480-500	-	480	3+	-	-
4	ATS	240-440	-	40	1+	-	-
5	ATS	456-536	-	456	2+	-	-
6	ATM	200-320	400	280	2+	-	-
7	ATM	460-640	560	-	-	-	-
8	ATM	440-500	4800	440	2+	-	-
9	ATM	1000-1500	6400	1800	1+	-	-
10	ATM	520-640	1340	640	2+	-	-
11	CATM	140-160	1840	68	1+	-	-
12	CATM	120-480	4000	120	1+	-	-
13	CATM	1440-1600	240	256	1+	-	-
14	CFS	0-400	-	-	-	Acute	Fissure
15	FS	40-80	-	-	-	-	Rupture
16	ATS	27-52	-	0	1+	-	-
17	ATM	0-280	1600	28	2+	-	Rupture

Table 2.1. Morphological features of the 17 specimens. IF = intimal fibroplasia, ATS = atherosclerotic plaque, ATM = atheromatous plaque, FS = fibrotic-sclerotic plaque, C = calcified.

■ 2.3.2 Tissue study

The histopathologic parameters relating to plaque vulnerability are summarized in Table 2.1 for each of the 17 specimens. The last four specimens exhibit the hallmarks of vulnerable plaque and are so classified: specimen #14 contains an intraplaque hemorrhage, specimens #14-17 all have thin (< 65 μm) fibrous caps, some of which also exhibit the presence of ulceration, superficial foam cells, and necrotic core. The remaining specimens (#1-13) do not have the necessary combination of features to be deemed vulnerable.

Figure 2-2 shows the model components: oxy-hemoglobin and β-carotene extinction spectra (DRS), MCR components for IFS at 308 and 340 nm, and Raman morphological basis spectra. Representative MMS spectra from the three modalities are shown in Fig. 2-3 for (a) intimal fibro-

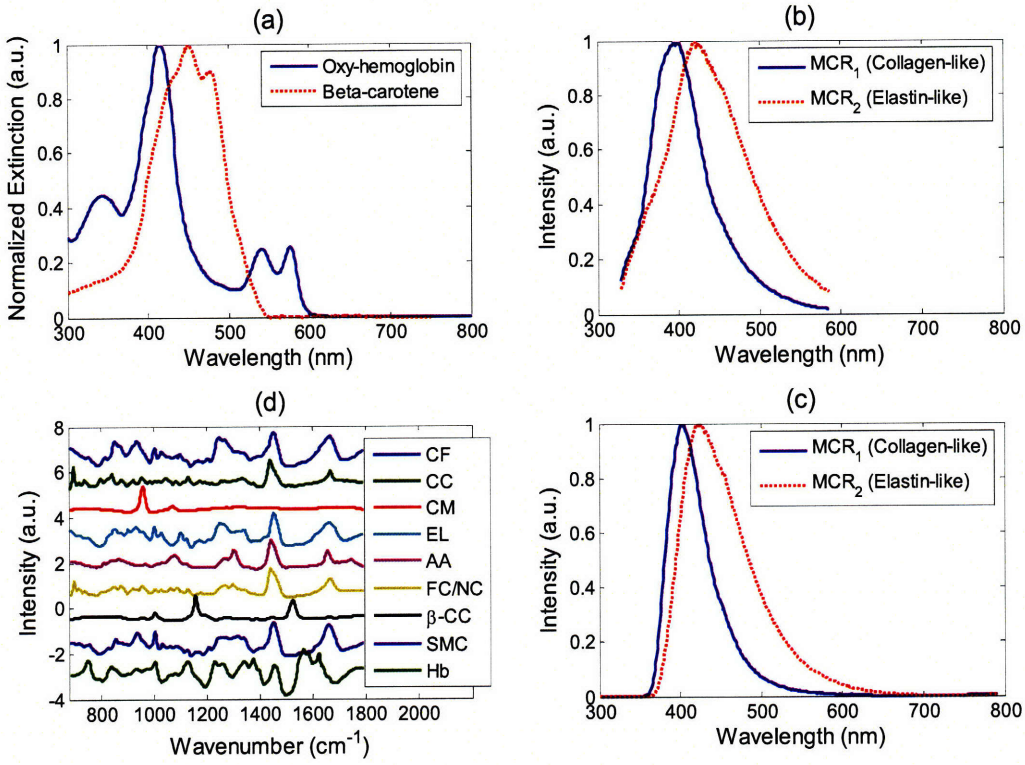

Figure 2-2. a) Extinction coefficients of oxy-hemoglobin and beta-carotene; b) MCR basis spectra components for IFS at 308 nm; c) MCR basis spectra components for IFS at 340 nm; d) Raman morphological model basis spectra.

plasia, (b) non-vulnerable atherosclerotic plaque, and (c) vulnerable atheromatous plaque. The difference between the measured spectrum and the model fit, the residual, is shown below each spectrum. Lack of significant structure in the residuals demonstrates that the model accounts for the majority of spectroscopic features observed and robustly describes the data.

The following spectroscopic parameters showed the best correlation with morphologic features of vulnerable plaque: DRS hemoglobin concentration [HbO_2], DRS scattering parameter A, IFS parameter $\rho = C_{308}/C_{340}$ and Raman parameter Σ = CC + FC/NC.

The DRS spectra are composed of contributions from absorption and scattering. The absorption is primarily due to oxy-hemoglobin, with a smaller contribution due to β-carotene. The scattering

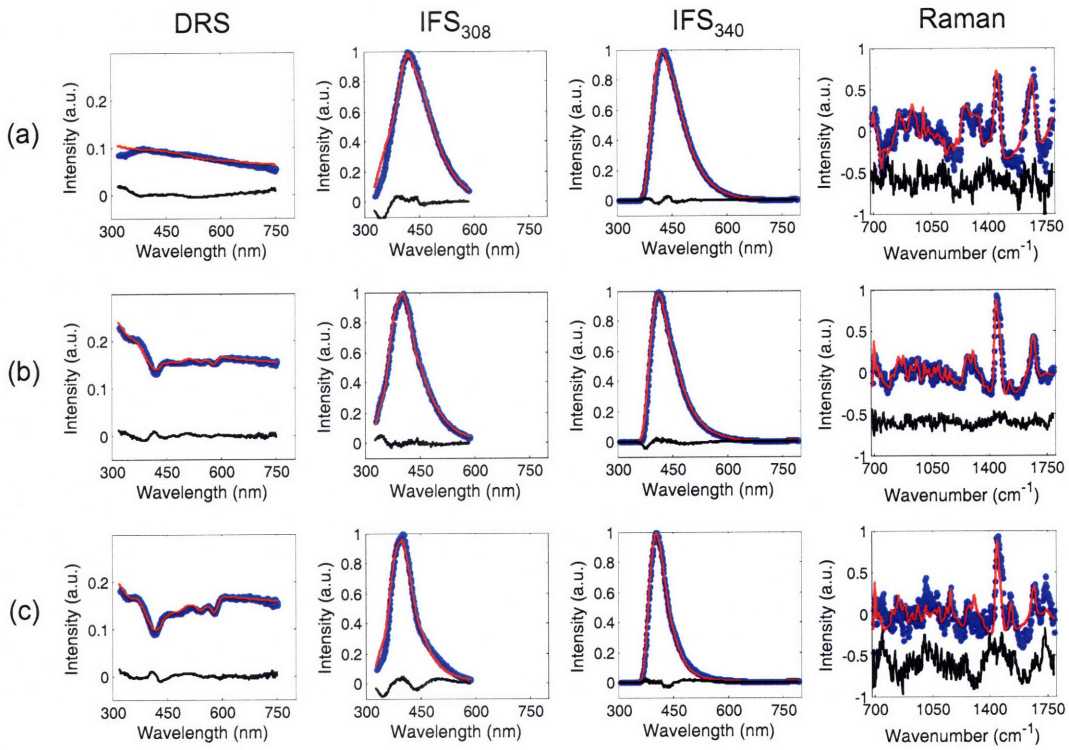

Figure 2-3. Representative spectra (dotted blue line), fits (solid red line), and residuals between the data and fit (solid black line) of the MMS modalities for three specimens with different pathologies: a) intimal fibroplasia; b) atherosclerotic plaque (not vulnerable); and, c) vulnerable atheromatous plaque. Note the progression of an increased presence of hemoglobin (420 nm absorption dip in DRS) for the three specimens. The IFS spectra for intimal fibroplasia are broader (characteristic of elastin) when compared to the more narrow spectra for the plaques (characteristic of collagen in the fibrous cap). The Raman spectrum of c) is noisy, due to the decreased signal intensity associated with hemoglobin absorption.

parameter A is related to the total amount of scattering produced by the tissue. The parameters [HbO_2] and A are given in Figs. 2-4a and 2-4b, respectively, for the 17 specimens.

Components MCR_1 and MCR_2 of IFS at both 308 and 340 nm (Fig. 2-2) exhibit features similar to the IFS spectra of collagen and elastin, respectively, as reported in previous studies at similar excitation wavelengths [70, 128, 129]. According to these previous studies, the fluorescence emission of elastin and the fluorescence emission of lipids (or necrotic core) are very similar at these excitations. Both IFS MCR_1 and the fluorescence spectrum of collagen are blue shifted and more

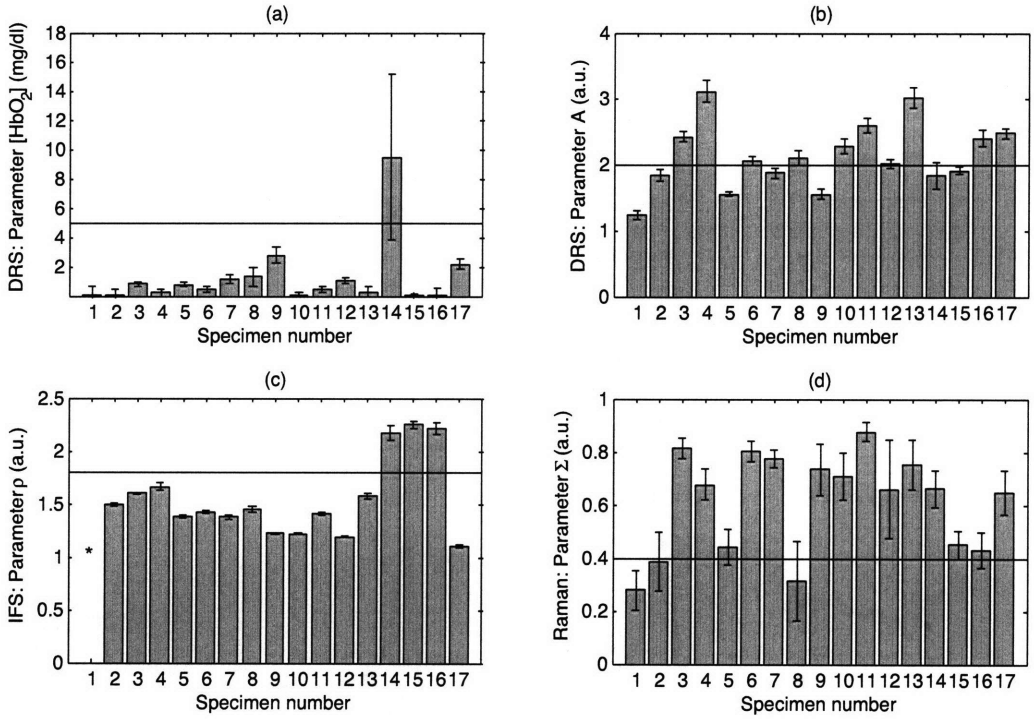

Figure 2-4. Spectral parameters for each of the 17 specimens: a) hemoglobin concentration (mg/mL) obtained from DRS, used to detect intraplaque hemorrhage; b) scattering parameter A (relative units) obtained from DRS, used to detect the presence of foam cells; c) ρ parameter (relative units) extracted from IFS_{340} and IFS_{308}, used to detect a thin fibrous cap (The value of ρ for specimen #1 (*) is undefined as C_{340} is within the error for this sample); and d) the Σ parameter (relative units) extracted from the Raman fit coefficients, used to obtain information about the presence of necrotic core. The error bars indicate one standard deviation.

narrow when compared to IFS MCR_2 and the fluorescence spectrum of elastin, which has a longer tail. Thus, we conclude that the corresponding fit coefficients C_{308} and C_{340} of MCR_1 are related to the amount of collagen present within the tissue volume sampled. We define an IFS parameter ρ as the ratio of the fit coefficients of MCR_1 at 308 and 340 nm excitation ($\rho = C_{308}/C_{340}$), which is related to the amount of collagen present and the depth at which it is found. Since the sampling depth at 340 nm excitation is greater than that at 308 nm (see Sec. 2.3.1), C_{340} provides information about collagen distributed over a greater depth compared to that provided by C_{308}. Values of ρ are shown in Fig. 2-4c for each of the specimens. (For additional results relating to collagen depth

sensing with IFS, see Sec. 2.6.) A value of ρ was undefined for specimen #1 as C_{340} was smaller than the error in this case (see Sec. 2.3.3), implying a potential division by zero.

Previous diagnostic algorithms [86] were able to discriminate plaque content using the sum of the Raman fit coefficients for CC and FC/NC. Similarly, we defined a parameter Σ = CC + FC/NC, which is given for each specimen in Fig. 2-4d. We will use Σ to measure the presence of necrotic core.

■ 2.3.3 Error analysis

In order to determine the error (uncertainty) in our spectral parameters, we performed a chi-square analysis and applied the error propagation formula [103]. Chi-squared (χ^2) analysis is a standard method for calculating the goodness of a fit and the uncertainty associated with fitting parameters. Uncertainties reported for ρ and Σ are based upon propagating the uncertainty from the individual components. The error bars in Fig. 2-4 that indicate the uncertainty of each extracted parameter are generated from this analysis. We could have equivalently performed the uncertainty analysis of Raman and IFS spectra using the Δc analytical framework presented in Sec. 3.1 while χ^2 would still need to be used for the nonlinear DRS fitting as described in Sec. 3.2.

■ 2.4 Discussion

We compare the extracted spectroscopic parameters with the measured morphologic features, and demonstrate how the former can be used to make inferences about the latter, and thus serve to characterize plaque vulnerability. The small size of this sample set is somewhat compensated for by our ability to directly compare spectroscopic features with those of pathology.

■ 2.4.1 Intraplaque hemorrhage

. Intraplaque hemorrhage is an unambiguous marker of plaque vulnerability. Histopathology indicates that specimen #14 is a site of acute intraplaque hemorrhage (Table 2.1, Fig. 2-5a); the other specimens are not hemorrhagic. MMS indicates that specimen #14 also exhibits a high value of [HbO_2] (9.5 mg/mL) as assessed by DRS (Fig. 2-4a), whereas all other non-hemorrhagic specimens have relatively low [HbO_2] values ($<$ 3 mg/mL). This indicates that a high concentration of hemoglobin inside the plaque, as measured by DRS, is consistent with intraplaque hemorrhage. The intraplaque hemorrhage in sample #14 was not detected by Raman spectroscopy (though the hemoglobin basis spectrum) because of the presence of calcification in the tissue. The contribution of CM dominates the Raman spectrum of specimen #14 and marginalizes the contribution from all other components.

■ 2.4.2 Foam cells

The presence of superficial foam cells is associated with plaque ulceration/erosion, and their detection is important in assessing plaque vulnerability [130]. We compared the magnitude of the scattering parameter A for specimens rich in foam cells and those without foam cells. It appeared that a threshold value of A could serve as a parameter for assessing the presence of foam cells. To enable an accurate comparison in establishing this threshold, we only considered specimens with a relatively thick fibrous cap. Two representative specimens with superficial foam cells (#11 and #12) had a mean value of A of 2.3 whereas two specimens without superficial foam cells (#7 and #9) had 1.7 as the mean value of A. Based on this, a threshold value of A = 2 was selected.

Foam cells are present in all 10 specimens with A $>$ 2 (Fig. 2-4b), and they occur at an average depth of 250 μm below the surface of these plaques (Table 2.1; Fig. 2-5b). Foam cells are observed

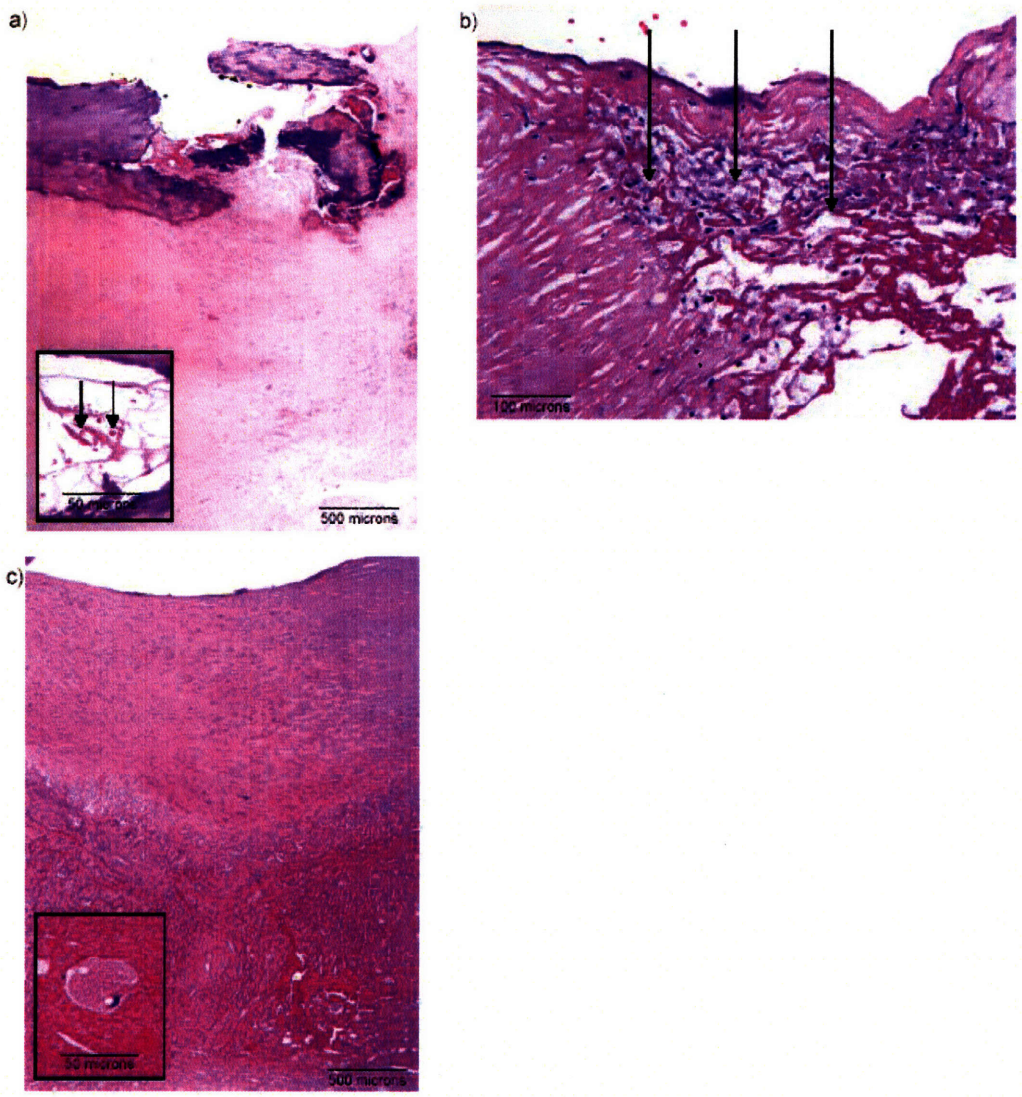

Figure 2-5. Photomicrographs of representative tissue sites: a) specimen #14, an ulcerated vulnerable plaque with acute intraplaque hemorrhage (insert; arrows indicate red blood cells) and hemoglobin fit contribution of 9.5 (mg/mL) (H&E; 4X); b) specimen #17 a vulnerable plaque with superficial foam cells (arrows) and scattering parameter A > 2 (H&E; 20X); and c) specimen #9, a non-vulnerable plaque with deep foam cells (insert) and scattering parameter A < 2 (H&E; 4X).

in only 2 of the 7 specimens with A < 2, and these foam cells tend to reside deeper in the plaque, at an average depth of 1100 μm (Table 2.1, Fig. 2-5c). Given the range of several hundred μm sampling depth for DRS excitation wavelengths, we do not expect to sense such deep lying foam cells; moreover, these deep-lying foam cells are not clinically relevant to plaque vulnerability. The inverse relationship of A with foam cell depth suggests that foam cells, which contain a high concentration of lipid vacuoles, are strong light scatterers and that their presence near the surface should markedly enhance tissue scattering. Thus, the intensity of scattering, as measured by DRS, can be used to indicate the presence of superficial foam cells.

■ 2.4.3 Thin fibrous cap

A thin fibrous cap is the hallmark of a vulnerable plaque. As discussed earlier, the parameter $\rho = C_{308}/C_{340}$ assesses the amount of collagen present in the top layer of tissue. A large value of ρ indicates a thinner layer. Hence, ρ can provide information about the thickness of the fibrous cap. To study this, we performed a two-layer Monte Carlo numerical simulation in which we varied the thickness of a top collagen-rich layer, modeling the collagen that comprises the fibrous cap, where the bottom layer (elastin or plaque core) is presumed to be semi-infinite. We assumed collimated delivery of excitation light in a uniform beam of 200 μm diameter; fluorescence was generated in the tissue proportional to the fluence of the excitation light within the varied top layer. The fluorescence collected at the surface, over an area of 400 μm diameter that is specified by the ring of collection fibers of the probe, was compared for 308 and 340 nm excitation wavelengths. As expected, the ratio of the collected fluorescence excited by 308 versus 340 nm light is a monotonically decreasing function of the thickness of the fluorescing layer, asymptotically leveling off, as shown in Fig. 2-6. For a 65 μm thick layer, the value of the ratio is approximately in the middle of the range. This

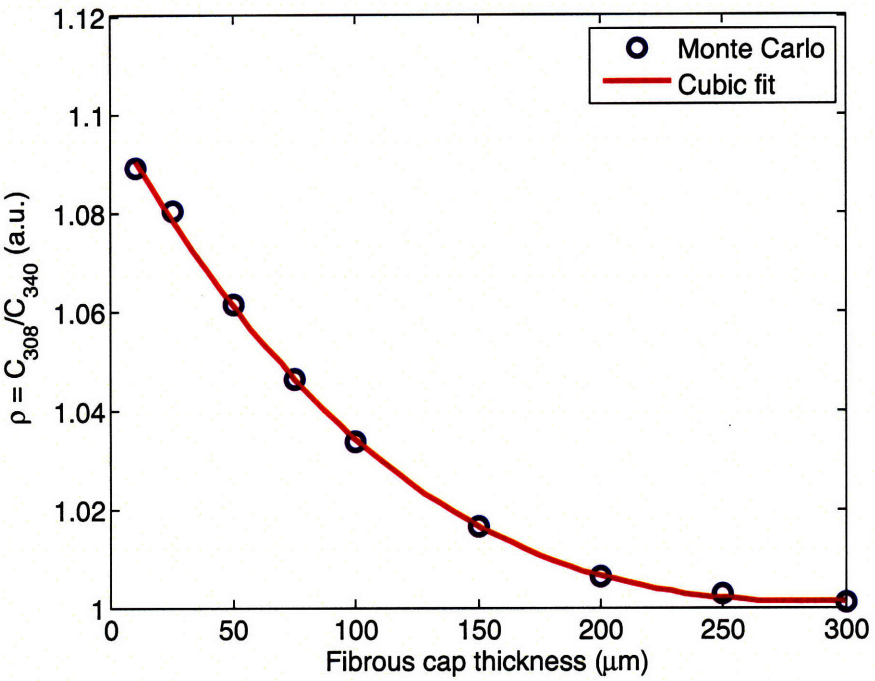

Figure 2-6. Simulated value of ρ as function of the thickness of the fibrous cap. The Monte Carlo simulation was run with two layers: top collagen-rich layer (variable thickness) and bottom collagen-free layer (semi-infinite). For each thickness of the top layer, a ratio of fluorescence (~420 nm emission) generated by 308 nm and 340 nm excitation was calculated.

suggests that the value of ρ in the middle of our experimental range of ρ's can separate specimens with thin fibrous caps from those with thicker caps. We thus chose $\rho = 1.8$ as the threshold value.

Indeed, of the diseased specimens (#3-17), all those with $\rho > 1.8$ (#14-16) have a minimum fibrous cap thickness well below 65 μm (Table 2.1), whereas the remaining diseased specimens have thicker fibrous caps. (It remains to be determined if and how the ρ parameter should be applied to intimal fibroplasia, as with specimens #1-2, given that the amount of intimal collagen may vary.) In specimen #17, the small value of ρ is not consistent with the histologically observed thin cap and associated plaque rupture. However, pathology also indicates that some portions of the fibrous cap are thick (range 0-280 μm), which can explain the small value of ρ. With this caveat, the

parameter ρ, an indicator of the amount of collagen present in the topmost tissue layer, can be used to estimate fibrous cap thickness.

■ 2.4.4 Necrotic core

When a large necrotic core is exposed to luminal blood flow following rupture of the fibrous cap, the coagulation cascade is triggered, resulting in thrombosis. We used the diagnostic parameter Σ, defined as the sum of the Raman fit coefficients for cholesterol crystals (CC) and foam cells/necrotic core (FC/NC), to assess presence of a necrotic core (Fig. 2-4d). Eleven of 14 specimens with $\Sigma > 0.4$ had either a necrotic core or were rich ($> 2+$) in foam cells; only 1 of 3 specimens with $\Sigma < 0.4$ had a necrotic core. Specimen #8 has a large necrotic core but $\Sigma < 0.4$; however, this plaque has a thick fibrous cap (> 440 μm), so the penetration depth of 830 nm light may not sufficiently sample the necrotic core in this case, and such a deep necrotic core is not associated with plaque vulnerability. In contrast, specimens #14 and #15 have high values of Σ but lack foam cells and necrotic core. It should be noted that these specimens are fibrotic-sclerotic plaques, demonstrating a well-developed fibrous cap but lacking a necrotic core and cholesterol crystals. Some investigators regard these as end stage plaques, in which the necrotic core may have been resorbed. Further studies will be needed to fully understand the significance of Σ, particularly in fibrotic-sclerotic plaques, but the results from this small sample set indicate the ability of Σ to detect necrotic core.

■ 2.4.5 Identifying vulnerable plaques

Fibrous cap thickness is a key parameter and, taken together with the presence of necrotic core or foam cells, can serve as an indicator of plaque vulnerability. In addition, the presence of intraplaque hemorrhage, by itself, indicates a vulnerable plaque. For our sample set, having $\rho > 1.8$ (thin fibrous cap) taken together with $A > 2$ (foam cells) and/or $\Sigma > 0.4$ (necrotic core), correctly identifies

three of the four vulnerable plaques (#14-16). A value of [HbO_2] > 5 (intraplaque hemorrhage) by itself, also correctly identifies sample #14 as vulnerable. As discussed earlier, sample #17, which exhibits rupture and is vulnerable, would be missed by this identification scheme. The ability to localize small regions of thinning of the fibrous cap is under investigation. All non-atherosclerotic samples (#1-2) and non-vulnerable plaques (#3-13) are correctly identified as such.

■ 2.5 Summary

This pilot study demonstrates the feasibility of using a combination of diffuse reflectance, intrinsic fluorescence, and Raman spectroscopy to detect morphological markers of vulnerable plaque. The approach is based on the correlation of parameters obtained from different spectroscopic modalities with pathology features and follows from a simple physical picture of the way light probes biological tissue. These spectroscopic parameters allow depth-sensing and provide information about intraplaque hemorrhage, superficial foam cells, a thin fibrous cap and large necrotic core, morphologic features that are associated with plaque vulnerability. In view of the small size of the sample set, these results should be considered preliminary. However, given these promising results, a larger study is warranted to establish the full potential of MMS by assessing spectral variability across many different pathologies and patients. The larger study will permit regression and statistics to be employed to validate these initial conclusions. Advances in instrumentation and the development of small-diameter side-viewing probes will enable percutaneous access to vessels and potentially provide clinically relevant information about plaque morphology. Thus, this method has the potential to guide diagnosis and treatment of atherosclerotic cardiovascular disease.

■ 2.6 Addendum 1: Detecting fibrous cap thickness revisited

After publishing the results from this pilot study [131], the idea of sensing fibrous cap thickness with IFS was revisited. Instead of using the previously described parameter $\rho = C_{308}/C_{340}$ that gives the ratio of collagen contributions to IFS excited at two different wavelengths, one can propose an alternate parameter:

$$R_C = \frac{C_{340}}{C_{340} + E_{340}}, \tag{2.5}$$

where C_{340} is the collagen-like contribution and E_{340} is the elastin-like contribution. (The assumption is, again, that what is referred to as elastin-like fluorescence could also have originated from lipids and/or necrotic core.) The parameter R_C still assumes the two layer model: a top collagen-rich layer overlying a bottom elastin or necrotic core layer. The advantage of the R_C parameter is that it is computed at only one wavelength, in this case for 340 nm excitation IFS, and that it essentially gives the relative amount of collagen observed in the IFS signal. In other words, $R_C = 0$ specifies a pure elastin-like contribution while $R_C = 1$ specifies a pure collagen-like contribution.

The diagnostic sensitivity of the proposed R_C parameter was evaluated in two ways. In the first, an analogous Monte Carlo simulation to the one presented in Fig. 2-6 was performed and the value of R_C was calculated for various thicknesses of the fibrous cap. Secondly, the R_C parameter was calculated for the 17 specimens. Both of these results are given in Fig. 2-7. For ease of comparison to the previous figure, the value of R_C^{-1} is plotted.

From the comparison between the Monte Carlo simulations, one can conclude that the R_C^{-1} parameter is much more sensitive that the ρ parameter, as evidenced by the larger contrast in the parameter value for thin fibrous caps. Moreover, the experimental diagnostic ability of the R_C^{-1} parameter is equivalent to, if not better than, that of the ρ parameter when applied to the 17

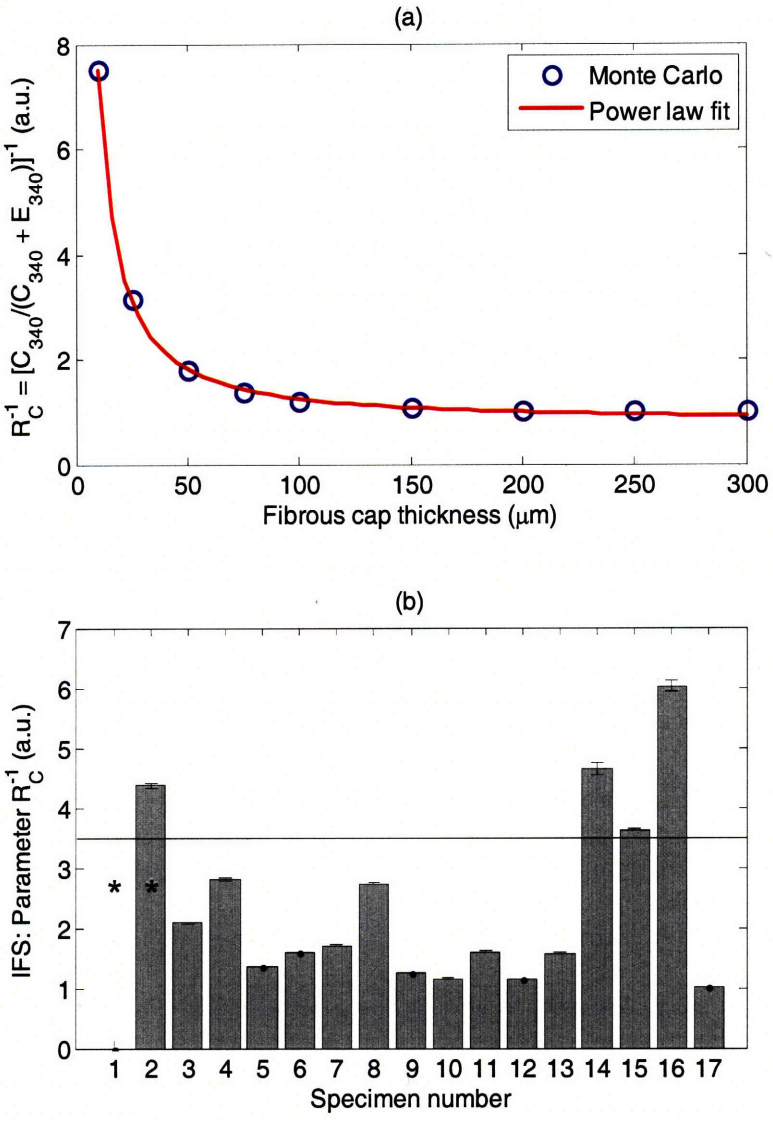

Figure 2-7. (a) Simulated value of R_C^{-1} as function of the thickness of the fibrous cap, which should be compared to the one for ρ presented in Fig. 2-6. (b) The value of R_C^{-1} computed for the 17 specimens, which should be compared to Fig. 2-4c. The error bars indicated one standard deviation. (The value of R_C^{-1} for specimens #1 and #2 (*) should be disregarded, as the two-layer model need not apply to intimal fibroplasia. Moreover, the value of R_C^{-1} for specimen #1 is undefined, for the same reasons as its ρ value.)

specimens. One can immediately observe the much higher difference in the value of R_C^{-1} for the thin fibrous caps and thick fibrous caps. The relatively high value of the R_C^{-1} parameter can still identify the three thin fibrous cap plaques, samples #14-16, while having the same limitation with specimen #17 as the ρ parameter. As stated earlier, the value of R_C^{-1} for specimens #1 and #2 (*) cannot be clearly interpreted, as the fibrous cap two-layer model need not apply to intimal fibroplasia.

In summary, Monte Carlo simulations show that the R_C^{-1} parameter exhibits more sensitivity to detecting thin fibrous caps and that proposed robustness is supported by the experimental data for the 17 specimens.

■ 2.7 Addendum 2: Freeze/thaw effects on tissue spectroscopy

Although the freeze/thaw process is known to introduce artifacts in fluorescence spectra of epithelial tissues [132, 133, 134], it is expected that these changes are less significant in artery wall than in epithelial tissues [70]. This is because our current artery models involve largely structural proteins, lipids and calcium salts that are unlikely to be affected by the freeze/thaw process. Evidence from the pilot clinical study in patients with peripheral artery disease supports this assumption, as the Raman spectra obtained *in vivo* were fit well by the spectral model developed using data obtained *in vitro* from frozen-thawed tissue, with the addition of basis spectra for probe components and oxy-hemoglobin [89]. Although it is possible that the IFS and DRS spectra may be more subject to freeze/thaw effects, this is not believed to be the case, as preliminary studies showed little difference in DRS and IFS spectra obtained from arterial tissue before and after freeze-thawing [64]. Figure 2-8 shows some representative *ex vivo* spectra from artery tissue that indicate that the freeze/thaw effect is minimal in DRS and IFS.

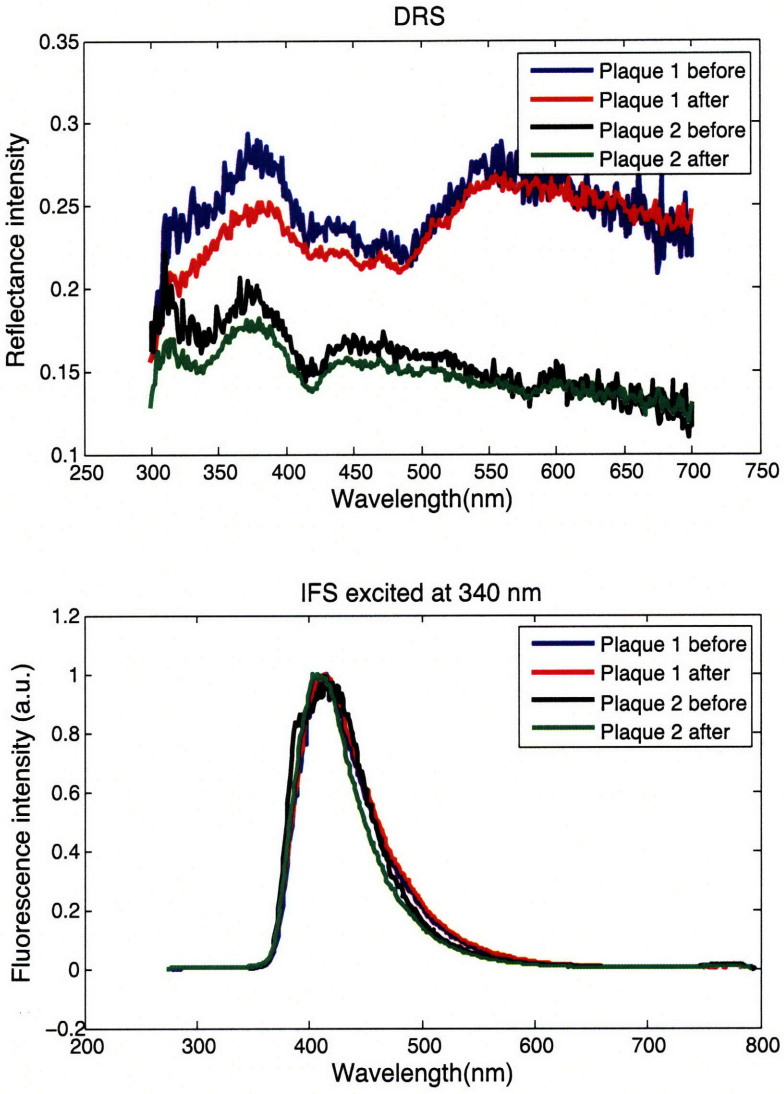

Figure 2-8. Freeze/thaw effects on DRS and IFS spectra of artery tissue. DRS (top) and IFS (bottom) spectra from two *ex vivo* artery tissue locations were collected, the tissue was then snap-frozen in liquid nitrogen and kept in the freezer for 60 days, after which the samples were thawed and spectra collected again.

Nevertheless, although our data to date indicate that freeze-thaw effects are not significant in arterial tissue for Raman, DRS or IFS, it may be necessary to obtain fluorescence basis spectra from fresh tissues, most likely "thin" sections obtained using a fresh tissue microtome, should problems with freeze/thaw effects arise.

■ 2.8 Acknowledgements

Dr. Maryann Fitzmaurice was responsible for all histological analysis of the arterial samples as well as for some of the physiological interpretation of the spectral parameters. Dr. George Angheloiu and Samir Awasthi helped collect the spectra from the excised tissue samples. Chae-Ryon Kong assisted with and provided results for the Monte Carlo simulations. Dr. Joseph Gardecki, Dr. Jason Motz, and Dr. John Kramer assisted with the interpretation of the results. Many of the images and text were reproduced from the *Journal of Biomedical Optics* [131] with permission from SPIE. This research was conducted at the MIT Laser Biomedical Research Center under NIH grant number R01-HL-64675 and grant number P41-RR-02594.

Chapter 3

Data and uncertainty analysis

This chapter describes ways to estimate uncertainty in parameters extracted from spectroscopic measurements. It is broken down in two sections, the first dealing with linear models (Raman and IFS) and the latter discussing the application of nonlinear models (DRS). For linear models, we build on previous work to develop an analytical expression for estimating uncertainty from a single measurement. On the other hand, for nonlinear models we utilize χ^2 analysis owing to an absence of valid analytical frameworks for characterizing uncertainty.

■ 3.1 Linear fitting - IFS and Raman

■ 3.1.1 Introduction

As overviewed in Sec. 1.4, uncertainty calculations can be performed by means of repeated measurements, χ^2 analysis, or through mathematical modeling of the system performance. In this section, we follow the third approach to uncertainty analysis and present a method of analysis that can be used in conjunction with a single spectrum to provide physical insight into the sources of uncertainty. The analytical expression employed for this purpose describes concentration uncertainty as a function of measurement noise, signal strength, and spectral overlap: quantities easily extracted from spectroscopic measurements. As such, the method can guide improvements in data modeling,

as well as optimization of the instrument. This approach can be considered as an extension and a complement to previous work of our research group [135]. In that study, we derived an analytical expression for the limiting uncertainty in analyte concentrations extracted from Raman spectra using partial least squares (PLS), and showed it to hold experimentally [135]. Uncertainty was expressed as a function of measurement noise and the b-vector using PLS. Since then, we have worked on characterizing the lower bound on the uncertainty in extracted concentrations using a more generally applicable approach [136]. Other groups have employed our framework in analyzing the uncertainties and sources of error in spectroscopic measurements [137].

Our approach is a special case of the error analysis of Lorber and Kowalski [104] where calibration is very accurate and thus model uncertainty is negligible. This is often the case, because variables such as integration time may be increased or optimized for the calibration data. Therefore, in the limit in which calibration noise is small, uncertainty will be dominated by measurement noise in the prediction sample.

Although we are focusing on the case when measurement noise dominates, the analytical expression presented here can be used, in many cases, even when model uncertainties are not negligible. Therefore, we may calculate both actual uncertainty, which takes into account modeling and measurement noise, as well as the limiting uncertainty, where model noise is disregarded. The limiting uncertainty, the unavoidable uncertainty associated with the inherent spectral noise in the prediction sample and the spectral makeup of the model, also specifies the smallest concentration at which a constituent can be detected. This approach is applicable to concentration measurements and for determining diagnostic accuracy of parameters obtained for spectral diagnosis of disease, using linear spectroscopic techniques such as Raman scattering or fluorescence, and is very important in system design and evaluation.

In the following, we derive an analytical expression for the limiting uncertainty, and show its equivalence to χ^2 analysis. We demonstrate that the concentration uncertainty calculated by the analytical formula is in good agreement with that measured experimentally from aqueous solutions of clinically-relevant analytes. Furthermore, we demonstrate that in this case the calculated actual uncertainties are very close to the limiting uncertainties, which is indicative of the accuracy of our data acquisition and modeling. To illustrate the biomedical application of this analytical formula, we calculate uncertainties of parameters extracted from tissue spectra that are used in disease diagnosis.

■ 3.1.2 Theory

We adopt a linear algebra approach and notation in this paper. All vectors are column vectors and are denoted by bold lowercase letters. Similarly, matrices are bold uppercase letters comprising multiple column vectors, where size is indicated in parentheses (row×column). Measurements and spectra are denoted as vectors, in that each element represents the response of a particular detector (e.g. CCD pixel). Many of the results presented below follow from Kay [138], a standard text in statistical signal processing.

Linear model.

We begin with the standard additive noise linear model:

$$\mathbf{s}=\mathbf{P}\mathbf{c}+\mathbf{w}. \tag{3.1}$$

The vector $\mathbf{s}$ is the observed measurement (M×1), the matrix $\mathbf{P}$ contains the model constituent vectors (M×N) and is full-rank, the vector $\mathbf{c}$ contains the underlying coefficients of the model

constituents (N×1), and the vector **w** represents noise in the system (M×1). Here M represents the number of wavelengths and N represents the number of model components. In other words, the measured vector **s** is a linear combination of the model components in **P**, weighted by the coefficients in **c**, and with the addition of random measurement noise **w**. The **w** is assumed to be a zero-mean Gaussian random vector with a known or measurable covariance matrix $\mathbf{C_w}$. Our goal is to analytically determine the best estimate $\hat{\mathbf{c}}$ (fit coefficients) of the true underlying coefficients **c** and the uncertainty specified by the standard deviation of that estimate. The application of the model, Eq. (3.1), to characterize spectroscopic measurements is appropriate. Raman and fluorescence spectra (**s**) have been shown experimentally to be linear combinations of the distinct individual spectra of the underlying chemical species that can be measured in isolation (**P**) and proportional to the concentration of those species (**c**) [139, 140]. Measurement noise (**w**) is typically associated with the measurement system and detector, and its statistics ($\mathbf{C_w}$) can be readily measured; moreover, the Gaussian assumption also holds well in practice. It should be noted that Eq. (3.1) is a special case of a more general formulation by Lorber and Kowalski [104] that can be specialized for our model as

$$\mathbf{s}=(\mathbf{P}+\delta\mathbf{P})\mathbf{c}+\mathbf{w}=\mathbf{P}\mathbf{c}+\mathbf{w}'. \tag{3.2}$$

The formulation of Eq. (3.2) also includes modeling uncertainty, $\delta\mathbf{P}$, taking into account the uncertainties of the concentrations and measurements of the constituent spectra. If the modeling uncertainty is also assumed to be Gaussian, its effect can be lumped together with the measurement noise as **w'**, where the covariance of **w'** is greater than that of **w** in Eq. (3.1). As noted earlier, in most of this paper we are interested in the limiting case in which the measurement noise of the prediction sample, **w**, is the dominant source of uncertainty. In this way we calculate the

limiting uncertainty.

Estimator performance.

In determining the optimal estimator, we restrict our attention to unbiased estimators: those that, on average, accurately return the underlying parameters $\mathbf{c}$. From the linear model with the assumptions described above and estimation theory, one can derive the minimum variance unbiased (MVU) estimator [138]:

$$\hat{\mathbf{c}} = (\mathbf{P}^{\mathbf{T}}\mathbf{C}_{\mathbf{w}}^{-1}\mathbf{P})^{-1}\mathbf{P}^{\mathbf{T}}\mathbf{C}_{\mathbf{w}}{}^{-1}\mathbf{s}. \tag{3.3}$$

This estimator is desirable because out of all possible unbiased estimators, it is the one that achieves the minimum variance for all combinations of unknown underlying parameters $\mathbf{c}$. For the MVU estimator of Eq. (3.3), it can be shown [138] that its covariance matrix is:

$$cov(\hat{\mathbf{c}}) = (\mathbf{P}^{\mathbf{T}}\mathbf{C}_{\mathbf{w}}^{-1}\mathbf{P})^{-1}. \tag{3.4}$$

The diagonal entries of this matrix specify the variances of each $\hat{c}_k$ fit coefficient. This is the most general result as it specifies the covariance and, in turn, the uncertainty, of our estimate for any particular noise covariance $\mathbf{C}_{\mathbf{w}}$ and the model matrix $\mathbf{P}$. The result of Eq. (3.4) can be specialized by assuming that $\mathbf{w}$ is white (i.e. uncorrelated and identically distributed) Gaussian noise so that $\mathbf{C}_{\mathbf{w}} = \sigma^2\mathbf{I}$. With this assumption, the MVU estimator and the covariance are given by [138]:

$$\hat{\mathbf{c}} = (\mathbf{P}^{\mathbf{T}}\mathbf{P})^{-1}\mathbf{P}^{\mathbf{T}}\mathbf{s}. \tag{3.5}$$

$$cov(\hat{\mathbf{c}}) = \sigma^2(\mathbf{P}^{\mathbf{T}}\mathbf{P})^{-1}. \tag{3.6}$$

The estimator, Eq. (3.5), can also be recognized as the OLS solution for $\mathbf{c}$, and each row of $(\mathbf{P^T P})^{-1}\mathbf{P^T}$ corresponds to the b-vector for that particular component.

One final remark involves the concept of the Cramér-Rao Lower Bound (CRLB) from estimation theory [138]. The CRLB is a lower bound on the covariance of any unbiased estimator. It can be shown that the covariance of this MVU estimator, Eq. (3.6), is equal to the CRLB and hence the estimator is deemed *efficient* [138]. Moreover, for the linear model given above, the efficient MVU estimator implies that it is also the maximum likelihood (ML) estimator. We shall revisit this last point later.

Simple formula: ΔC.

The estimation framework and the CRLB described above are well-known, general concepts applicable to any type of linear system with the above-mentioned assumptions. However, physical insight can be provided by specializing Eq. (3.6) in order to elucidate variables relevant to spectroscopy. We can express $\mathbf{P} = \mathbf{QS}$, with $\mathbf{S}$ being a diagonal matrix where the kth diagonal entry, s_k, is the Euclidean norm of the kth component in $\mathbf{P}$, as follows:

$$s_k = \sqrt{\sum_{i=1}^{M} (\mathbf{P}_{i,k})^2}. \tag{3.7}$$

and the columns of the matrix $\mathbf{Q}$ are thus normalized to unit length. This leads to a simple expression for the standard deviation, Δc, of the kth estimated parameter $\hat{c}_k$:

$$\Delta c \equiv std(\hat{c}_k) = \sigma\sqrt{(\mathbf{P^T P})^{-1}_{(k,k)}} = \frac{\sigma}{s_k}\sqrt{(\mathbf{Q^T Q})^{-1}_{(k,k)}} = \frac{\sigma}{s_k} \cdot olf_k \tag{3.8}$$

The first factor on the right hand side, σ, describes the measurement noise and s_k quantifies the signal strength of the kth model component at unit concentration. The spectral overlap factor, olf_k, indicates the amount of non-orthogonality (overlap) between the kth model component and the other (N-1) model components. The overlap factor may take on values between 1 and ∞. If all of the columns of P (or, equivalently, Q) are orthogonal (no overlap), then $olf_k = 1$. In the other extreme, if the kth column of $\mathbf{P}$ (or $\mathbf{Q}$) is nearly linearly dependent with one or more columns (almost complete overlap), then $\mathbf{Q}^T\mathbf{Q}$ is close to singular and its inverse does not exist. In a generalized sense, olf_k then approaches ∞. (In the case of two columns being linearly dependent, one of the two columns should be removed so that $\mathbf{P}$ becomes full rank, as was specified earlier). In other words, when the model $\mathbf{P}$ contains orthogonal constituent spectra, the estimator uncertainty, Δc, is equal to the ratio (σ/s_k) of the measurement noise to the signal strength for that particular component. In the extreme case of complete spectral overlap (two chemicals with very similar Raman or fluorescence bands across the wavelength range of interest), the estimate is unreliable so Δc approaches ∞. For the more commonly encountered case of partial spectral overlap of the linearly independent spectral components of $\mathbf{P}$, we have $1 < olf_k < \infty$ and Δc is a function of the three physically understandable quantities: σ, s_k, and olf_k. The concept of overlap factors as defined here is directly related to variance inflation factors (VIF), first proposed by Marquardt [141]. The relation of VIFs to the concept of condition number as well as other relevant methods for evaluation of spectral overlap are described by Kalivas [142]. The spectral overlap is also related to the NAS of a particular analyte in that the former measures overlap (interference) while the latter is an indication of non-overlap (orthogonality).

Limiting vs. actual uncertainty.

We note that, of the three parameters, σ varies from sample to sample because shot noise is dependent on the sample-specific raw signal, whereas s_k and olf_k are sample-independent for a given spectroscopic technique and model. The value of σ can be obtained in two different ways. One approach is to calculate σ from each pixel across many repeated measurements. The alternative approach, which requires only a single measurement, is to calculate σ from the residual between the observed spectrum and the best fit using Eq. (3.5). The former value of σ specifies the limiting uncertainty while the latter value specifies the actual uncertainty through Eq. (3.8). Therefore, we have

$$\sigma_{lim} = \sqrt{\frac{1}{M}\sum_{i=1}^{M}\left\{\frac{1}{L-1}\sum_{j=1}^{L}(s_{i,j}-\bar{s}_i)^2\right\}} \tag{3.9}$$

$$\sigma_{act} = \sqrt{\frac{1}{M}(\mathbf{s}\text{-}\mathbf{P}\hat{\mathbf{c}})^T(\mathbf{s}\text{-}\mathbf{P}\hat{\mathbf{c}})}, \tag{3.10}$$

where σ_{lim} is calculated as the root mean squared value (across M pixels) of the standard deviation of a representative pixel σ_i calculated from L repeated measurements, while σ_{act} is calculated from the residual as the root mean squared between the data $\mathbf{s}$ and the fit $\mathbf{P}\hat{\mathbf{c}}$. Under the assumption of Eq. (3.1) that the only source of uncertainty is measurement noise, both approaches should yield the same value for σ. However, if there are also modeling uncertainties as in Eq. (3.2), then only the second approach yields the actual σ, as the residual includes measurement and modeling noise. Therefore, $\sigma_{act} \geq \sigma_{lim}$, and the difference between the actual and limiting σ can serve to evaluate the accuracy of the modeling. In most of the following we use Eq. (3.10) to calculate σ. By extension, we can define Δc_{act} and Δc_{lim} using the values of σ_{act} and σ_{lim}, respectively.

Relation to chi-squared (χ^2).

A statistical method of calculating the uncertainty in extracted parameters can be implemented through χ^2 analysis. This quantity is defined as

$$\chi^2 = \sum_{i=1}^{N} \left(\frac{data_i - fit_i}{\sigma_i} \right)^2 . \tag{3.11}$$

Maximizing the likelihood of observing a particular measured spectrum (in random Gaussian noise) is equivalent to minimizing χ^2. The value of a parameter that minimizes χ^2 is the optimal ML value. The χ^2 function (of the underlying parameter) is parabolic in the vicinity of the minimum, and the curvature of the parabola is proportional to the uncertainty (standard deviation) in that parameter [103]. Specifically, the variance of the parameter is equal to the reciprocal of the curvature of the χ^2 function [103]. Equivalently, an increase of one standard deviation of the parameter from the value at the minimum increases χ^2 by unity [103, 143]. The χ^2 approach can be used in conjunction with many fitting procedures, regardless of whether the underlying fitting model is known (or directly measurable) or determinable through calibration. The analytical expression for Δc, Eq. (3.8), is equivalent to the one obtained statistically through χ^2 analysis. This is to be expected, since the MVU estimator (or the least squares estimator) is equivalent to the ML estimator. Hence the criterion, used in determining the ML estimate, should yield the same value for the parameter uncertainty as the analytical formula obtained for the MVU estimator. This is demonstrated in Secs. 3.2 and 3.3 in more detail.

3.1.3 Methods

In this section we demonstrate the application of the above error analysis formalism to the estimation of experimental uncertainty in a set of spectral measurements. Two experiments are performed, both using near infrared Raman spectroscopy. In the first experiment, we prepare aqueous mixtures of known concentrations of clinically-relevant analytes by dilution from stock solutions. Our goal is to extract the concentration measurements from the spectral data using OLS fitting of component spectra. The reference analyte concentrations are accurately known and the spectral noise of the component spectra is minimal. Therefore, we can demonstrate both accurate extractions of concentrations in the prediction set and accurate assessment of their uncertainties via our formalism. In the second experiment, we record spectra of human artery tissue from which we obtain diagnostic parameters. Although the spectral components of the artery tissue spectra are known with minimal uncertainty, accurate reference concentrations are unavailable. Therefore, we again utilize OLS, but we obtain the relative (normalized) fit coefficients for each model parameter. From this, we demonstrate uncertainty assessment of measurements from biological tissue and the resulting confidence in a particular diagnosis.

Concentration measurements.

Raman spectra were acquired from 60 aqueous solutions of glucose, creatinine, and urea with randomized analyte concentrations ranging from 0 to 50 mM. The solutions were contained in a 1 cm fused silica cuvette that had been photobleached for one hour to deplete fluorescent impurities prior to the start of the experiment. The Raman system consisted of an 830 nm diode laser that was directed through a holographic bandpass filter (Kaiser Optical Systems, Inc.) and aperture to reduce emission outside the center wavelength. An external photodiode monitored the intensity of

the laser beam and was used to correct for intensity variations. The laser beam was then passed through beam shaping optics and focused into the cuvette through a small hole in a gold-coated paraboloidal mirror (Perkin Elmer). The power at the sample was 217 mW with a spot area of $\sim$ 1 mm^2. Backscattered Raman light was collected by the paraboloidal mirror and passed through a 2.5 inch notch filter (Kaiser) to reject the Rayleigh peak at 830 nm. The filtered light was focused into an optical fiber bundle composed of 65 fibers, core diameter 396 μm, NA = 0.37 (Romack Fiber Optics). The input end was in the form of a circle and the output end was a single row of 65 fibers, serving as the entrance slit of an f/1.4 spectrometer (Kaiser). The light was dispersed with a holographic grating onto a liquid nitrogen-cooled CCD detector (1300×1340b, Roper Scientific). The integration time per spectrum, 2s, constituted one "frame," and 30 consecutive frames were collected. Spectra from 280-1700 cm^{-1}, occupying 1000 CCD pixels, were used in all data analysis. Owing to the large CCD size and the high-NA imaging system, the entrance slit image appeared curved on the CCD. Direct binning of vertical pixels would result in highly degraded spectral resolution [144]. To correct the image curvature, a processing routine was developed that utilizes multiple spectral lines of a strong Raman-active material such as acetaminophen for curvature calibration. The algorithm preserves instrumental diffraction-limited spectral resolution and improves wavelength accuracy of the measured spectra. The constituent spectra of the three chemically active species (glucose, creatinine, and urea) acquired at 53 mM concentration, as well as those of water and cuvette, are shown in Fig. 3-1. By applying the OLS fitting specified by Eq. (3.5), the experimentally measured, offset-corrected total spectrum from each frame can be decomposed into the concentrations of the underlying constituents. (Alternatively, if the spectral noise is not white, Eq. (3.3) can be used in place of Eq. (3.5).) All of the spectral fitting was performed in the wavelength (CCD pixel) domain.

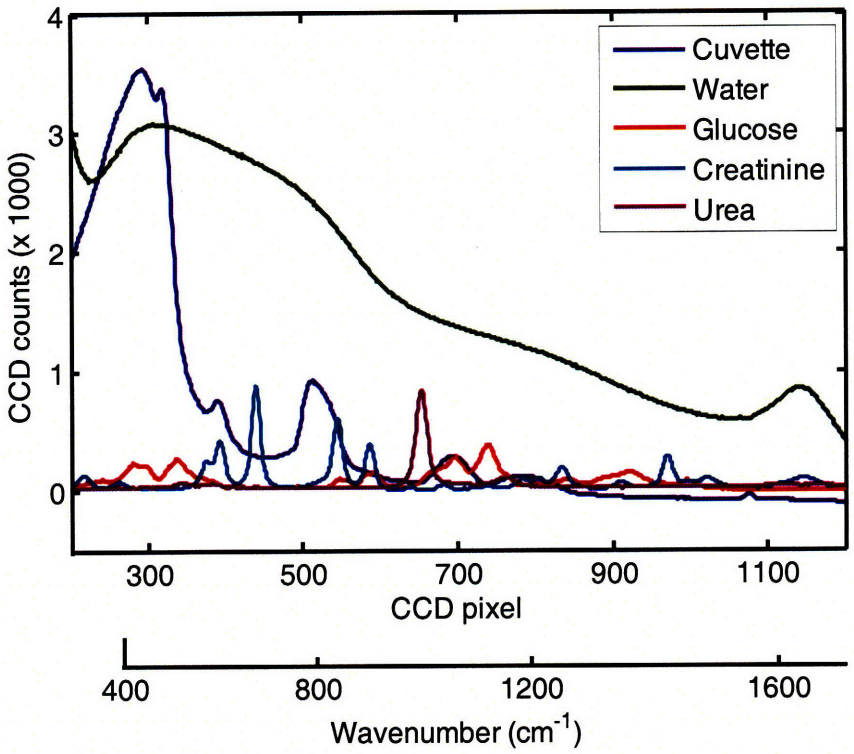

Figure 3-1. Constituent Raman spectra - glucose, creatinine, urea, water and cuvette - plotted as functions of wavelength (CCD pixel). The corresponding wavenumber scale is indicated below.

Some of the raw experimental spectra contained a distortion in the middle of the spectral range. This artifact, which varied in size from frame to frame, is attributed to variations in the opening and closing of the mechanical shutter that gates the CCD camera, which allows relatively more (or less) light to be collected in the middle of the spectral range. Although the amplitude of this artifact was not very large in absolute terms (50-100 counts out of $\sim$ 7000), the changes in the predicted concentrations from these faulty frames were significant, creating statistical outliers from the mean of the 30 repeated measurements. The faulty frames were easily identified by looking at the shape of the residuals between the data and the fit and were thus excluded from the ensuing analysis by setting a threshold on the amplitude of the residual. This resulted in the removal of 440 frames out

of the original 1800, so that each sample contained a set of approximately 25 measurements with minimal experimental artifacts.

Measurement of diagnostic parameters.

We have applied the Δc analysis to experimental Raman spectra obtained from human artery tissue to illustrate the application of this analysis method to disease diagnosis. The experiment with excised human carotid artery tissue was part of a separate study and is described in detail elsewhere [131]. The spectra were acquired using a clinical Raman system [88] and Raman spectral probe [87]. The excitation wavelength was 830 nm, laser power was 100 mW, spot area $\sim$ 1 mm^2, and the collection time was 5 seconds, typically acquired in 20 consecutive measurements of 0.25 seconds each. The details of the system are described in Ref. [88]. Raman spectra were extracted from the raw spectra by performing a white light correction, removing probe-related background, and subtracting tissue fluorescence [88, 87]. A model composed of Raman-active tissue constituents, obtained from confocal Raman microscopy spectra of eight artery morphological structures [85], was used to fit the data using OLS. Prior to fitting, the Raman tissue spectra were interpolated and binned onto the same wavenumber scale as the spectral model constituent spectra. Only relative intensities of the Raman spectral components were obtained, and those relative fit coefficients from the eight spectral components were normalized to sum to unity, as done previously [89].

■ 3.1.4 Results

Concentration measurements.

Figure 3-2 shows the data, the least squares fit using the spectral components, and the difference between the data and the fit (the residual) for one representative mixture. We can analyze how

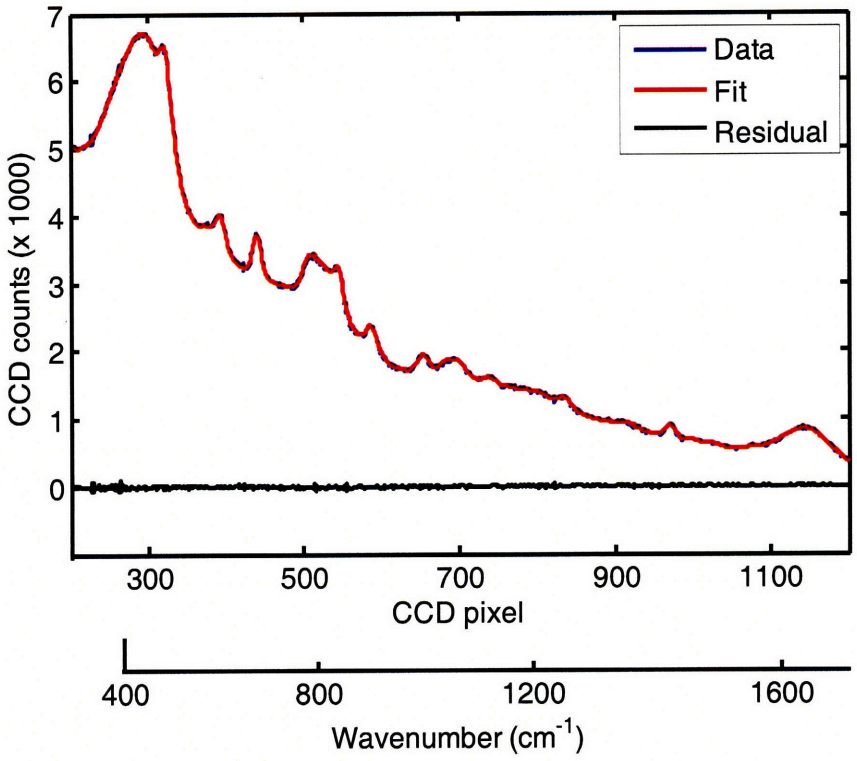

Figure 3-2. Representative data spectrum (blue), the least squares fit (red) and the residual between the data and the fit (black) obtained from a mixture solution. Spectral fitting is performed in the wavelength (CCD pixel) domain; the corresponding wavenumber scale is indicated below.

close the predicted parameters $\hat{\mathbf{c}}$ are to the reference values $\mathbf{c}$ by means of the plot of Fig. 3-3. The root mean squared errors of prediction (RMSEP) across the 1360 total repeated measurements for glucose, creatinine, and urea are 0.488 mM, 0.270 mM, and 0.321 mM, respectively.

We next turn to uncertainty analysis. An empirical method to calculate the uncertainty associated with each of the extracted fit coefficients is to repeat the measurement many times, extract the parameters from each individual measurement, and then calculate the standard deviation across the entire set. We refer to this as the *measured uncertainty*. A faster and more broadly applicable approach to estimate the underlying parameter uncertainty is to employ the analytical formula for

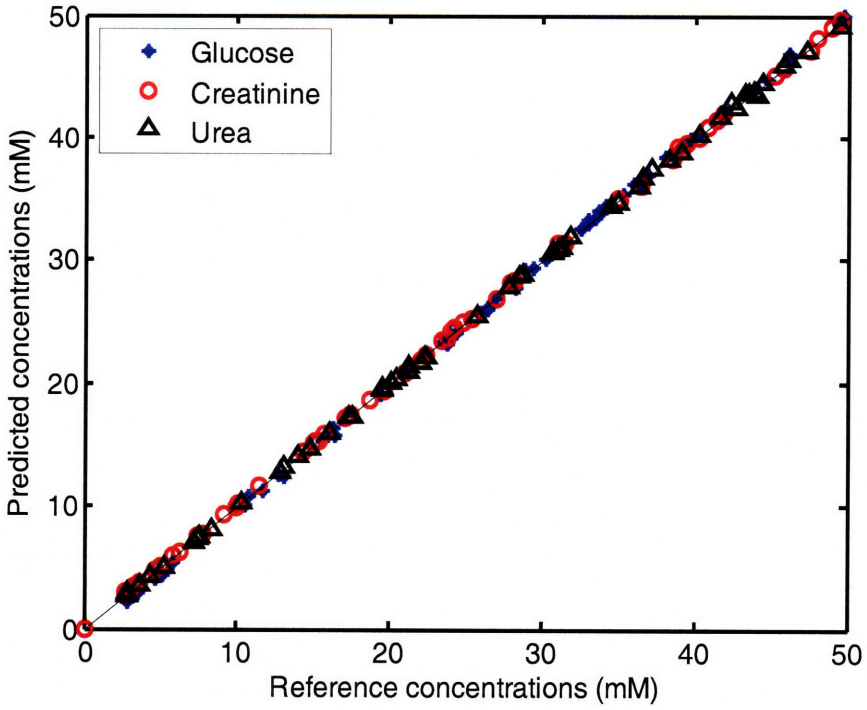

Figure 3-3. Predicted concentrations using Eq. 3.5 versus the reference concentrations for the three analytes. The predicted concentrations closely follow the reference concentrations.

Δc, Eq. (3.8). The parameter values calculated for our spectra, the noise (σ), signal (s_k), and overlap factor (olf_k), are given in Table 3.1.

To analyze how accurately Eq. (3.8) characterizes the true measured uncertainty, Fig. 3-4 plots the measured uncertainty calculated from the set of repeated measurements for all 60 mixtures versus Δc. The Δc value for each mixture in Fig. (3-4) was evaluated using an effective σ equal

	s_k ($\times 10^3$)	olf_k
Cuvette	36.1	1.61
Water	59.8	2.44
Glucose	3.58	1.51
Creatinine	4.67	1.42
Urea	3.32	1.17

Table 3.1. Necessary parameters for calculating uncertainty using Eq. (3.8). The constituent glucose, creatinine and urea spectra were measured at 53 mM concentration. The only value that varies from sample to sample is σ. The value of σ in the representative spectrum of Fig. 3-2 is 14.9.

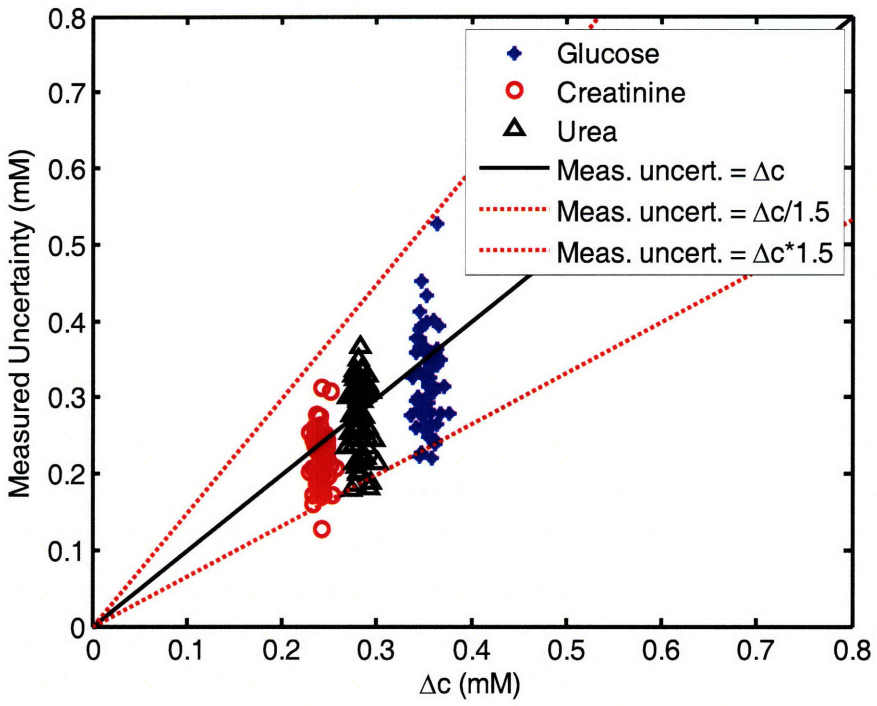

Figure 3-4. Measured uncertainty (standard deviation from repeated measurements) vs. uncertainty calculated by the analytic formula, Δc, for the three analytes. The dotted lines indicate the region for which the measured uncertainty is within a factor of 1.5 of Δc.

to the root mean squared value of the individual σ's that were calculated using Eq. (3.10) in the set of repeated measurements. The figure also indicates a 45° line (black) to reference where Δc equals the measured uncertainty, as well as two additional lines (dotted red) to indicate the region where the measured uncertainty is within a factor of 1.5 of Δc. Note that every estimated analyte concentration (Fig. 3-3) can be associated with an error bar using the Δc uncertainty (Fig. 3-4).

Measurement of diagnostic parameters.

Figure 3-5a shows a representative experimental Raman spectrum, the least squares fit using the artery morphological model, and the residual difference between the data and the fit obtained from a specimen of calcified carotid artery plaque with 0.25 seconds integration time. The measured

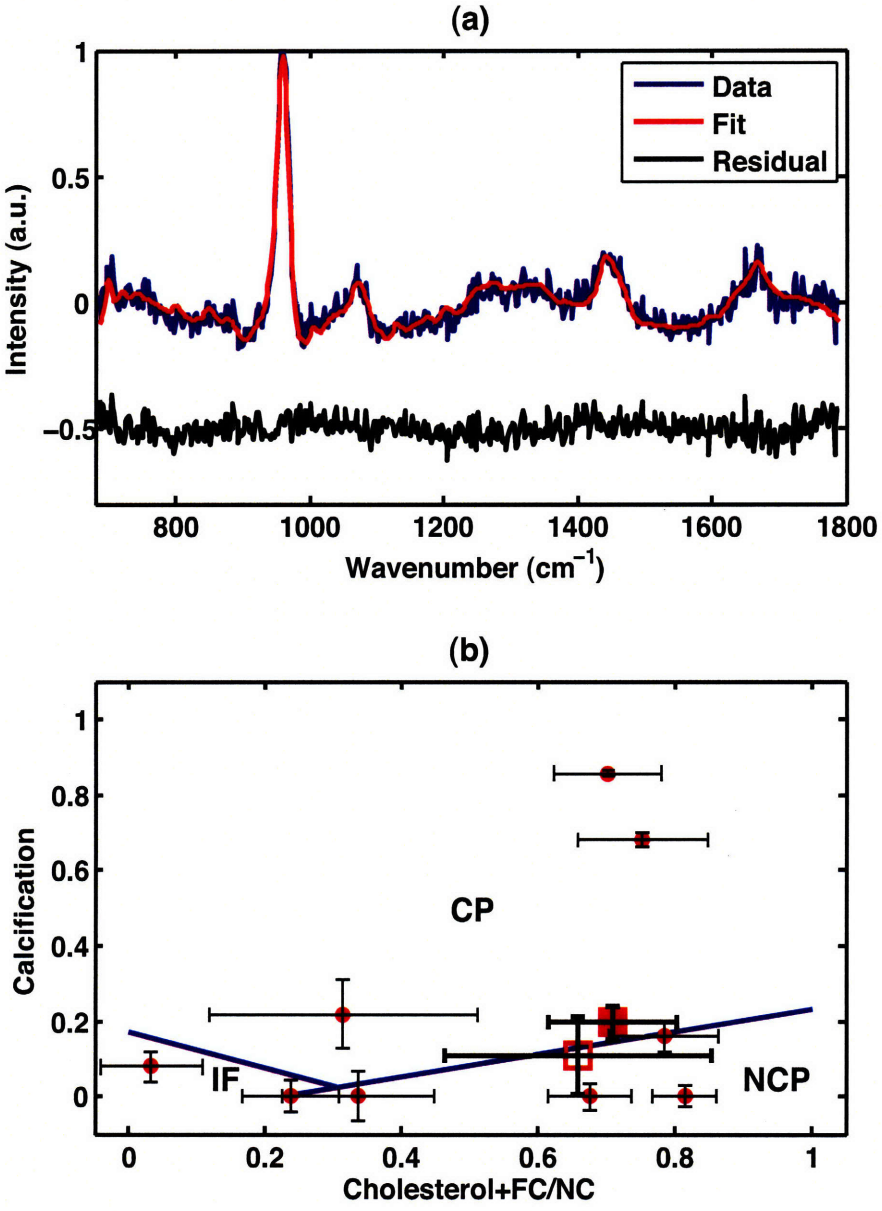

Figure 3-5. (a) Representative experimental Raman spectrum (blue), the least squares fit (red), and the residual between the data and the fit (black), obtained from a calcified carotid artery plaque in 0.25 seconds. (b) Diagnostic algorithm, showing several representative Raman artery spectra including the spectrum above (see text for details). The error bars in the two dimensions are calculated using the Δc equation. (CP = calcified plaque, NCP = non-calcified plaque, IF = intimal fibroplasia.)

uncertainty in the model fit coefficients was calculated by taking the standard deviation from the set of fit coefficients extracted from 20 consecutive measurements of 0.25 seconds each. This measured uncertainty was compared to the average uncertainty calculated by the Δc formula from Eq. (3.8) applied to any single one of the 20 independent measurements. For the representative spectrum of Fig. 3-5a, the value of σ was 0.041, s_k ranged from 2.78 to 8.89 and olf_k ranged from 1.05 to 5.83 for the set of spectral components. The measured and Δc uncertainties for this particular sample never deviated from each other by more than a factor of two.

A previously developed diagnostic algorithm [86] was applied to the fit coefficients extracted from the spectrum plotted in Fig. 3-5a. The diagnostic algorithm uses the fit coefficients from three morphological components [calcium mineralization, cholesterol crystals, and foam cells/necrotic core (FC/NC)] to classify the artery sample as being non-atherosclerotic (intimal fibroplasia), non-calcified plaque, or calcified plaque. Because only the relative intensities of the constituent Raman spectra were employed, the raw fit coefficients were normalized so that they sum to unity; in this way, the normalized fit coefficients represent the relative contributions of each morphological feature in the observed spectrum [86]. The calculated uncertainties of each raw fit coefficient were similarly scaled to provide uncertainties of the normalized fit coefficients: if $f_{norm} = a \cdot f_{raw}$, then the uncertainty propagates as $\Delta f_{norm} = a \cdot \Delta f_{raw}$. Figure 3-5b shows the diagnosis for the artery specimen with the spectrum given in Fig. 3-5a, along with diagnoses based on several other spectra from the artery data set, using the diagnostic space described earlier. The error bars in the two directions indicate the uncertainty (one standard deviation) of the normalized diagnostic fit coefficients.

■ 3.1.5 Discussion

Concentration measurements.

We first note that the values of s_k and olf_k presented in Table 3.1 make physical sense. Of the three analytes of interest, creatinine has the greatest value of $s_{creatinine}$, which indicates that it has a relatively larger Raman scattering cross section compared to the other analytes. Considering the overlap factors, we note that urea has the smallest olf_{urea}, which can be understood qualitatively by the fact that its constituent spectrum does not overlap strongly with the other constituent spectra (Fig. 3-1).

Turning to the data presented in Fig. 3-3, we note that the relatively small values of RMSEP given the large range of concentrations means that the estimator is unbiased, as expected. In addition, we find that the RMSEP values are not very different (<4%) if the data is fit using Eq. (3.3), which takes into account wavelength-dependent noise variations, rather than Eq. (3.5). (In making this comparison, Eq. (3.3) is evaluated using a noise covariance, $\mathbf{C_w}$, matrix whose diagonal elements are the calculated wavelength-dependent variances of each pixel across the set of repeated measurements while the off-diagonal covariance terms are set to zero. Because the number of repeated measurements ($\sim$ 25) was much smaller than the number of points in the spectra ($\sim$ 1000), a direct calculation of the covariance matrix results in a rank-deficient matrix. Instead of attempting to correct this by artificially boosting the diagonal elements, we found it more sensible to just use the individual variances on the diagonals and constrain the off-diagonal covariance terms to be zero, since we know that our sensors are independent.)

Figure 3-4 indicates that Eq. (3.8) provides an excellent estimate of the measured uncertainty. The measured uncertainties all lie within a factor of 1.5 of the Δc values calculated by Eq. (3.8),

as indicated by the dotted red lines in Fig. 3-4, with an average deviation of only 11%. The largest contribution to the vertical spread is due to the fact that the measured uncertainty is calculated across a limited number of measurements ($\sim$ 25), and is thus subject to its own uncertainty. We calculated the standard deviation of the estimate and found it to be from 10% to 15% of the recorded measured uncertainty. Much of the horizontal spread is due to the fact that the value of σ used in Eq. (3.8) is also calculated and is thus an estimate of the true σ. This estimate is related to the discussion of actual vs. limiting uncertainty. Any remaining deviations are likely due to subtle uncontrollable experimental factors.

We can quantify how close we are to the limiting uncertainty by comparing values of σ calculated by Eqs. (3.9) and (3.10). Across the 60 samples, the average value of σ_{act} as calculated by Eq. (3.10) is about 4% higher than the value of σ_{lim} as calculated by Eq. (3.9). Although σ_{act} is greater than σ_{lim}, the difference is very small, indicating that this measurement is very close to the limiting uncertainty. This good agreement is evidence that the linear model is valid and that measurement noise is the dominant source of uncertainty.

These results indicate that the analytical uncertainty analysis framework is an accurate and useful way of characterizing the experimental uncertainty obtainable from a single measurement. We note that great care was taken in accurately measuring the reference concentrations and minimizing spectral noise in the model, as well as in collecting the prediction spectra, thus fulfilling the necessary conditions of Eq. (3.1). Because the data pre-processing steps such as curvature correction are linear and deterministic, the assumption of uncorrelated noise holds as well for the corrected spectra as for the raw spectra. However, we observed that the distributions (of pixel intensities across multiple measurements) are only approximately Gaussian, and this may explain some of the small deviation. Other sources that account for imperfect agreement between σ_{act} and

σ_{lim} include the $\mathbf{P}$ matrix being imperfect in modeling mixtures due to chemical interactions in the solution and perhaps other minor inaccuracies in the model.

The agreement presented in Fig. 3-4 is similar to that which would result had Eq. (3.4) been used to calculate the uncertainties while using Eq. (3.3) to predict the concentrations (data not shown), using $\mathbf{C_w}$ as described above. This result, together with consistent prediction accuracy described above, underscores the validity of the initial assumption that, when noise is relatively constant across pixels, Eq. (3.5) and Eq. (3.8) are valid practical approximations to the more analytically accurate Eq. (3.3) and Eq. (3.4) for the purposes of estimating parameters and their uncertainties, respectively. In this regime, use of Eq. (3.5) and Eq. (3.8) is advantageous as it can be applied to a single spectrum, rather than requiring multiple repeated measurements in order to obtain $\mathbf{C_w}$.

Measurement of diagnostic parameters.

The Δc analysis is particularly useful for calculating uncertainty in the parameters extracted from artery tissue. This uncertainty translates into diagnostic error bars (Fig. 3-5b) that indicate the confidence of the overall diagnosis. Note that in Fig. 3-5b, one of the diagnostic dimensions is the sum of two normalized fit coefficients: cholesterol crystals and foam cells/necrotic core. The uncertainty of the sum involves the uncertainties (variances) of each individual fit coefficients as well as the covariance of the two, which is specified by the off-diagonal terms of the matrix in Eq. (3.6).

Consider two specific specimens which are located on opposite sides of the decision line between calcified and non-calcified plaque, represented by open and solid squares in Fig. 3-5b. Without knowledge of the uncertainty in these assignments, one cannot be more or less confident of either classification assignment. The Δc analysis allows for both qualitative and quantitative assessment

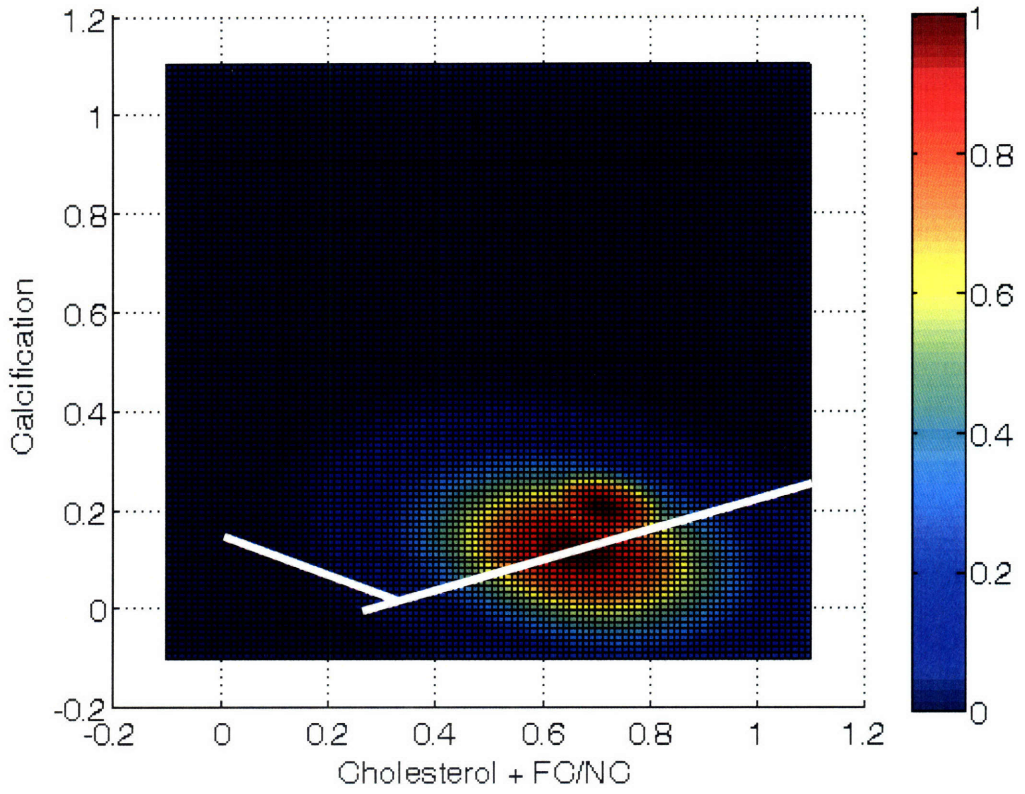

Figure 3-6. The diagnostic probability distributions for the solid and open square from Fig. 3-5b. The mean of each bivariate Gaussian distribution is specified by the fit coefficients while the covariance is specified by the relevant elements of Eq. (3.6).

of the confidence of the diagnosis by assignment of error bars, which effectively specify a probability distribution. If we assume a bivariate Gaussian distribution specified by mean corresponding to the fit coefficients and covariance matrix calculated by Eq. (3.6), as shown in Fig. 3-6, we calculate the probability of the solid square specimen being calcified as 80%. Similarly, we calculate the probability of the open square specimen being non-calcified as 60%. For simplicity, here we have considered that the classification algorithm is perfect, meaning there is absolute certainty about the decision, regardless of proximity to the decision line. However, in practice there is an additional probability associated with classification that arises from an imperfect decision line. Therefore, a

more rigorous approach would be to use this classifier probability as a weighting factor on the data point probability in calculating diagnostic confidence.

We note that the value of σ_{act} is on average 15% higher than σ_{lim} for the 17 artery specimens examined, a somewhat larger discrepancy than that observed for the concentration measurements. Although data pre-processing steps are linear and deterministic, thus preserving the assumption about uncorrelated noise, the tissue Raman spectra are fit after interpolation and binning, which could undermine that assumption. Therefore, we calculated the changes in σ_{act} and σ_{lim} before and after interpolation, but found only a small difference (<5%) between the two. We attribute the remaining differences between σ_{act} and σ_{lim} to minor structure in the residuals that result in artificially high calculated values of σ_{act}. This finding is not surprising when considering the complex nature of tissue modeling and indicates that there is room for improvement in the modeling.

Another factor that may help explain the larger discrepancy between σ_{act} and σ_{lim} for tissue Raman measurements is the fluorescence removal pre-processing step. Although this procedure has been used in numerous previous studies [86, 89, 94], removing tissue fluorescence by means of fitting and subtracting a 6^{th} order polynomial from the raw data may introduce some unwanted spectral distortions. These spectral distortions, though surely small, may translate into an overestimate of σ_{act}. Perhaps a more accurate way to remove tissue fluorescence may be by utilizing the method of frequency shifting, described elsewhere [145]. The method of frequency shifting, or other more advanced mathematical methods [146], may be explored in future work to address the discrepancy between σ_{act} and σ_{lim} for tissue measurements.

General comments.

Knowledge of the limiting uncertainty also provides the limit of detection. For example, under the stated assumptions, if we calculate a value of Δc for a particular sample, we can be reasonably certain of detecting parameters (concentrations or fit coefficients) on the order of $\geq 3\Delta c$. This quantity specifies the lowest concentration of an analyte such as glucose that can be detected in a mixture solution or, equivalently, the smallest contribution of a morphological pure component from a tissue sample.

The differences between the actual and limiting uncertainties can be broken down into three cases. In the first case, $\sigma_{act} \approx \sigma_{lim}$ and the residuals are featureless. This implies that $\Delta c_{act} \approx \Delta c_{lim}$, indicating that the measurements are being made with minimal uncertainty. Given the small difference between σ_{act} and σ_{lim} for the concentration measurements presented, we can conclude that these measurements fall in this category. The second case is that $\sigma_{act} > \sigma_{lim}$ and the residuals are nearly featureless. This implies that there is noise in the model components that can be further reduced. This case would hold true in applications where the constituent spectra were not measured directly but rather obtained through PCR, for example; thus, the spectral components (principal components) may be noisy and add to measurement noise. Even for direct measurements of the spectral components, a particular component spectrum may contain more noise than others and may need to be collected again. Most of the artery tissue measurements fall in this category, and the uncertainty analysis should guide improvements in modeling until the limiting uncertainty is reached. Lastly, the third case where $\sigma_{act} > \sigma_{lim}$ and the residuals have structure means that there are model components missing or there is some other error in the pre-processing of the data. Some infrequent tissue spectra fall in this category as tissue is very heterogeneous, especially when analyzing disease progression. In this case, careful understanding of the sample properties and

variation, as well as accurate modeling, is needed to bring the uncertainty down to the limiting level.

As mentioned earlier, the limiting uncertainty can also be expressed in terms of parameters extracted by indirect calibration (such as PLS), that depend on measurement noise and the b-vector [135]. The present paper provides a natural extension to those results by demonstrating the applicability of a more general formula, Eq. (3.8), that arises naturally from the CRLB concept and that effectively breaks up the b-vector from Ref. [135] into the signal strength and spectral overlap contributions. When only indirect calibration is possible, such as for concentration measurements in solutions where individual spectral contributions of the constituents cannot be measured directly, the formula from Ref. [135] should be used. When both direct and indirect calibration are possible, both the formula from Ref. [135] and Eq. (3.8) can be used; this way, the formulas can be utilized to test and compare the robustness of indirect (PLS) and direct (OLS) prediction methods. Lastly, when indirect calibration is not possible but the spectral models are measurable, such as for extracting model parameters from samples including human tissue where reference contributions of particular morphological features are almost impossible to obtain, either formula can be used to calculate parameter uncertainty. In fact, the two equations provide exactly the same ultimate mathematical result. However, the advantage of using Eq. (3.8) is that it provides physical insight into the signal strength and spectral overlap effects on the b-vector. As described earlier, the χ^2 approach can always be used to estimate the uncertainty by doing several constrained fits; however, the method is statistical and does not have a functional dependence, hence it cannot provide insight to the nature of the uncertainty.

The demonstration of experimental uncertainty being very close to Eq. (3.8) for the concentration measurements indicates the precision of our experimental apparatus and can be used to guide

instrument improvements. For example, increasing the slit width of a spectrograph increases the overlap factor by blurring the Raman peaks, but also increases the signal strength. This trade-off should guide instrument optimization to yield the minimum extracted parameter uncertainty. Such improvements are crucial in developing multimodal spectroscopy systems that require real-time error assessments of parameters extracted from multiple spectral modalities [131].

■ 3.2 Nonlinear fitting - DRS

■ 3.2.1 Theory

The preceding sections were based on the linear model assumption from Eq. (3.1). However, in a generalized nonlinear problem, such as fitting DRS spectra, where we have:

$$\mathbf{s} = f_{nl}(\mathbf{c}) + \mathbf{w}, \tag{3.12}$$

the analytical approach presented in Sec. 3.1 does not apply. While it is possible to linearize a nonlinear problem around a particular operating point, this would result in a loss of accuracy for DRS measurements owing to a wide dynamic range of physically observable DRS signals. We can still proceed to find the optimal estimator $\hat{\mathbf{c}}$ by optimization of the χ^2 error metric from Eq. (3.11):

$$\hat{\mathbf{c}} = \arg\min_{\hat{\mathbf{c}}}(\chi^2) \tag{3.13}$$

The uncertainty in each parameter $\hat{c}_k$ is determined from the curvature of χ^2 as a function of $\hat{c}_k$. Once we obtain the optimum value for $\hat{c}_k$ from Eq. (3.13), the χ^2 values can be calculated for different constrained values of $\hat{c}_k$ close to the optimum by optimizing over all the other $\hat{c}_j$ for j≠k; this $\chi^2(\hat{c}_k)$ function is quadratic in the vicinity of its minimum [103, 143]. The standard deviation

of the uncertainty or error in the estimate $\hat{c}_k$ is related to the curvature by:

$$std(\hat{c}_k) = \sqrt{2\left(\frac{d^2}{d\hat{c}^2}\chi^2\right)^{-1}_{(k,k)}} \tag{3.14}$$

This uncertainty can be calculated easily by constraining the value above and below the optimum for each parameter, redoing optimizations over the remaining degrees of freedom, generating the χ^2 function, and calculating the square root of the reciprocal of its curvature. Alternatively, using standard optimization routines (such as *fmincon* in MATLAB) with χ^2 as the objective function, the second derivative (Hessian matrix) of χ^2 at its minimum value would give the equivalent uncertainty.

■ 3.2.2 Results and Discussion

A simulated example is given here for the nonlinear model using DRS. We start with the true coefficients that define the DRS signal. The scattering parameters (A, B, C) specify the μ_s' through Eq. (2.4) and the absorption parameters ($[HbO_2]$ and $[\beta - car]$) specify the μ_a through Eq. (2.3). These values are given in Fig. 3-7 under "Original." Then, a level of Gaussian noise of a known standard deviation was added, resulting in the blue spectrum shown in Fig. 3-7. The spectrum was fit using the model of Zonios [66] specified in Eq. (4.3) as the f_{nl} in Eq. (3.13). The fit coefficients extracted by minimizing the χ^2 in (3.13) are shown under "FC". The values of extracted coefficients were constrained to the range specified in "Range" to insure convergence of the nonlinear model. The uncertainty is given in the last column ("Error") and is equivalent to performing the procedure many times of adding a different instance of noise of the same standard deviation, extracting the fit coefficients for each experiment, and calculating the standard deviation statistics across all the fit coefficients; this is analogous to the *measured uncertainty* defined earlier. This uncertainty can be calculated equivalently from just one measurement using the empirical error analysis (3.14), using

the χ^2 parabolas generated for all the coefficients, as demonstrated in the middle and bottom right panels. The agreement between the measured and calculated uncertainty holds again.

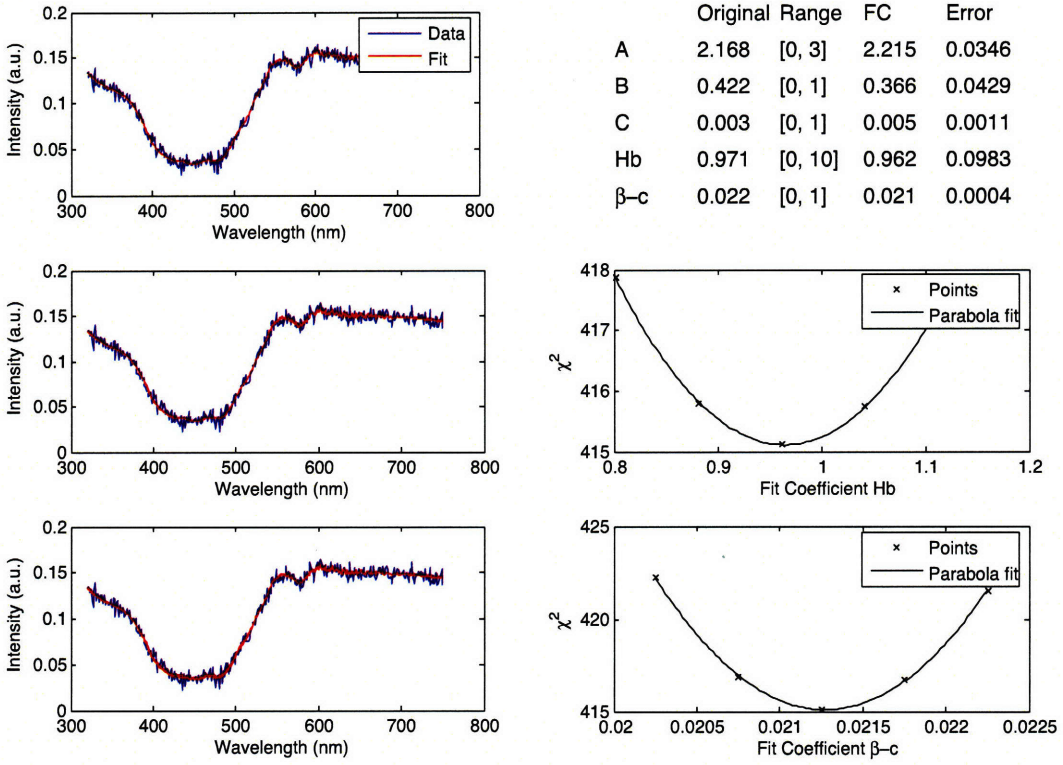

	Original	Range	FC	Error
A	2.168	[0, 3]	2.215	0.0346
B	0.422	[0, 1]	0.366	0.0429
C	0.003	[0, 1]	0.005	0.0011
Hb	0.971	[0, 10]	0.962	0.0983
β–c	0.022	[0, 1]	0.021	0.0004

Figure 3-7. Uncertainty analysis example in for nonlinear measurements (DRS). The blue noisy simulated data is calculated from the nonlinear DRS model that takes inputs (A, B, C, $[HbO_2]$, $[\beta-car]$) with the given true coefficients ("Original"). The extracted fit coefficients are given in "FC" with the uncertainty associated with each estimate in "Error".

■ 3.3 Relation between χ^2 and Δc

The MVU estimator is equivalent to the ML estimator for the linear model described earlier [138]. In this section, we demonstrate that the standard deviation of the estimator obtained analytically (Δc) is the same as that obtained through χ^2 analysis. The χ^2 value is defined in Eq. (3.11) and the associated ML estimator is determined by minimizing this value as given by Eq. (3.13). Specializing to our linear model, Eq. (3.1), and recognizing the fit as $\mathbf{P}\hat{\mathbf{c}}$, we can express χ^2 in the

form of an inner product:

$$\chi^2 = \frac{(\mathbf{s}\text{-}\mathbf{P}\hat{\mathbf{c}})^T(\mathbf{s}\text{-}\mathbf{P}\hat{\mathbf{c}})}{\sigma^2}. \tag{3.15}$$

The second derivative of χ^2 with respect to our estimate $\hat{\mathbf{c}}$ has a particularly useful form. Noting that:

$$\frac{d^2}{d\hat{\mathbf{c}}^2}\chi^2 = \frac{d^2}{d\hat{\mathbf{c}}^2}\frac{(\mathbf{P}\hat{\mathbf{c}})^{\mathbf{T}}(\mathbf{P}\hat{\mathbf{c}})}{\sigma^2} = \frac{d^2}{d\hat{\mathbf{c}}^2}\frac{\hat{\mathbf{c}}^{\mathbf{T}}(\mathbf{P}^{\mathbf{T}}\mathbf{P})\hat{\mathbf{c}}}{\sigma^2}, \tag{3.16}$$

and using the general property, $\frac{d^2}{d\mathbf{x}^2}\mathbf{x}^{\mathbf{T}}\mathbf{A}\mathbf{x} = (\mathbf{A}+\mathbf{A}^{\mathbf{T}})$ and Eq. (3.6), we can simplify the derivative quantity to:

$$\frac{d^2}{d\hat{\mathbf{c}}^2}\chi^2 = \frac{2(\mathbf{P}^{\mathbf{T}}\mathbf{P})}{\sigma^2} = 2 \cdot cov(\hat{\mathbf{c}})^{-1}. \tag{3.17}$$

Note that $\frac{d^2}{d\hat{\mathbf{c}}^2}\chi^2$ is a Hessian matrix whose (i, j) entry specifies $\frac{d^2}{d\hat{c}_i\hat{c}_j}\chi^2$. This matrix is used by standard optimization techniques and, as we shall see, is particularly useful when evaluated at the minimum χ^2 value. Dividing by 2, inverting, specializing to the kth diagonal component, and taking the square root, we obtain:

$$\sqrt{2\left(\frac{d^2}{d\hat{\mathbf{c}}^2}\chi^2\right)^{-1}_{(k,k)}} = std(\hat{c}_k) \equiv \Delta\hat{c}_k \tag{3.18}$$

This expression demonstrates the connection between the Δc and χ^2 analysis of uncertainty. That is, the curvature of χ^2 (as function of $\hat{c}_k$) is inversely proportional to the variance of the kth estimator $\hat{c}_k$. If we had not made the simplifying assumption that $\mathbf{C_w} = \sigma^2\mathbf{I}$ for the noise vector $\mathbf{w}$ in Eq. (3.1), we could still follow an analogous mathematical approach as shown above to demonstrate that the curvature of χ^2 specifies the covariance as given by the more general formula of Eq. (3.4). In this case, Eq. (3.17) would become:

$$\frac{d^2}{d\hat{\mathbf{c}}^2}\chi^2 = \frac{2(\mathbf{P}^{\mathbf{T}}\mathbf{C}_{\mathbf{w}}^{-1}\mathbf{P})}{\sigma^2} = 2 \cdot cov(\hat{\mathbf{c}})^{-1}, \tag{3.19}$$

and the final result of Eq. (3.18) still follows.

■ 3.4 Summary

We have described a simple and direct method for calculating the uncertainty from a single spectroscopic measurement and demonstrated its experimental usefulness, both for solution mixtures and human tissue. Not only does the analytic Δc expression, Eq. (3.8), provide a means of calculating parameter uncertainties, but it also assesses the calibration and consistency of the experimental apparatus. Because the expression from Eq. (3.8) is the CRLB, it represents the ultimate lower bound on the uncertainty of parameters extracted from a linear system by an unbiased estimator. Analytical expressions for characterizing uncertainty for nonlinear fitting, such as modeling diffuse reflectance spectroscopy measurements, are also presently under investigation.

■ 3.5 Acknowledgements

Dr. Kate Bechtel collected all the Raman spectra from the aqueous solutions and helped with the analysis and interpretation. Dr. Sourav Dey provided helpful insights on topics in estimation theory. Dr. Wei-Chuan Shih provided helpful insights in chemometrics. Many of the figures and text were reproduced from the *Journal of Biomedical Optics* [147] with permission from SPIE. This research was conducted at the MIT Laser Biomedical Research Center under NIH Grant No. P41-RR-02594.

Chapter 4

MMS probe development

The MMS probe design builds off the design of the Raman probe and appropriately modifies it to enable efficient delivery and collection of DRS and IFS in the UV/visible wavelength region. However, as a result of this modified excitation/collection geometry, compared to that of the FastEEM probe, the modeling of DRS and IFS spectra collected with this probe needs to be adjusted to enable correct extraction of spectral parameters. This chapter is divided into three sections: 1) overview of the Raman probe design, 2) description of the MMS probe design, and 3) the modeling modifications for DRS and IFS in the MMS probe geometry.

4.1 Previous design - Raman probe

This section summarizes the previously developed design of the Raman probe. More detailed information can be found elsewhere [127, 87].

4.1.1 Overview

As Raman signals are weak, conventional fluorescence/reflectance probes cannot be used. The intense excitation light traversing the delivery optical fiber creates a very large background. Without proper filtering, this background will be back-reflected by the tissue into the collection fiber(s), overwhelming the Raman signal generated in the tissue. Furthermore, the excitation light back-reflected

from the tissue will generate additional fiber background on its return path, again obscuring the Raman signal collected from the tissue. In addition, the probe tip must be properly engineered to collect as much of the weak Raman signal generated in the tissue as is possible. The probe must also be sufficiently flexible to access narrow vessels such as the coronary arteries, and its diameter must be small (< 2 mm).

■ 4.1.2 Optical filters

The optical fiber background is removed by inserting optical filters in the distal tip. The excitation fiber is filtered with a short wavelength-pass filter that transmits the excitation laser light (830 nm) and blocks the background light generated in the probe. Conversely, the collection fibers are filtered with a long wavelength-pass filter that blocks the Rayleigh-scattered light and transmits the Raman light generated in the tissue. These filters are mounted in the distal end of the probe by means of a custom designed filter module that provides optical isolation between the various components.

The problem of fused silica background can be circumvented by collecting Raman signals in the high wave number region (2400-3800 cm^{-1}) rather than the fingerprint region (400-1800 cm^{-1}), thus enabling the use of a single unfiltered fiber for both excitation and collection [114]. However, this approach comes at the expense of losing potentially critical spectral information that is only present in the fingerprint region. Since all of our previous model development has utilized the fingerprint region to characterize Raman spectra of artery tissue and since the fingerprint region arguably contains more spectral variation, we have chosen to pursue the filtered probe design.

■ 4.1.3 Optical system design

The optical design process aims to conserve light throughput (the product of collection solid angle and cross-sectional area at any point along the optical train) while maximizing collection efficiency. System throughput is limited by the slit area and numerical aperture (NA) of the spectrograph. Optical element(s) at the probe tip are needed to efficiently couple the Raman light generated in the tissue to the collection fibers. This is achieved by using a central excitation fiber surrounded by a ring of collection fibers, which are matched in NA to the spectrograph. The excitation fiber NA was chosen to minimize the fiber and cladding background, and an appropriate diameter was selected to insure safe fluence levels and, for optimal collection, to limit the size of the delivery spot on the tissue surface. In order to design the probe collection optics, we need to determine the optimal collection geometry. Experiments show that the Raman light scattered from the tissue was approximately separable in emission angle and radius. Artery tissue experiments and numerical simulations are then performed to determine the efficiency of light collection from the tissue. Maximum collection efficiency, achieved at a 90° collection angle and 0.19 mm radius, is found to be 8.6%. This collection is achieved by means of a sapphire ball lens attached to the probe tip.

■ 4.1.4 Technical implementation

The central excitation fiber is optically isolated from the ring of 15 collection fibers by means of an aluminum jacket. All of the fibers have 200 μm core diameter. The excitation fiber NA is 0.22, whereas the collection fiber NA is 0.26, for reasons described above. The filter module is composed of a short-pass filter rod that fits snugly into a long-pass filter tube, both dielectrically coated. The filter module is attached to the fibers with index-matching optical cement. The sapphire ball lens is tightly secured at the probe tip, and positioned an appropriate distance from the fibers to insure

a collimated beam of excitation light and efficient collection of light emitted from the tissue. All of the probe components are custom fabricated using medical-grade materials that that can withstand clinical sterilization. The probe is 4 m long and less than 3 mm in overall diameter.

■ 4.1.5 Probe performance

Optical design simulations were used extensively to guide probe development, achieve a clinically acceptable excitation spot diameter, and maximize collection efficiency. Probe performance was also tested experimentally. Known Raman scatterers such as barium sulfate were used to evaluate the performance of the filters. Tissue phantoms were also employed, using models found in the literature to evaluate the impact of scattering and absorption on the signal and background. Finally, Raman spectra were taken from samples of artery tissue using 100 mW delivery power and 1 s collection, and fit with the appropriate models. The excellent quality of spectra collected in only 1 s demonstrates the feasibility of clinically implementing Raman spectroscopy [87, 88, 89].

■ 4.2 MMS probe design

The schematic of the MMS probe, which is very similar to that of the Raman probe, is shown in Fig. 4-1. This design is that of a front-viewing probe; for more information about side-viewing probes, refer to Sec. 8.2.1. The MMS probe is different from the Raman probe in several ways: 1) the optical fibers that are used for delivery and collection, 2) the filter characteristics of the excitation rods and collection tubes, and 3) the type of adhesives used to glue the components in the probe tip.

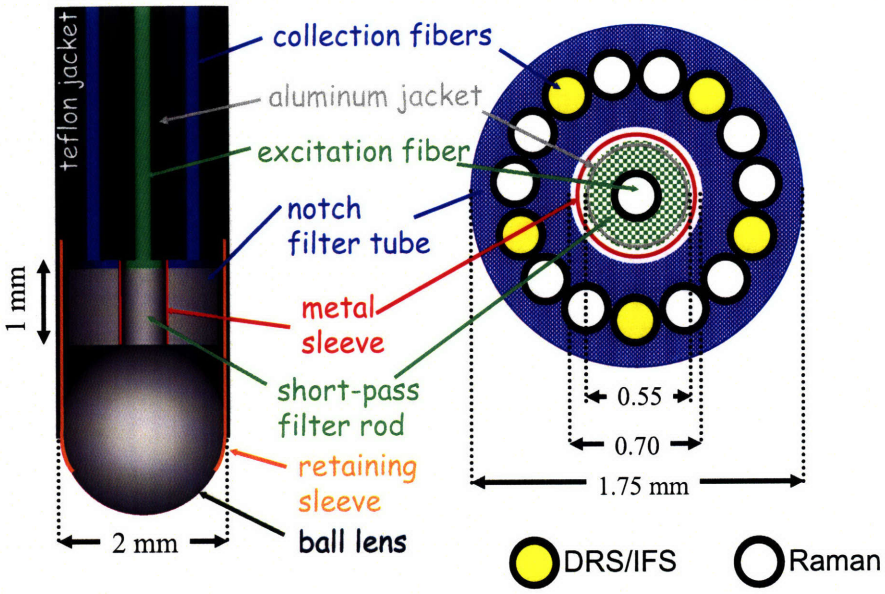

Figure 4-1. The schematic of the MMS probe, with the side view of the left and a cross sectional view on the right. The single central excitation fiber (200 μm diameter, 0.22 NA) is optically isolated from the 15 collection fibers, 10 of which (200 μm diameter, 0.26 NA) are used for Raman spectra collection and 5 of which (200 μm diameter, 0.22 NA) are used for DRS and IFS collection. The probe tip contains a filter module to appropriately filter the excitation and collection fibers and a sapphire ball lens to optimize collection.

■ 4.2.1 Optical fibers

Owing to the broad range of wavelengths of light used, the MMS probe fibers needs to be optimized for the particular modalities. The central excitation fiber needs to efficiently transmit excitation light in the range 300-830 nm so the Superguide fiber (200 μm diameter, 0.22 NA, Fiberguide Industries, Stirling, NJ) is used. On the collection side, the collection fibers need to be split in a way to optimize some for transmission in the visible wavelength range and the rest for transmission in the NIR wavelength range. The collection fibers can thus be optimized based on modalities, so the Superguide fibers are used for the visible (DRS/IFS) and Anhydroguide fibers (200 μm diameter, 0.26 NA, Fiberguide Industries, Stirling, NJ) are used for the NIR (Raman). Therefore, out of the 15 collection fibers, five fibers are dedicated for DRS/IFS while 10 are dedicated for

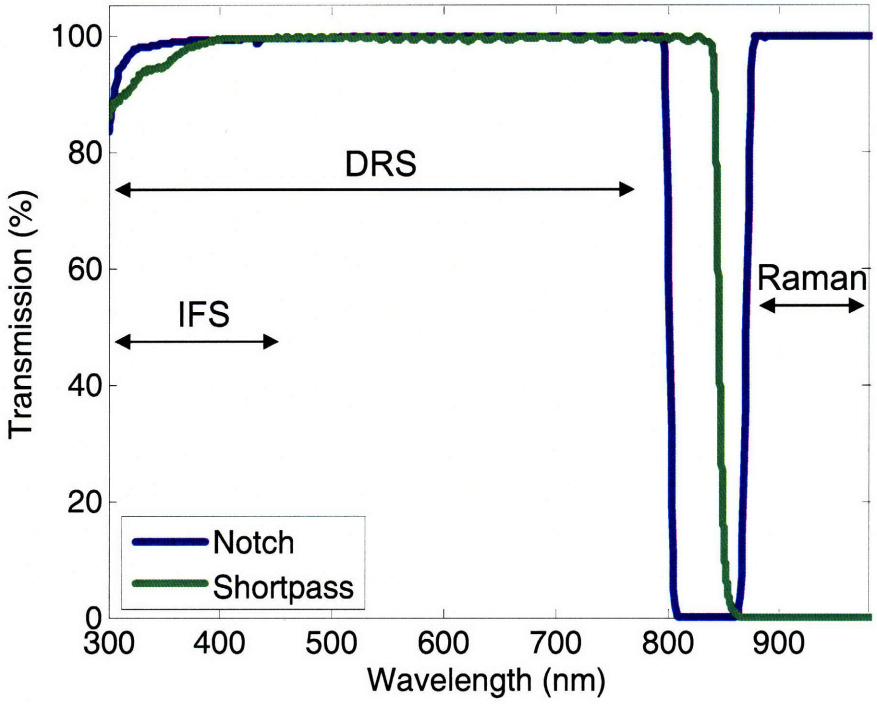

Figure 4-2. The filter characteristics of the MMS probe. The excitation fiber light is filtered by a shortpass filter that transmits 300-830 nm light and blocks light > 850 nm. The collection fiber tube contains a notch filter that transmits 300-800 nm and 850-1000 nm while blocking light around the Raman laserline (830 nm).

Raman. This would allow almost equivalent signal collection with the single MMS probe as with the individual FastEEM and Raman probes used individually in previous studies.

■ 4.2.2 Filter characteristics

The filters in the MMS probe are still constrained by the need for efficient extraction of Raman signals. However, both the excitation and collection filters need to transmit the visible range 300-800 nm. Hence, the excitation fiber rod contains a shortpass filter that transmits 300-830 nm light and blocks light > 850 nm. Analogously, the collection fiber tube contains a notch filter that transmits 300-800 nm and 850-1000 nm while blocking light around the Raman excitation wavelength (800-850 nm). The described filter characteristics are shown in Fig. 4-2. These filters

are custom manufactured (Barr Associates, Westford, MA) and deposited onto polished fused silica pieces. The shortpass filter is deposited onto a cylindrical (0.5 mm diameter, 1 mm length) "rod," while the notch filter is deposited onto a donut-shaped (inner diameter 0.7 mm, outer diameter 1.8 mm, length 1 mm) "tube."

■ 4.2.3 Adhesives

Previously, sodium silicate or epoxy were used in the Raman probe design to glue the rods and tubes to the fibers. Ultimately, epoxy was deemed more optimal as a result of its durability and optical properties. However, ordinary epoxy is not optically clear in the UV wavelength range. As a result, a special epoxy (Epo-tek 305, Epoxy Technology, Billerica, MA) is used for the MMS probe. Note that that a ball lens made of sapphire is still optimal for the MMS probe as sapphire is optically clear in the range 300-1000 nm. The ball lens is not glued in the probe but instead held by means of the stainless steel retaining sleeve.

■ 4.3 Modeling modifications

In the past, DRS and IFS spectra were collected only with the unfiltered, six collection fibers around one excitation fiber, FastEEM probe with a 1.5 mm long quartz shield at the tip. Specifically, the probe geometry was such that the excitation and collection spots on the sample can be treated as two partially overlapping circles. The DRS modeling developed by Zonios *et al.* [66] was dependent on this probe geometry. Now, with the ball lens of the MMS probe, the excitation/collection geometry has changed, specifically by decreasing the source-detector separation as well as the range of angles that can be collected. The IFS modeling could in principle stay the same as presented by Zhang *et al.* [80], with modifications done for several probe-specific parameters. Therefore, the modeling

for both DRS and IFS in this new probe geometry needed to be revisited so that each MMS probe could be calibrated appropriately to insure the accurate extraction of tissue parameters.

■ 4.3.1 DRS modeling

This section describes the diffusion theory modeling for DRS and the associated probe calibration procedure.

Diffusion theory model for DRS

Farrell *et al.* calculated the diffuse reflectance from a narrow beam of light incident on the surface of a semi-infinite turbid medium in the diffusion approximation [67]. The following expression is the Green's function $R(\lambda, r)$, in units of radial density (mm^{-2}), at a distance r from the point of incidence:

$$R(\lambda, r) = \frac{z_0}{4\pi} \frac{\mu_s^{'}}{(\mu_s^{'} + \mu_a)} \left[\left(\mu + \frac{1}{r_1} \right) \frac{e^{-\mu r_1}}{r_1^2} + \left(1 + \frac{4}{3} A \right) \left(\mu + \frac{1}{r_2} \right) \frac{e^{-\mu r_2}}{r_2^2} \right], \tag{4.1}$$

with

$$\mu = \sqrt{3\mu_a(\mu_a + \mu_s^{'})}, \qquad z_0 = \frac{1}{\mu_s^{'} + \mu_a},$$

$$r_1 = \sqrt{z_0^2 + r^2}, \qquad r_2 = \sqrt{z_0^2 \left(1 + \frac{4}{3} A \right)^2 + r_2^2}.$$

The parameter A depends on the refractive index of the tissue and is assumed to be $A \cong 3.2$ [66]. It should be noted explicitly that all μ quantities are functions of wavelength. In order to calculate the reflectance collected by a probe, $R_p(\lambda)$, the above Green's function must be integrated over the delivery and collection areas, characterized by radii r_d and r_c, respectively, and normalized by the

delivery area (πr_d^2) to obtain the unitless reflectance:

$$R_p(\lambda) = \frac{1}{\pi r_d^2} \int_0^{2\pi} d\phi_c \int_0^{r_c} r dr \int_0^{2\pi} d\phi_d \int_0^{r_d} R\left(\lambda, \left|r - r^{'}\right|\right) r^{'} dr^{'}, \tag{4.2}$$

where $\left|r - r^{'}\right|$ specifies the distance between a point on the delivery area and a point on the collection area. The parameters r_d and r_c are probe-specific parameters that are to be determined by calibration. Equation. (4.2) can be evaluated numerically but it can further simplified the equation by making the approximation of point source delivery ($r_d << 1$). With this approximation, Zonios *et al.* obtained a closed form solution [66] for the reflectance collected by a probe:

$$R_p(\lambda) = \frac{1}{2} \frac{\mu_s^{'}}{(\mu_s^{'} + \mu_a)} \left\{ e^{-\mu z_0} + e^{-(1+\frac{4}{3}A)\mu z_0} - z_0 \frac{e^{-\mu r_1^{'}}}{r_1^{'}} - \left(1 + \frac{4}{3}A\right) z_0 \frac{e^{-\mu r_2^{'}}}{r_2^{'}} \right\}, \tag{4.3}$$

with $r_1^{'} = \sqrt{z_0^2 + r_c^{'2}}$ and $r_2^{'} = \sqrt{z_0^2 \left(1 + \frac{4}{3}A\right)^2 + r_c^{'2}}$. The parameter $r_c^{'} \cong r_c$ is the effective collection radius and is a probe-specific parameter that is also determined by calibration.

To avoid confusion, when the two values of r_d and r_c are discussed, it is in the context of the model of Farrell *et al.*. On the other hand, the single value of $r_c^{'}$ is germane to the model of Zonios *et al.*, which assumes that $r_d \approx 0$.

Parameter calibration strategy

In either Eq. (4.2) or Eq. (4.3), we see that the reflectance collected by a probe, $R_p(\lambda)$, is a function of tissue-specific parameters ($\mu_s^{'}$ and μ_a) and probe-specific parameters (r_d and r_c, or $r_c^{'}$). Our objective is to accurately extract the $\mu_s^{'}$ and μ_a given a $R_p(\lambda)$, which requires the knowledge of the probe-specific parameters. We calculate the probe-specific parameters by means of a calibration procedure presented in Fig. 4-3. First, a calibration set of tissue phantoms is used to determine

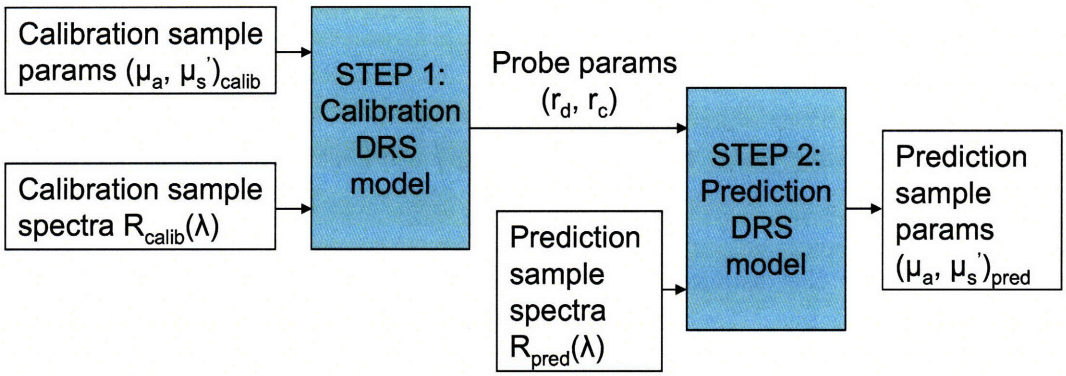

Figure 4-3. The probe calibration procedure. First, a calibration set of tissue phantoms is used to determine the probe-specific parameters, r_d and r_c. Then, these probe-specific parameters are used prospectively on tissue spectra to accurately extract μ_s' and μ_a.

the probe-specific parameters, r_d and r_c. These phantoms are designed to mimick tissue optical properties. By recording DRS spectra of these tissue phantoms and accurately knowing their μ_s' and μ_a, one can infer the optimal values of r_d and r_c that correspond to that particular probe. Then, these probe-specific parameters are held fixed and used prospectively to extract μ_s' and μ_a from spectra of tissue with unknown optical properties. The next several sections describe the phantom experiments that ultimately yield the r_d and r_c values for the MMS probe.

Phantom preparation

Five phantoms were prepared to mimick artery tissue reflectance properties. Polystyrene beads with 1 μm diameter and 1% solids by volume (64030 Polysciences, Warrington, PA) were used to simulate scattering. A concentrated solution (8 mg/ml) of hemoglobin, created by dissolving 12 mg of dry hemoglobin (H0267, Sigma-Aldrich, St. Louis, MO) with 1.5 ml of deionized H_2O, was used for absorption. The five phantoms included variations of scattering amplitude and hemoglobin concentration, and the mixture proportions are given in Table 4.1. Note that the scattering in phantoms 1 and 2 is equivalent, just as is the scattering of phantoms 3 and 4. Analogously, the

Phantom	Beads (ml)	Hb (ml)	H_2O (ml)
1	1.4	0.2	1.2
2	1.4	0.4	1.0
3	1.0	0.2	1.6
4	1.0	0.4	1.4
5	1.2	0	1.6

Table 4.1. The mixture of beads, hemoglobin solution and deionized water that resulted in the five phantoms used to calibrate DRS probe-specific parameters. The volume of beads indicate amount of 1% solids solution and the volume of hemoglobin indicate amount of 8 mg/ml stock solution.

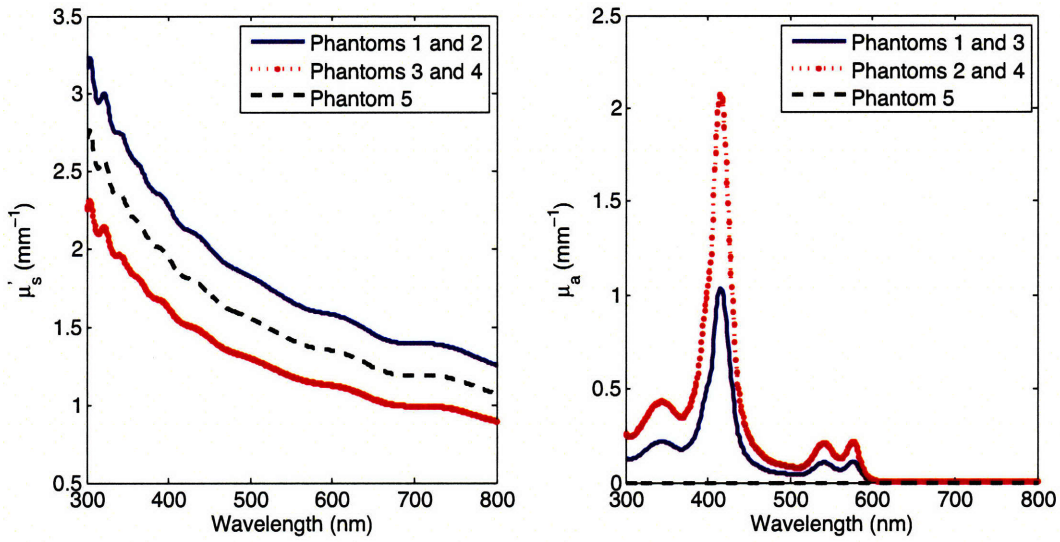

Figure 4-4. The μ_s' and μ_a values for the five phantoms mixed in the proportions described in Table 4.1.

absorption of phantoms 1 and 3 is equivalent (0.57 mg/ml), just as is the absorption of phantoms 2 and 4 (1.14 mg/ml). Phantom 5 contains an intermediate level of scattering and no absorption. Those levels of scattering an absorption translate into the $\mu_s'(\lambda)$ and $\mu_a(\lambda)$ given in Fig. 4-4. The $\mu_s'(\lambda)$ values are calculated using a standard Mie code that evaluates the total scattering cross section $\sigma_s(\lambda)$, which translates into $\mu_s'(\lambda)$ with the following relation:

$$\mu_s'(\lambda) \equiv \mu_s(\lambda)(1-g) = \rho_s \sigma_s(\lambda)(1-g), \tag{4.4}$$

where ρ_s is the density of beads in the solution, g is the beads anisotropy parameter calculated from the scattering phase function, and $\sigma_s(\lambda)$ is a function of the bead size and refractive index mismatch between the beads and water [68]. In modeling the $\mu_s^{'}(\lambda)$ in tissue where the scatterer properties are unknown *a priori*, a more general power-law relation can be used [123, 124]:

$$\mu_s^{'}(\lambda) = A \cdot \left(\frac{\lambda}{\lambda_0}\right)^{-B}, \tag{4.5}$$

where A and B specify the power law function and $\lambda_0 = 1$ μm is a normalization factor. The $\mu_a(\lambda)$ parameter is calculated using the following equation:

$$\mu_a(\lambda) = (log_e 10) c_{Hb} \left(\alpha \epsilon_{HbO_2}(\lambda) + (1-\alpha)\epsilon_{Hb}(\lambda)\right), \tag{4.6}$$

where c_{Hb} is the concentration of hemoglobin, α is oxygen saturation of hemoglobin, and $\epsilon_{HbO_2}(\lambda)$ and $\epsilon_{Hb}(\lambda)$ are the extinction spectra of oxygenated and deoxygenated hemoglobin, respectively.

Calibration: finding probe-specific r_d and r_c

The phantoms were mixed in small glass vials and thoroughly agitated to prevent clumping of the beads. Then, reflectance spectra were collected using the MMS probe and the MMS instrument. The DRS spectra were calculated using the following expression:

$$DRS(\lambda) = \frac{Reflectance(\lambda) - Background(\lambda)}{(Spectralon(\lambda) - Background(\lambda))/(calibStd(\lambda))}, \tag{4.7}$$

where $Reflectance(\lambda)$ is the recorded reflectance spectrum from the phantom, $Background(\lambda)$ is the background spectrum collected from an opaque cup of deionized water, $Spectralon(\lambda)$ is the

reflectance spectrum recorded from a calibrated standard (20% reflectance standard, Labsphere Inc., North Sutton, NH), and $calibStd(\lambda)$ is the manufacturer-specified response of the standard. In this way, the DRS is expressed in calibrated reflectance units.

The probe-specific r_d and r_c values were calculated using a lookup table. First, a lookup table was generated, for each phantom, by numerically integrating Eq. (4.2) for a range of r_d and r_c values, while keeping the μ_s' and μ_a values fixed to the known values for that particular phantom. Then the measured DRS spectrum specified by Eq. (4.7) was compared to the spectra in the lookup table. The spectrum in the lookup table that is the best fit to the experimental DRS spectrum is associated with particular values of r_d and r_c. These best fit spectra are shown in Fig. 4-5. Figure 4-5 also shows the best fits to the experimental DRS spectra using Eq. (4.3) to calculate reflectance and optimizing over r_c' while keeping fixed the known μ_s' and μ_a values for each phantom.

We can now make several conclusions regarding the calibration of the MMS probe. Although the optimal values of r_d and r_c vary slightly across the five phantoms, one can verify that intermediate values (r_d = 0.45 mm and r_c = 0.30 mm) can model well all five phantoms. These average parameters also make physical sense given the MMS probe ball lens that specifies a both delivery spot and also a range of reflected angles that can couple into the collection fibers. On the other hand, we observe that the simplified Eq. (4.3) does not model the experimental data well for the MMS probe. Therefore, Eq. (4.2) should be used to model DRS spectra collected with the MMS probe.

As an addendum, we can make some observations relating to the FastEEM probe geometry. Using the FastEEM probe, DRS spectra were collected from the same five phantoms. The same calibration procedure was performed using both Eq. (4.2) and Eq. (4.3). The optimal r_d and r_c parameters for the FastEEM probe were in the range $r_d = 0.20$ mm and $r_c = 0.35$ mm, which makes

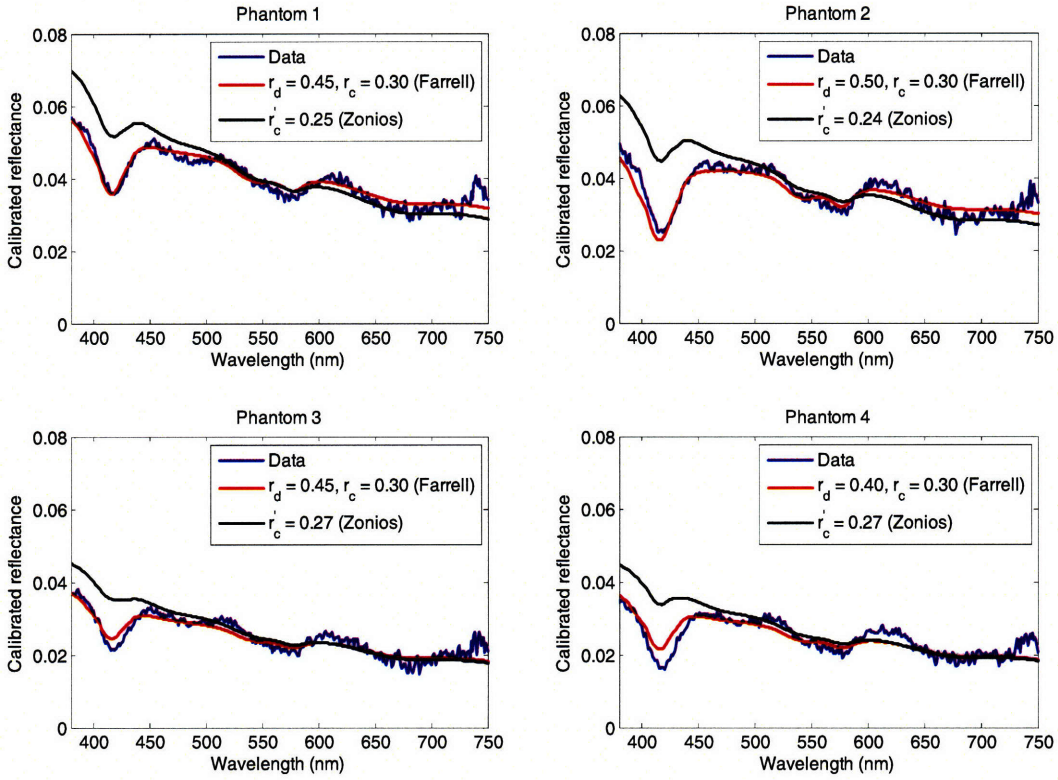

Figure 4-5. The experimental DRS spectra for phantoms 1-4 (blue), the best fits using a lookup table with Eq. (4.2) (red), and best fits using Eq. (4.3) (black).

physical sense given the FastEEM probe geometry. Moreover, Eq. (4.3) resulted in a much better fit (not shown) to experimental data for the FastEEM probe compared to the MMS probe, using $r_c^{'} = 0.34$ mm. This is consistent with the previously published work [66] and with observation that since $r_d = 0.20$ mm and $r_c = 0.35$ mm, the Eq. (4.3) assumption of point source delivery is sensible (since $r_d < r_c$). Whereas for the MMS probe one needs to use Eq. (4.2) and the calibrated r_d and r_c values, for the FastEEM probe it is sufficient to use Eq. (4.3) and the calibrated $r_c^{'}$ value.

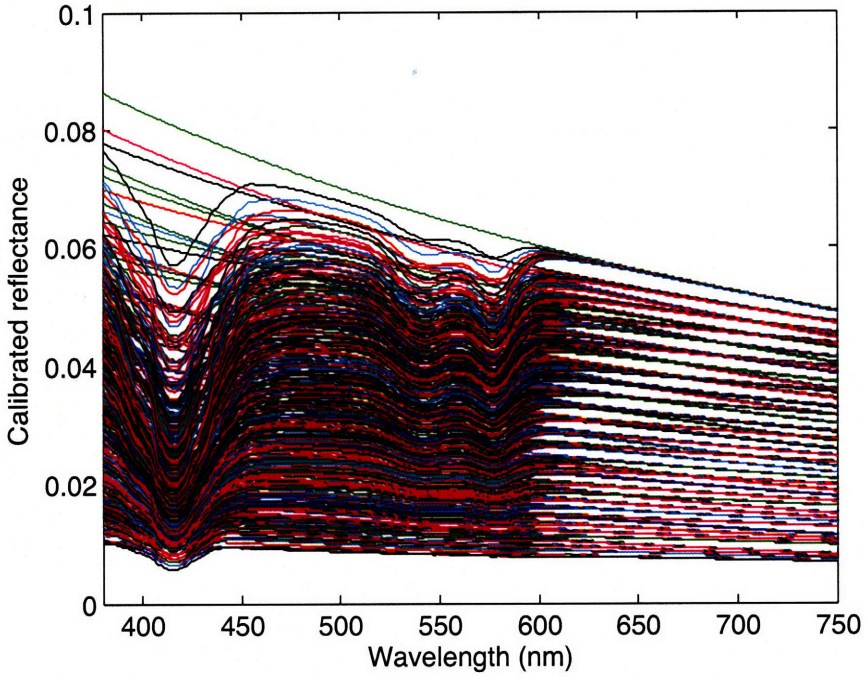

Figure 4-6. A prospective lookup table calculated using Eq. (4.2) for various values of μ_s' and μ_a while keeping $r_d = 0.45$ mm and $r_c = 0.30$ mm.

Prediction: extracting correct DRS modeling parameters

Once the calibrated values of r_d and r_c are known, the second part of the process described in Fig. 4-3 is to generate a method to prospectively extract μ_s' and μ_a from an unknown tissue sample. This is done by means of a lookup table in which DRS spectra are generated by numerically integrating Eq. (4.2) over a range of values of μ_s' and μ_a, while keeping the probe-specific parameters r_d and r_c fixed. Then, an unknown tissue spectrum is compared to the entries in the lookup table to obtain the optimal values of μ_s' and μ_a, corresponding to that entry. One such lookup table, calculated for $r_d = 0.45$ mm and $r_c = 0.30$ mm is presented in Fig. 4-6. To check its validity, the prediction table was applied to the phantom spectra and the extracted spectral parameters (A, B, cHb, and α) were compared to the known true parameters. The deviation between the two was on average

only a few percent which demonstrates the accuracy of the predictive fitting.

Note that a prediction lookup table is not necessary for the FastEEM probe because once the calibrated $r_c^{'}$ value is known, one may simply use the closed form Eq. (4.3) and perform an optimization that minimizes the difference between the data and a model-generated fit in order to extract the spectral parameters. In principle, the constrained minimization can be performed for MMS probes as well using Eq. (4.2) and numerical integration. However, this is computationally much more expensive, which is why the lookup table is desirable for real-time fitting applications.

■ 4.3.2 IFS modeling

This section describes the modeling needed to extract an IFS spectrum from a raw fluorescence spectrum and the associated probe calibration procedure.

Model for extracting IFS

Raw tissue fluorescence, in additional to containing the emission spectrum of fluorophores, is also distorted by absorption and scattering. Intrinsic fluorescence, on the other hand, is defined as the signal free from this interference and that is thus a linear function of the concentrations of the fluorophores. Zhang *et al.* [80] presented a method based on photon migration of extracting IFS spectra from turbid media, which built on a previously developed model of Wu *et al.* [79]. The IFS spectrum f_{xm} is related to the experimentally measured fluorescence spectrum F_{xm} and DRS spectrum R_m by means of the following expression [80]:

$$f_{xm}(\lambda) = \frac{F_{xm}}{\frac{1}{\mu_{sx}l}\left(\frac{R_{0x}R_{0m}}{\epsilon_x\epsilon_m}\right)^{1/2}\frac{R_x}{R_{0x}}\left(\frac{R_m}{R_{0m}}+\epsilon_m\right)}, \tag{4.8}$$

where R_x is the DRS spectrum evaluated at the fluorescence excitation wavelength, R_{0x} is similar to R_x but evaluated using Eq. (4.2) by setting $\mu_a = 0$, R_{0m} is similarly evaluated but for all needed fluorescence emission wavelengths, and μ_{sx} is evaluated at the fluorescence excitation wavelength and is extracted from $\mu_s^{'}$ using Eq. (4.4) and the known value of anisotropy (g). Finally, ϵ_x and ϵ_m are evaluated at the excitation and emission wavelengths using $\epsilon = e^{\beta} - 1$, where $\beta = S(1-g)$, for a fixed parameter S and anisotropy g, and l is related to the optical thickness of the sample.

Of all these parameters, S and l are probe-specific parameters that need to be calibrated for a particular probe. This is done in a similar fashion as described by Fig. 4-3 in the case of DRS. First, a set of known phantoms is used to calibrate the values of S and l. Then, these probe-specific parameters are held fixed for the particular probe and used with Eq. (4.8) for extracting IFS prospectively from unknown samples.

Phantom preparation

The phantoms used to calibrate the IFS parameters were the same five phantoms used for the DRS calibration, except that a small amount of furan 2 (Lambdachrome, Germany) was added to each sample to achieve a furan concentration of 0.9 μM.

Calibration: finding probe-specific S and l

The phantoms were remixed in small glass vials and again thoroughly agitated to prevent clumping of the beads. Then, reflectance and fluorescence spectra were collected using the MMS probe and the MMS instrument. The DRS spectra were extracted according to Eq. (4.7) to obtain R_m. The fluorescence spectra were corrected by subtraction of a fluorescence background spectrum, recorded from an opaque cup of deionized water, to obtain F_{xm}.

Phantom 5, which contained no absorption and hence no absorption-related artifacts, was used

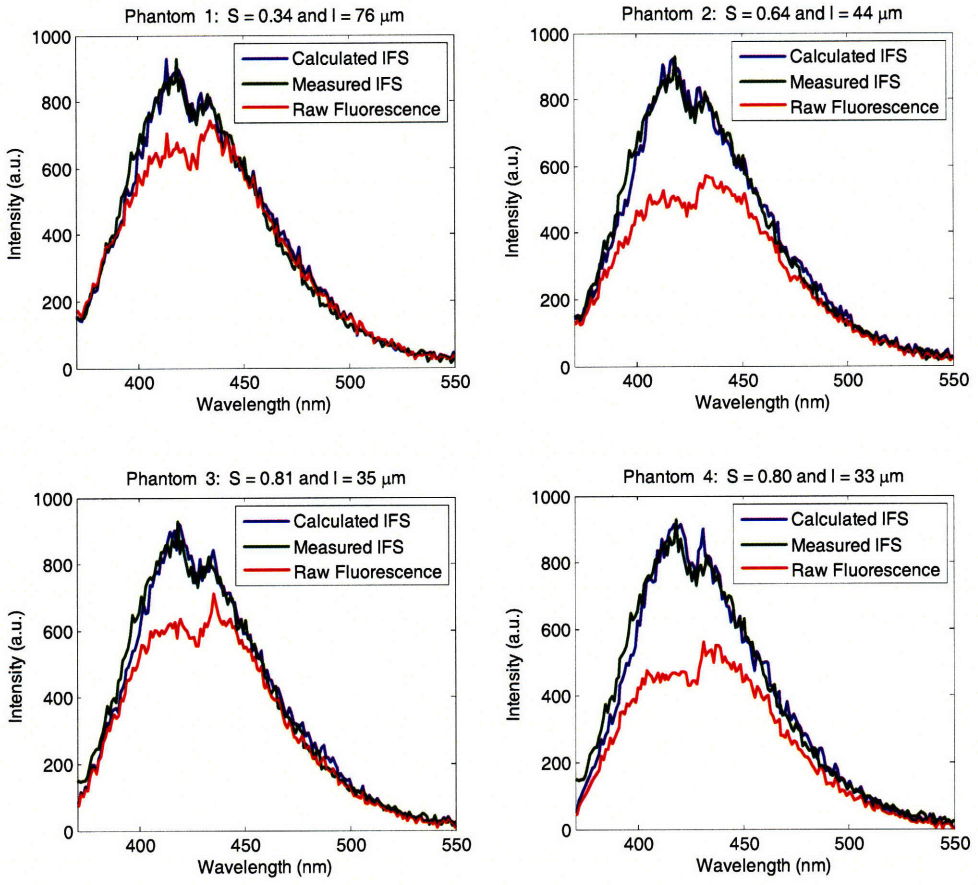

Figure 4-7. The optimal probe-specific parameters S and l, for each phantom, that resulted in the calculated IFS spectrum (using Eq. (4.8)) being closest to the measured IFS spectrum (phantom 5).

to model the IFS signal. Then, Eq. (4.8) was used to optimize over the parameters S and l until the optimal parameters were achieved for each of the phantoms 1-4. These optimal parameters resulted in the calculated IFS spectrum (Eq. (4.8)) being closest to the IFS spectrum (phantom 5) and they are presented in Fig. 4-7. The values of the parameters that minimize the combined error (calculated IFS - true IFS) for the four phantoms are $S = 0.7$ and $l = 40$ μm.

Prediction: extracting correct IFS spectrum

Having calibrated the IFS parameters, any prospective raw fluorescence spectra should be corrected using Eq. (4.8) to extract the IFS signal with the probe-specific parameters of $S = 0.7$ and $l = 40$ μm. Once the correct IFS spectrum is extracted, it can be fit using least squares to a specific linear model of constituent spectra.

■ 4.4 Summary

We have described and design and calibration of an integrated MMS probe, capable of efficiently collecting reflectance, fluorescence, and Raman signals from the same location in tissue. The probe is approximately 2 mm in outer diameter and contains a single excitation fiber and a ring of 15 collection fibers. Appropriate filters at the probe tip allow for efficient extraction of the relatively weak Raman signals, and the probe components are optimized to enable efficient transmission of light in the entire 300-1000 nm range. Since a probe with this excitation/collection geometry has not been used previously to collect reflectance and fluorescence spectra, careful tissue-mimicking phantoms are used to characterize the optical properties of the probe. These calibration steps provide probe-specific modeling parameters that enable the accurate extraction of spectral parameters.

■ 4.5 Acknowledgements

Chae-Ryon Kong contributed to the design of the phantom study experiments, phantom study data collection, and performed some of the analysis related to IFS. Zoya Volynskaya assisted with some of the experimental data collection.

Chapter 5

MMS instrumentation development

The clinical MMS instrument is a practical and modular merging of the designs of the previously developed clinical Raman and FastEEM systems. The MMS instrument contains all the critical functionality of both systems with several improvements based on newer technology.

It was believed previously that two IFS excitation wavelengths, 308 and 340 nm, were needed to detect a thin fibrous cap, as described in Sec. 2.4. As a result, the MMS instrument initially pursued a 308 nm UV lamp to provide the additional IFS excitation. The experiments and problems associated with the 308 nm UV lamp are summarized in Appendix C, which describes the reasons why this source was ultimately abandoned. In parallel, later analysis has indicated that a more appropriate parameter derived from a single excitation wavelength, 340 nm, provides a more robust way to detecting a thin fibrous cap, as described in Sec. 2.6. For these reasons, the MMS instrument in its present state contains a single excitation wavelength rather than multiple wavelengths characteristic of the FastEEM instrument. It remains to be seen whether other, longer, fluorescence excitation wavelengths that have been used in the past to study artery disease (e.g. 476 nm [71]), should also be included, at some point, as part of the MMS instrument.

5.1 Previous instrumentation

As mentioned previously, two separate instruments were used for Raman and DRS/IFS studies in the past. This section technically described both earlier systems, focusing on aspects in which they are different from the MMS instrument.

5.1.1 Clinical Raman system

Our laboratory has previously developed a compact clinical Raman instrument capable of real-time application [88]. The instrument uses an 830 nm diode laser to excite Raman scattering. The laser light is filtered and coupled into the Raman probe, which delivers to and collects light from tissue. The collected light is passed through a spectrograph and dispersed onto a CCD. The entire operation of the system is fully automated and controlled via computer, as shown in Fig. 5-1.

Instrumentation

Light from an 830 nm InGaAs diode laser (Process Instruments, Salt Lake City, UT) is collimated by a pair of cylindrical lenses and passed through a holographic bandpass filter centered at 830 nm (Kaiser Optical Systems Incorporated, Ann Arbor, MI). The light is then coupled into the 200 μm core diameter excitation fiber of the Raman probe using a 5x microscope objective (NA=0.1, Newport Corporation, Irvine, CA). Illumination of the sample is gated by a high-speed, 6 mm aperture, computer-controlled shutter (LS6ZM2, Vincent Associates, Rochester, NY). The excitation fiber is terminated with an FC connector to provide day-to-day reproducibility of alignment.

An optical fiber probe is used to transport the excitation and Raman scattered light to and from the tissue sample at the distal end of the catheter [87]. A more detailed description of the Raman probe is given in Sec. 4.1. For 100 mW of excitation power, the resultant irradiance is 318 W/cm^2,

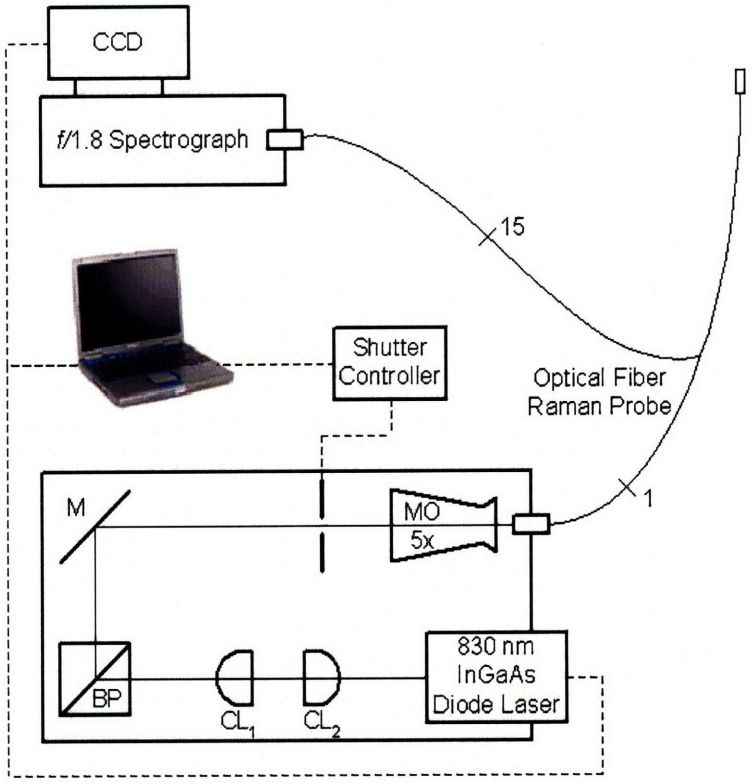

Figure 5-1. Schematic diagram of the clinical Raman system (CL: Cylindrical Lens; BP: 830 nm Band-Pass filter; M: Mirror; MO: Microscope Objective; CCD: Charge-Coupled Device detector).

which has been clearly shown to not cause any tissue damage [148]. The proximal end of the probe contains the collection fibers that are arranged in a vertical array and serve as the entrance slit to the spectrograph (Holospec f/1.8i, Kaiser Optical Systems), attached by means of a modified BNC connector. The collected Raman light is dispersed onto a back-illuminated, deep-depletion CCD detector with a 1340×400 array of pixels (Spec-10:400BR, Princeton Instruments, Trenton, NJ). The CCD detector has a 16 bit dynamic range and was liquid nitrogen cooled to -110°C. Spectra are obtained by vertically binning the signal from the collection fibers.

Real-time software

The system utilizes LabVIEW software (v 6.1, National Instruments, Austin, TX) as the primary platform to interface with various hardware components of the system and control data flow, allowing automation of more complicated calibration and analysis routines. These subroutines are accomplished via a direct interface with Matlab (v.6.5.0, The Mathworks, Natick, MA) to provide relevant diagnostic parameters, such as calcification and total cholesterol in the case of atherosclerosis, or collagen and fat in the case of breast cancer [86, 126]. The modular design of the real-time software allows for easy adaptation of the instrument for different applications.

■ 5.1.2 FastEEM system

Our laboratory has previously developed a portable clinical instrument to collect fluorescence and reflectance spectra called the FastEEM, for fast excitation-emission matrix (EEM) [109, 110, 111]. A fluorescence EEM is produced by means of a rotating wheel containing laser dyes, pumped by a 308 nm XeCl excimer laser, which generates nine laser pulses at excitation wavelengths ranging from 340 to 500 nm which, including the 308 nm pulses, provides ten laser excitation wavelengths in all. In addition, a Xenon flash lamp produces white light pulses for reflectance. This light is delivered to and collected from the tissue via an unfiltered flexible optical fiber probe. Return light from the tissue is transmitted by the collection fibers to a spectrograph/CCD detector for analysis. This schematic of this instrument is shown in Fig. 5-2.

Instrumentation

The FastEEM utilizes an optical fiber probe to deliver a sequence of ten laser pulses (308-480 nm) and two white light pulses to the tissue sample. The collected white light reflectance and

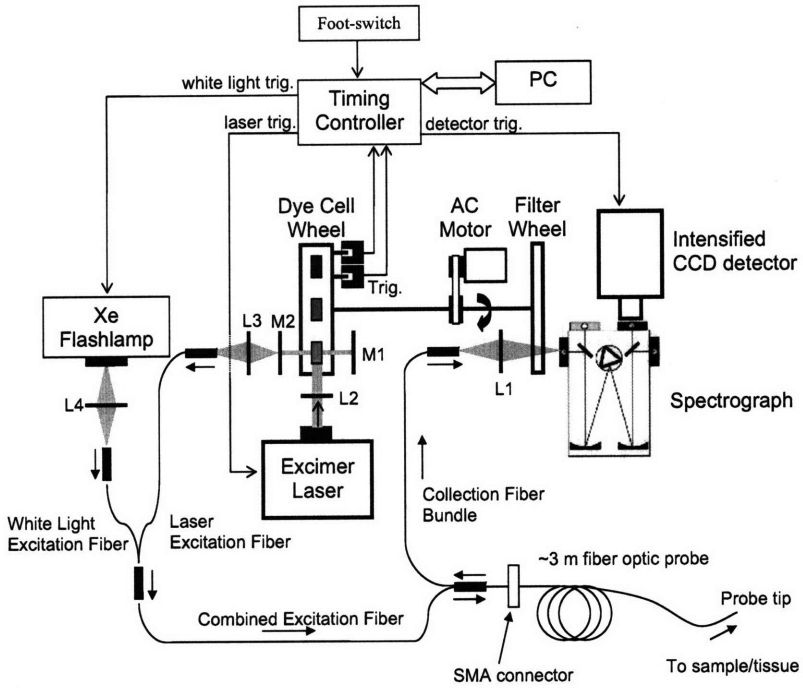

Figure 5-2. Schematic diagram of the FastEEM clinical spectrophotometer. L1, L2, L3, L4 are lenses. M1 and M2 are mirrors. (Published with permission from: Instrumentation for multi-modal spectroscopic diagnosis of epithelial dysplasia, *Technology in Cancer Research & Treatment*, Volume 2, page 509, 2003, Adenine Press; http://www.tcrt.org)

fluorescence return via the same probe and are brought to the entrance slit of the diffraction grating spectrometer (Spectra Pro 150, Acton Research, Acton, MA), connected to an intensified CCD detector (PIMAX, Roper Scientific, Princeton, NJ). The total collection time for all ten fluorescence emission spectra and the two reflectance spectra is approximately 0.3 s. Several of these acquisitions can be averaged together to increase the SNR, making a typical acquisition time on the order of 1.5 s.

The instrument generates the excitation wavelengths between 342-480 nm by means of dye lasers, while the 308 nm excitation comes directly from the XeCl excimer laser (8 ns pulse FWHM, Optex XeCl, Lambda Physik, Ft. Lauderdale, FL). A Xe flashlamp (L7684, 1J @ 2.9 μs pulse

FWHM, Hamamatsu Corp., Bridgewater, NJ) is used to generate the two white light spectra. By using set of rapidly rotating wheels, driven by an AC motor at just over 3 Hz (180 RPM), the FastEEM achieves its relatively short acquisition time. This "dye cell wheel" contains nine dye cells with different dye solutions (for the 342-480 nm fluorescence excitation), one prism (for 308 nm excitation), and two open spaces (for the white light). The dye cells are 2.8 ml spectrosil quartz cuvettes (Starna Cells, Atascadero, CA) with a 10 mm pathlength and transmission from 170-2700 nm and contain a mixture of the dyes (p-Terpenyl, PBD, Exalite 384, Exalite 398, LD 425, Stilbene 420, Coumarin 440, Coumarin 460, Coumarin 480) and a solvent (either p-dioxane or methanol). The XeCl excimer laser pumps each dye cell as it traverses the common optical resonant cavity (mirrors M1 and M2). The output pulses are coupled into a fiber after passing through a 10% reflective mirror (M2) and lens (L3). In addition, the 308 nm excimer laser light is coupled to the same fiber by the prism traversing the optical cavity. Lastly, when the two open spaces in the wheel traverse the optical cavity, the Xe flashlamp is triggered instead of the excimer laser and the light is coupled into a separate fiber. The two fibers, carrying either the laser excitation or the white light, are combined into one by a fiber splitter and guided to the optical fiber probe. As the collected light returns through the collection fibers of the probe, it passes through another synchronized "filter wheel," containing long pass filters that remove the excitation line, and is focused onto the entrance slit of the spectrograph.

Since the Xe lamp emits significant intensity in the range 270-800 nm and the spectrograph operates in the first order of diffraction (i.e. the longest wavelength it can collect is twice the shortest wavelength), this provides a range of 270-540 nm. However, light in the second order of diffraction can enter the spectrograph above 540 nm and thus cause an artifact. To correct for this effect, a second reflectance spectrum is collected using a long pass filter (420 nm) to remove

the short wavelengths and the amplitude of its spectral response is adjusted in software to match that of the unfiltered response in the region between 460 and 530 nm. This correction enables one continuous spectrum from 300-800 nm to be created from the merging (at 500 nm) of these two white light spectra.

The FastEEM relies on a timer controller, consisting of a control logic circuit and a National Instruments timer/counter board (PCI-6602, National Instruments, Austin, TX), to program the timing of the data collection. Optical interrupters (Omron Photomicrosensors EE-SX770, Schaumburg, IL) mounted on the rotating wheel are used to generate trigger signals, which are used to determine when to pulse the laser or white light source and when to gate and read data from the detector.

Real-time software

Custom software developed in the graphical programming environment LabVIEW 7.0 (National Instruments, Austin, TX) is used to control and operate the FastEEM. In addition, the control software handles all data calibration and enables real-time data acquisition, providing an immediate check on data quality. A spectrum from a mercury lamp is used to calibrate the wavelength. A background calibration spectrum is used to correct for effects of CCD dark currents and stray light. Since the intensity of each dye laser is inherently different from one another, the intensity of each EEM is calibrated by measurement of a standard rhodamine B dye mixture (5 g/L, ethyleneglycol) with a known quantum yield. Lastly, a spectrum collected from a reflectance standard (20% reflectance standard, Labsphere Inc., North Sutton, NH) is used to calibrate the tissue reflectance measurements.

■ 5.2 MMS integrated instrumentation

This section describes the MMS instrument. Many of the instrumentation and software aspects of the system are either equal to or improvements upon the previously described instrumentation. The schematic of the MMS instrument is given in Fig. 5-3.

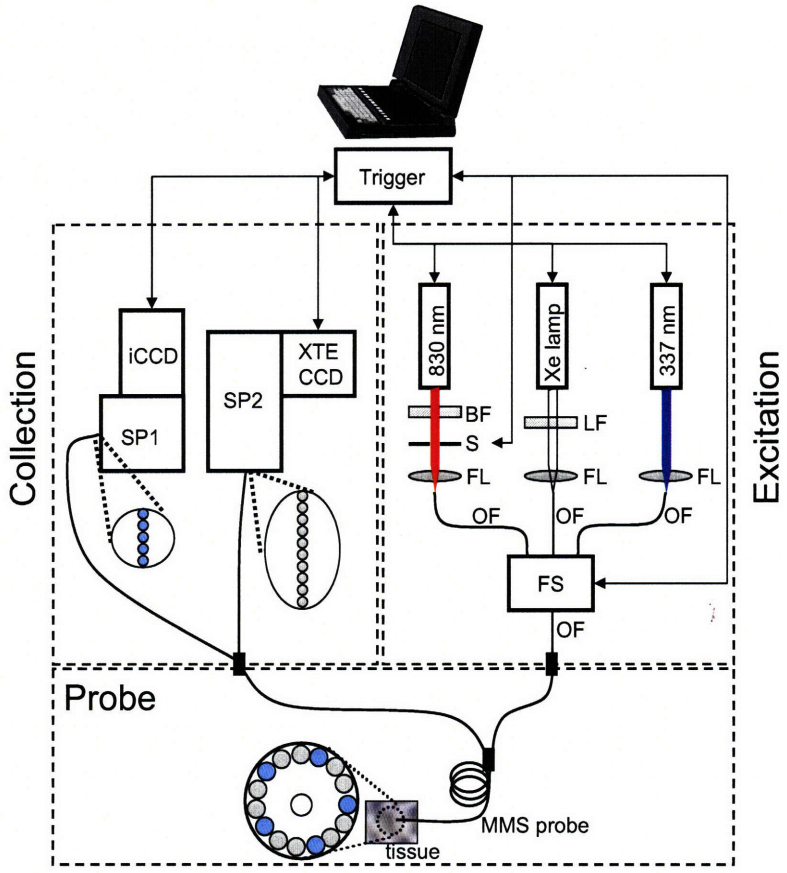

Figure 5-3. Schematic diagram of the MMS instrument. BF = bandpass filter, LF = longpass filter, S = shutter, FL = focusing lens, OF = optical fiber, FS = fiber switch, SP1 = visible spectrograph, SP2 = NIR spectrograph, iCCD = intensified charge-coupled device, XTE CCD = thermoelectrically cooled charge-coupled device.

5.2.1 Sources

The MMS instrument contains three excitation sources: a Xe flash lamp (L7684, Hamamatsu Corp., Bridgewater, NJ), a 337 nm N_2 laser (NL100, Stanford Research Systems, Sunnyvale, CA), and an 830 nm diode laser (Process Instruments, Salt Lake City, UT). All are configured to be triggerable externally through the automated software platform. The Xe lamp provides a 2.9 μs FWHM pulse of white light, 1 J/pulse max, given an external trigger supplied by the software. The light from the Xe lamp is passed through a ~370 nm longpass filter (LP02-364RS-25, Semrock, Rochester, NY) before being focused into a fiber; the purpose of this filter is to guarantee a collected range of reflectance 370-740nm that is free of 2^{nd} order diffraction effects from the spectrograph grating. The N_2 laser provides a 3.5 ns FWHM pulse of 337 nm light, 170 μJ per pulse, given an external trigger, and is focused into an optical fiber by a UV-coated lens. The diode laser can be configured to output a range up to 500 mW of continuous-wave 830 nm light, driven by a user-specified analog signal. The 830 nm laser light is filtered by an 830 nm bandpass filter (LL01-830-12.5, Semrock, Rochester, NY) and gated by a mechanical shutter (LS6ZM2, Vincent Associates, Rochester, NY) before being focused into an optical fiber.

5.2.2 Coupling to probe

The excitation sources are coupled sequentially to the MMS probe using an optical fiber switch (FSM14, Piezo Jena, Germany). This is a MEMS device that provides superior coupling of the individual sources and interfaces simply with the control software by means of a binary code that is user-configurable. We had previously investigated a design using a linear translation stage and a concave mirror, which also gave promising results, but the fiber switch was chosen ultimately owing to its better performance and alignment-free coupling consistency. The fiber switch contains a four

input fibers and a single output fiber, all terminated by SMA connectors. The outputs of the Xe lamp, N_2 laser, and diode laser are directly channeled into the three individual input fibers of the fiber switch. The fourth remaining input of the fiber switch is left vacant for a potential future light source. The MMS probe is connected to the output fiber of the switch by means of an SMA-to-SMA connector. The overall transmission efficiency of the fiber switch is ~60%, broken down into an ~80% switching efficiency and an ~80% SMA-to-SMA coupling efficiency. By contrast, the earlier translation stage and concave mirror configuration had an overall efficiency of 40%.

■ 5.2.3 Detection

The MMS system uses two separate spectrograph/CCD modules: one optimized for NIR detection (Raman) and the other for visible wavelengths (reflectance and fluorescence). The operation of both cameras is controlled by modular LabVIEW drivers (R^3 Software, Princeton, NJ).

The 10 collection fibers carrying the Raman light are aligned in a linear array, effectively serving as an entrance slit to the spectrograph (Holospec f/1.8i, Kaiser Optical Systems), resulting in a ~9 cm^{-1} spectral resolution. The fibers are encased in a modified male FC connector to ensure highly reproducible alignment with the connector plate of the spectrograph. Any spectral changes incurred by disconnecting and reconnecting the linear array are below the system's spectral resolution. The numerical aperture of the collection fibers is f/#-matched to the spectrograph to conserve throughput. The spectrograph contains an 830 nm notch filter that further suppresses the elastically scattered Rayleigh light and a holographic grating to disperse the Raman scattered light onto a back-illuminated, deep-depletion CCD detector with a 1340×400 array of pixels (Spec10 XTE, Princeton Instruments/Acton, Acton, MA). The CCD detector has a 16 bit dynamic range and can be thermoelectrically cooled, within minutes, down to -90°C, a significant practical improvement

over the older Raman system. Spectra are obtained by vertically binning the signal from the ten collection fibers. The continuous-wave collection of the Raman signals mandates that the all the spectra be collected with the room lights turned off.

The five collection fibers carrying the reflectance or fluorescence light are arranged into a vertical slit to a diffraction grating spectrometer (Spectra Pro 150, Princeton Instruments/Acton, Acton, MA), resulting in a ~6 nm spectral resolution. The collection fibers have individual male SMA adapters that connect to corresponding female SMA adapters mounted to a plate adjacent to the spectrograph; this insures easy reproducibility as the probe is repeatedly connected to the system. The collected light is then dispersed onto an intensified CCD detector (PIMAX, Princeton Instruments/Acton, Acton, MA). The CCD is operated in a gated mode, where the intensifier is biased on for only the short period of time (~30 μs) immediately prior to and after each laser/white light pulse. The short duration of this gate ensures that the background from ambient light is negligible, though this is less of a concern on the MMS instrument since room lights are routinely turned off, as constrained by the Raman signal collection. Spectra are obtained by vertically binning the signal from the five collection fibers. The PIMAX camera has a 16 bit dynamic range and is thermoelectrically cooled to -20°C.

■ 5.2.4 Real-time software

The entire MMS system is controlled by a single user-friendly interface developed in LabVIEW (National Instruments, Austin, TX). The control flow of the software for a single MMS acquisition is presented in Fig. 5-4, describing the timing by which the various sources and detectors are triggered to collect the MMS spectra. The software platform allows for calibration spectra to be taken and stored, provides easy operation of the experimental data collection and storage,

and provides instant feedback about the collected spectra, fits, and extracted diagnostic spectral parameters. The triggering of the sources and cameras is done by two data acquisition (DAQ) cards (6062 and 6035E, National Instruments, Austin, TX).

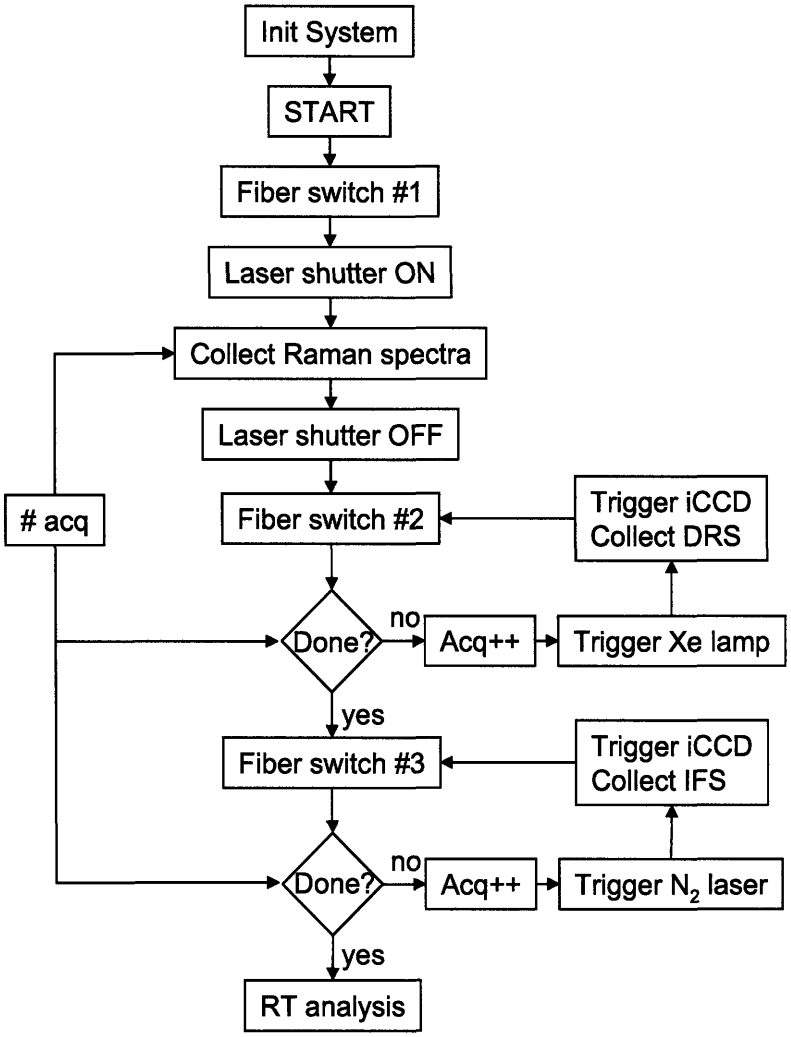

Figure 5-4. Control flow of the MMS instrument software.

■ 5.2.5 System calibration

In order to provide real-time data analysis and diagnosis, spectra for calibration and background subtraction must be acquired prior to data collection.

The material used to calibrate the Raman shift axis is 4-acetamidophenol (Tylenol). The remaining Raman fiber background signal from the optical fiber probe is characterized by acquisition of a spectrum from roughened aluminum. The spectral response of the Raman collection system is obtained by recording the spectrum of a calibrated tungsten white-light source, diffusely scattered by a reflectance standard ($BaSO_4$).

The wavelength of the reflectance and fluorescence spectra is calibrated by recording a spectrum from a mercury lamp. Background calibration for reflectance and fluorescence is used to remove effects of CCD dark currents and stray light and is typically acquired by collecting a spectrum from a opaque cup of deionized water. The reflectance amplitude is calibrated by collecting a spectrum from a reflectance standard (20% reflectance standard, Labsphere Inc., North Sutton, NH). Since EEMs are not collected, there is no need to routinely calibrate the fluorescence amplitude with rhodamine; instead, the stable output from the nitrogen laser is noted with an energy meter.

The system has been designed so that it is stable from day to day, thus disconnecting and reconnecting the probe to the system does not change the calibration parameters. However, different probes can have significantly different calibration parameters.

■ 5.2.6 Data analysis

In this section, the data analysis steps for each modality are briefly described.

Raman

A sequence of steps is executed before a quantitative Raman information is extracted from the raw spectrum acquired on the CCD. First, the data is corrected for the system spectral response by dividing it by the white light spectrum. The resultant data is then normalized to maximum peak height and truncated to the biological Raman region of interest appropriate to the models used in this study (686 to 1788 cm^{-1}). The next step is to remove the fiber background from the tissue data by subtracting the spectrum acquired from roughened aluminum. The relationship between the intensity of spectra from the aluminum and the tissue spectrum is dependent upon the tissue's optical properties, which are unknown *a priori*. Therefore, we iteratively subtract the same aluminum spectrum scaled by a range of different intensities to determine the optimal ratio for background removal. The spectrum that results in the lowest standard deviation of the residual between the data and the model fit is used for analysis. After fiber background removal, the remaining broadband tissue luminescence is removed by subtracting a 6^{th} order polynomial that is fit to the data [87]. This final correction step results in extraction of the Raman spectrum of the examination site. The resultant spectrum is calibrated to a standard set of wavenumber bins. This spectrum is analyzed with the appropriate disease model, atherosclerosis [85] or breast cancer [100], by using ordinary least squares, which provides the relative fit coefficients of the various chemical/morphological components of tissue. The user can toggle between the two different models as mandated by the clinical situation.

Reflectance and fluorescence

Similarly, a sequence of steps is executed to extract information from reflectance and fluorescence. The DRS spectrum is obtained from the raw reflectance spectrum by subtracting the background

spectrum and dividing by the background-subtracted reflectance standard response, whose true response is specified by the manufacturer. This calibration insures that the exictation/collection geometry of the probe is properly accounted for. The DRS spectrum is fit to the model of Farrell *et al.* [67] or Zonios *et al.* [66], depending on the probe that is used with the system, enabling the extraction of DRS spectral parameters (see Sec. 4.3.1). The IFS spectrum is obtained from the raw fluorescence spectrum by subtracting the background spectrum and applying the IFS extraction formula from Zhang *et al.* [80], enabling the extraction of IFS spectral parameters (see Sec. 4.3.2).

■ 5.2.7 Safety

The clinical MMS system must adhere to strict safety guidelines in the clinical environment. Any part of the system that touches the patient directly or indirectly must be kept sterile. Sterilization of the MMS probe was performed using cold-gas ethylene oxide. Furthermore, the excitation laser power cannot exceed a predetermined threshold value, which is determined and safeguarded before entering the operating room. As a precaution for safety of the operators and patient, the continuous-wave diode laser beam is gated by a high-speed shutter, also controlled by LabVIEW. The shutter opens automatically just before data acquisition begins and closes immediately after the acquisition is complete. The shutter then remains closed until the system receives a signal through LabVIEW for the next acquisition. The Xe flash lamp and the nitrogen laser are pulsed sources and thus internally shuttered.

■ 5.2.8 Clinical layout

In order for the MMS instrument to be a clinically used instrument, it needs to have a suitable, portable layout. The various components of the system described in Fig. 5-3, were optimally placed on optical breadboards with the help of SolidWorks software. This modular placement allowed for

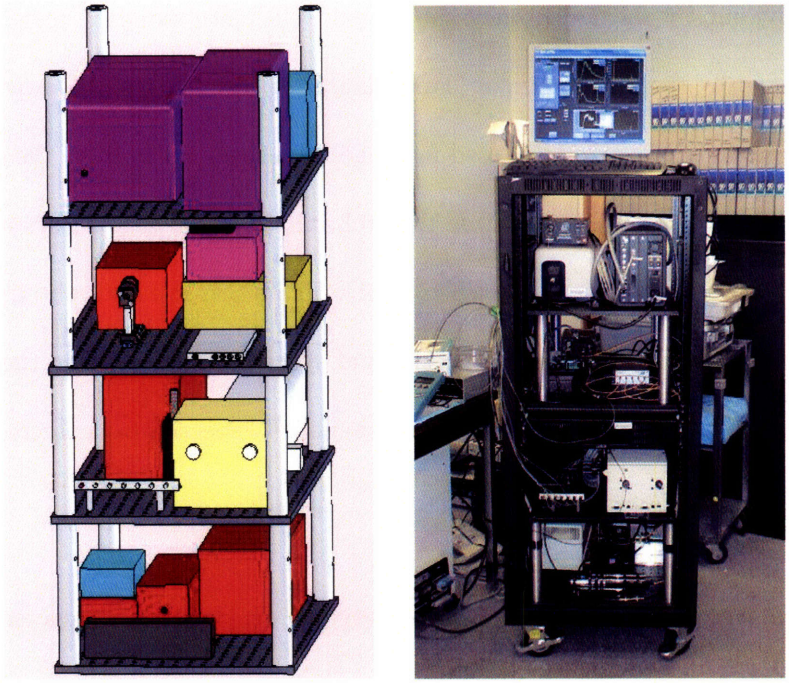

Figure 5-5. The layout of the MMS instrument (left) and a photo of the actual system (right).

the construction of the instrument within bounds of a metal enclosure (dimensions 27"x27"x58"), that can be wheeled into the operating room for clinical data collection. The layout schematic and a photo of the finished instrument are given in Fig. 5-5.

■ 5.3 Summary

We have developed an integrated instrument to be used with the MMS probe for the collection of reflectance, fluorescence, and Raman signals. The MMS instrument is designed to be compact and portable, thus ideally suited for clinical applications. All the critical diagnostic functionality of previous stand-alone Raman and FastEEM instruments has been preserved, taking advantage of technological improvements to reduce the size and cost of the system. The MMS instrument is easy to use, backwards compatible with previously developed probes for Raman and

reflectance/fluorescence, contains a software platform that automates instrument calibration and data collection, and provides real-time analysis capability.

■ 5.4 Acknowledgements

Zoya Volynskaya contributed to the development of the clinical MMS instrument. Jonathan Nazemi constructed a miniFastEEM system that served as a basis for the reflectance and fluorescence components of the MMS system. Luis Galindo was instrumental in overseeing and providing guidance in the overall instrumentation development. Figure 5-1 and text were reproduced from the *Journal of Biomedical Optics* [88] with permission from SPIE. Figure 5-2 and text were reproduced from *Technology in Cancer Research & Treatment* [111] with permission from Adenine Press. This research was conducted at the MIT Laser Biomedical Research Center under NIH Grant No. P41-RR-02594.

Chapter 6

Clinical implementation of MMS

This chapter describes the *in vivo* and *ex vivo* studies using MMS that were conducted at MetroWest Medical Center in Natick, MA.

6.1 Introduction

Numerous clinical studies have been undertaken by multiple research groups with the goal of characterizing the arterial wall. The techniques utilized include optical coherence tomography [51], fluorescence spectroscopy [78], near-infrared spectroscopy [59], etc. With the development of the Raman probe [87] and clinical Raman instrument [88], our group was the first to demonstrate, several years ago, the diagnostic application of Raman spectroscopy *in vivo* [89]. The present study is, to our knowledge, the first to date demonstration of collecting all MMS modalities - DRS, IFS, and Raman - in rapid succession, in a clinically acceptable time, in human patients *in situ*. The study was approved by the MetroWest Medical Center Institutional Review Board and the MIT Committee of the Use of Humans as Experimental Subjects. A total of 12 patients participated in the study.

6.2 Methods

Spectroscopic analysis of human artery tissue with MMS was performed both *in vivo* and *ex vivo*. Detailed histological analysis from the tissue locations was used to corroborate the spectroscopic findings. Based on the results, a diagnostic algorithm for detecting vulnerable plaques was developed.

6.2.1 *In vivo* spectral collection

MMS data was collected *in vivo* during two kinds of peripheral vascular procedures: femoral bypass and carotid endarterectomy surgeries. During a femoral bypass, a stenosed or occluded portion of one of the arteries in the lower limbs, usually femoral, is circumvented (or bypassed) with the attachment of a (synthetic) graft that restores adequate blood flow beyond the blocked portion of the vessel. During a carotid endarterectomy, a severely stenosed portion of the carotid artery, typically near a bifurcation, is treated by direct removal of the plaque, after which the artery wall is restored with a synthetic patch.

During a particular surgery, the MMS instrument was wheeled into the operating room shortly after the start of the surgery and placed within a few feet of the patient, just outside of the sterile field. The MMS probe, which had been previously sterilized overnight by either cold gas etylene oxide or Sterrad®, was connected to the MMS instrument, while keeping the proximal end in the sterile field. The instrument was turned on and software activated for data acquisition. Calibration spectra from the most recent procedure were loaded to enable real-time display of the acquired spectra and the ensuing data analysis. Spectra collected *in vivo* typically consisted of a 2.5 second 830 nm exposure for Raman (typically 10 consecutive exposures of 0.25 seconds each), ~1 second flashlamp exposure for DRS (typically 5-7 pulses of light), and ~1 second N_2 laser exposure for

IFS (typically 5-7 pulses of light), resulting in a total exposure time per tissue site of less than 5 seconds. The excitation powers for the three modalities were typically: 100 mW of the 830 nm diode laser for Raman, ~2 μJ/pulse of flashlamp measured at 575 nm for DRS, and ~4 μJ/pulse of the N_2 laser measured at 337 nm for IFS. The operating room and surgical lights were turned off during spectra data collection.

During a femoral bypass surgery, the surgeon would insert the front-viewing MMS probe through the proximal anastomosis site to make direct contact with the posterior wall of the saline-flushed artery. Spectra were also collected adjacent to the incision on the intimal side of the artery, where the graft would later be attached. The probe was always held perpendicular to the artery wall. A small biopsy was taken from the spectrally examined location and kept in saline until later use *ex vivo*. As the graft was typically attached to healthy portions of the artery, these specimens tended to be non-atherosclerotic, thus serving as controls. Note that biopsies could only be taken from the location adjacent to the incision but not from the posterior artery wall.

During a carotid endarterectomy surgery, the diseased portion of the artery was clamped off on both sides (with a shunt inserted to maintain blood flow to that half of the brain) and incised along the artery to expose the occlusive plaque. Spectra were collected from the intimal surface of the saline-flushed plaque with the probe normal to the artery wall (Fig. 6-1). The plaque was then surgically removed and kept in saline until later use *ex vivo*. These specimens tended to be heavily diseased plaques, with calcifications and thrombi, thus serving as potential candidates for vulnerable plaques.

Owing to surgical procedure constraints, not every artery that was spectrally evaluated *in vivo* resulted in an excised specimen that could also be evaluated *ex vivo*(particularly true for femoral bypasses). Conversely, *in vivo* data collection was not possible in every surgery that ended up

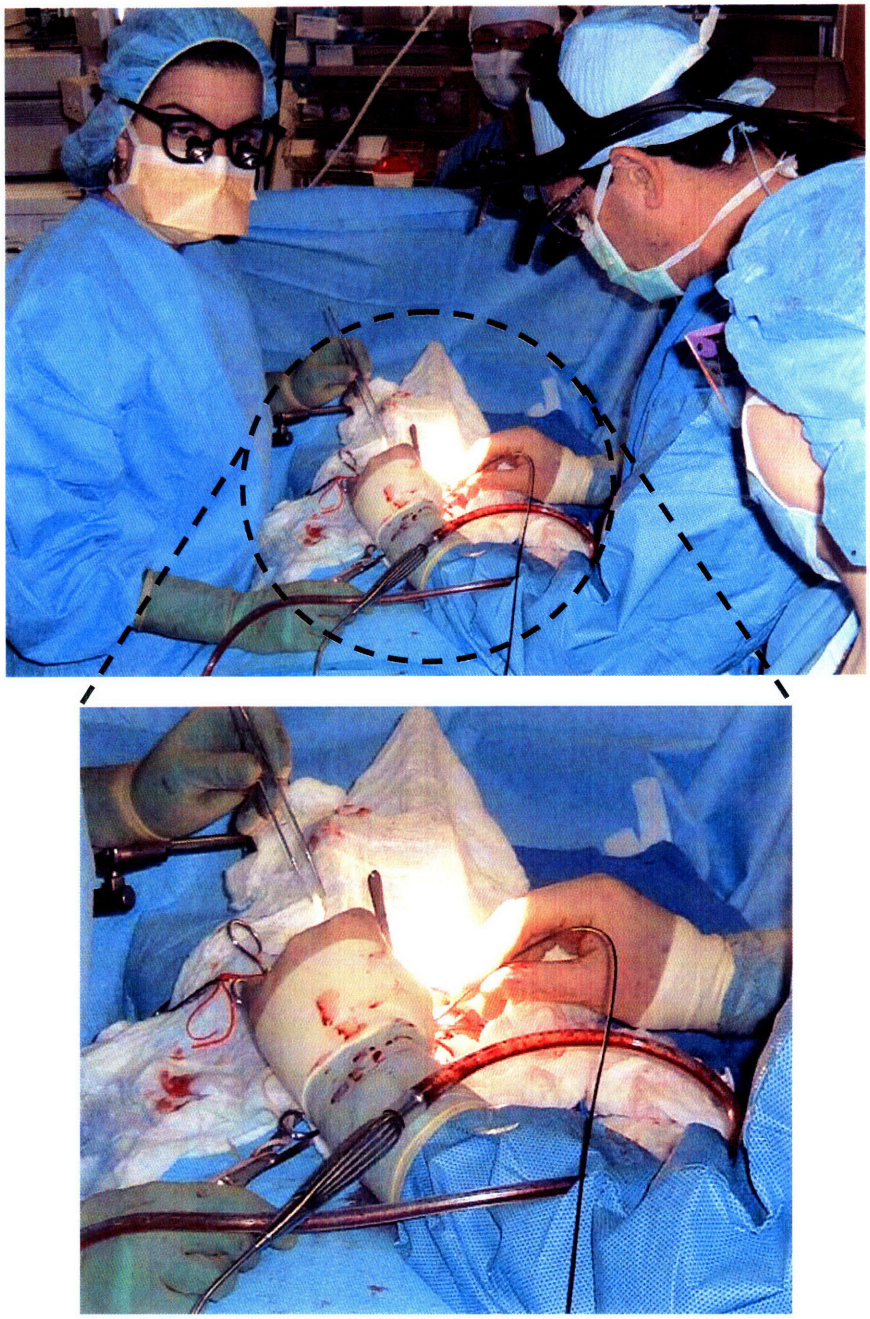

Figure 6-1. *In vivo* data collection during a carotid endarterectomy surgery. The surgeon is holding the sterilized MMS probe in contact with the exposed carotid artery plaque, moments before data acquisition.

yielding an excised specimen to be evaluated *ex vivo*. In total, we have collected MMS spectra from 40 locations *in vivo* from 9 patients.

■ 6.2.2 *Ex vivo* spectral collection

The *ex vivo* studies were performed on the excised artery specimens from the aforementioned surgeries in a research lab wing of the hospital. This data collection was typically done within one hour after the excision of the specimens. Calibration spectra were obtained prior to spectral data collection: a spectrum of 4-acetamidophenol for Raman wavenumber calibration, a spectrum from an aluminum surface for Raman probe background, a spectrum of a white light scattered off $BaSO_4$ for Raman spectral correction, a spectrum from a Hg lamp for DRS/IFS wavelength calibration, a spectrum from a 20% Spectralon reflectance standard for DRS intensity calibration, and a spectrum from deionized water in an opaque cup for DRS and IFS background characterization.

Spectra were collected *ex vivo* from multiple locations on the excised specimen, covering those areas that were spectrally examined *in vivo* as well as other locations not examined *in vivo* owing to lack of time during surgery. The probe was held normal to the artery and stabilized with a holding clamp. The room lights were again turned off during the data acquisition. The *ex vivo* acquisition was typically done with 5 seconds for Raman (20 exposures of 0.25 seconds), ~1.5 seconds for DRS (10 pulses of light), and ~1.5 seconds for IFS (10 pulses of light). The excitation powers for the three modalities were approximately the same as those used *in vivo*. The excitation energy of the N_2 laser on the tissue (μJ/pulse) measured each day was recorded so that the IFS spectra could be appropriately normalized later.

Following spectral acquisition, the evaluation site was demarcated with colloidal ink (Fig. 6-2), the specimen was fixed in formalin, and submitted for histological analysis. In total, we have

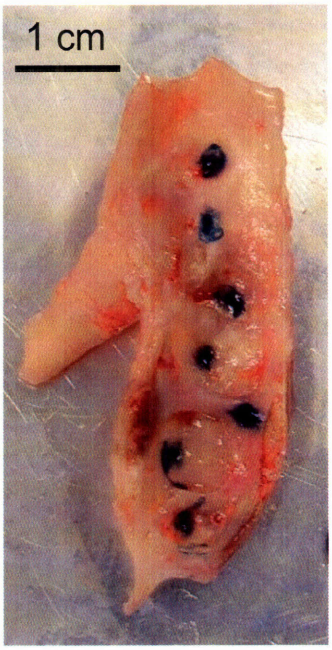

Figure 6-2. An excised carotid artery plaque with ink dots demarcating spectral evaluation sites.

collected MMS data from 84 locations *ex vivo* from 11 patients.

■ 6.2.3 MMS data analysis

The MMS spectra were processed and analyzed according to procedures described in previous chapters.

The DRS spectra were extracted after removing the background from raw reflectance and dividing by the response of the Spectralon reflectance standard with calibrated reflectivity ($calibStd(\lambda)$), as given below:

$$DRS(\lambda) = \frac{Reflectance(\lambda) - Background(\lambda)}{(Spectralon(\lambda) - Background(\lambda))/(calibStd(\lambda))}. \tag{6.1}$$

The calibrated DRS spectra were fit with the Farrell model, Eq. (4.2), and using the calibrated

probe-specific parameters ($r_d = 0.45$ mm and $r_c = 0.30$ mm) as described in Sec. 4.3.1. In applying the Farrell model, the $\mu_s^{'}$ and μ_a coefficients were modeled as:

$$\mu_s^{'}(\lambda) = A \cdot \left(\frac{\lambda}{\lambda_0}\right)^{-B} \tag{6.2}$$

$$\mu_a(\lambda) = (log_e 10)\left\{C_{diff} \cdot v \cdot (\alpha \cdot \epsilon_{HbO_2}(\lambda) + (1-\alpha) \cdot \epsilon_{Hb}(\lambda)) + c_{\beta-car} \cdot \epsilon_{\beta-car}(\lambda)\right\}, \tag{6.3}$$

where $\lambda_0 = 1$ μm, ϵ_{HbO_2}, ϵ_{Hb}, and $\epsilon_{\beta-car}$ are the extinction coefficients of oxy-hemoglobin, deoxy-hemoglobin and β-carotene, respectively, and α is the hemoglobin saturation parameter. The parameter v is the blood volume fraction, $v = c_{Hb}/(150$ mg/ml), and the parameter C_{diff} accounts for the inhomogeneous distribution of hemoglobin in blood vessels [149], and is defined as:

$$C_{diff}(\lambda, R_{vess}) = \frac{1 - exp\{-2 \cdot \mu_{a,bl}(\lambda) \cdot R_{vess}\}}{2 \cdot \mu_{a,bl}(\lambda) \cdot R_{vess}}, \tag{6.4}$$

where $\mu_{a,bl}(\lambda)$ is the absorption coefficient of whole blood (at concentration 150 mg/ml) and R_{vess} is the effective radius of the hemoglobin-containing vessels found in tissue.

The extinction coefficients of the said tissue absorbers at unit concentrations are presented in Fig. 6-5a. The experimental data was fit to the model of Farrell *et al.* using a standard optimization method that minimized the difference (Eq. (3.13)), in the χ^2 sense (Eq. (3.11)), between the DRS data (Eq. (6.1)) and fit (Eq. (4.2)) in the range from 370 - 740 nm. The fits resulted in an estimate of the $\mu_s^{'}$ and μ_a values of the tissue, which are characterized by parameters A, B, c_{Hb}, α, $c_{\beta-car}$, and R_{vess}.

The IFS spectra were extracted by subtracting the background from raw fluorescence and applying the IFS correction procedure of Zhang, Eq. (4.8), and using the calibrated probe-specific

parameters ($S = 0.7$ and $l = 40$ μm) as described in Sec. 4.3.2. Then, as done previously [131], the IFS spectra were used to develop an IFS model using multivariate curve resolution (MCR). The spectral features of the IFS signals could be well characterized using two MCR components, one collagen-like and another elastin/lipid-like, both shown in Fig. 6-5c. The IFS spectra were fit using these two MCR components, in the range 370 - 640 nm, using least squares, Eq. (3.5), to yield the contributions of each. The extracted collagen-like (C_{337}) and elastin/lipid-like (E_{337}) coefficient indicate the contributions of collagen-like and elastin/lipid-like constituent spectra to the observed spectrum.

The Raman spectra were extracted after background subtraction, spectral response correction, and the removal of tissue fluorescence using a 6^{th} order polynomial. Then, the Raman spectra, normalized to peak height, were fit using least squares, Eq. (3.5), to the artery morphological model [85], to yield the fit coefficients or contributions of the Raman active components: collagen fibers (CF), cholesterol crystals (CC), calcium mineralization (CM), elastic lamina (EL), foam cells / necrotic core (FC/NC), β-carotene crystals (β-CC), smooth muscle cells (SMC), adventitial adipocytes (AA), hemoglobin (Hb), epoxy, sapphire, and water. The constituent Raman spectra of the morphological structures are given in Fig. 6-5e. The sum of the contributions was normalized to unity for each lesion; in this way, the coefficients provide a relative contribution of each particular constituent.

■ 6.2.4 Histological analysis

The demarcated tissue specimens were routinely processed, sectioned, and stained with hematoxylin and eosin. Histopathology for each of the specimens was performed by an experienced cardiovascular pathologist blinded to the spectroscopy results. Examples of several histological features of

the samples is presented in Fig. 6-3. The morphological features associated with plaque vulnerability were assessed: thin fibrous cap (TFC), necrotic core (NC) size, superficial foam cells (SFC), intralesional hemorrhage, and thrombus. The fibrous cap thickness was recorded as the range of thicknesses found underneath the ink dot (Fig. 6-3b,c); the fibrous cap was also examined for presence of rupture or ulceration (Fig. 6-3d). The necrotic core size was recorded as the maximum dimension of the core beneath the fibrous cap (Fig. 6-3c). The foam cells were evaluated based on the most superficial depth at which they were found and a density grade (0 = none; 1+ = isolated single foam cells; 2+ = small clusters of foam cells; 3+ = confluent sheets of foam cells) (Fig. 6-3f). Acute intralesional hemorrhage was identified as an accumulation of blood within the lesion, usually associated with the core (Fig. 6-3d,e). The presence of thrombus on the luminal surface of the artery was also noted (Fig. 6-3d).

To make the histological determination of plaque vulnerability as quantitative as possible, the following scheme is proposed. The vulnerable plaque index (VPI), developed by Dr. Maryann Fitzmaurice, assigns a numerical score to each plaque vulnerability feature depending on severity [89]. The VPI and the particular numerical scores have been validated through a small study of autopsy coronary artery specimens from patients that died from a myocardial infarction; a larger validation study is also planned. The VPI of a particular plaque is the sum of the individual scores and if this VPI is above some threshold, the plaque is deemed vulnerable. The scoring scheme for the various plaque vulnerability features in given in Table 6.1.

It should be noted from Table 6.1 that acute intralesional hemorrhage and thrombus are features of post-ruptured plaques. However, the hemorrhage or thrombus, if not associated with a previous fatal event, still pose a threat to the patient in terms of subsequent events and thus plaques with those features should be considered vulnerable by default. On the other hand, plaques with only

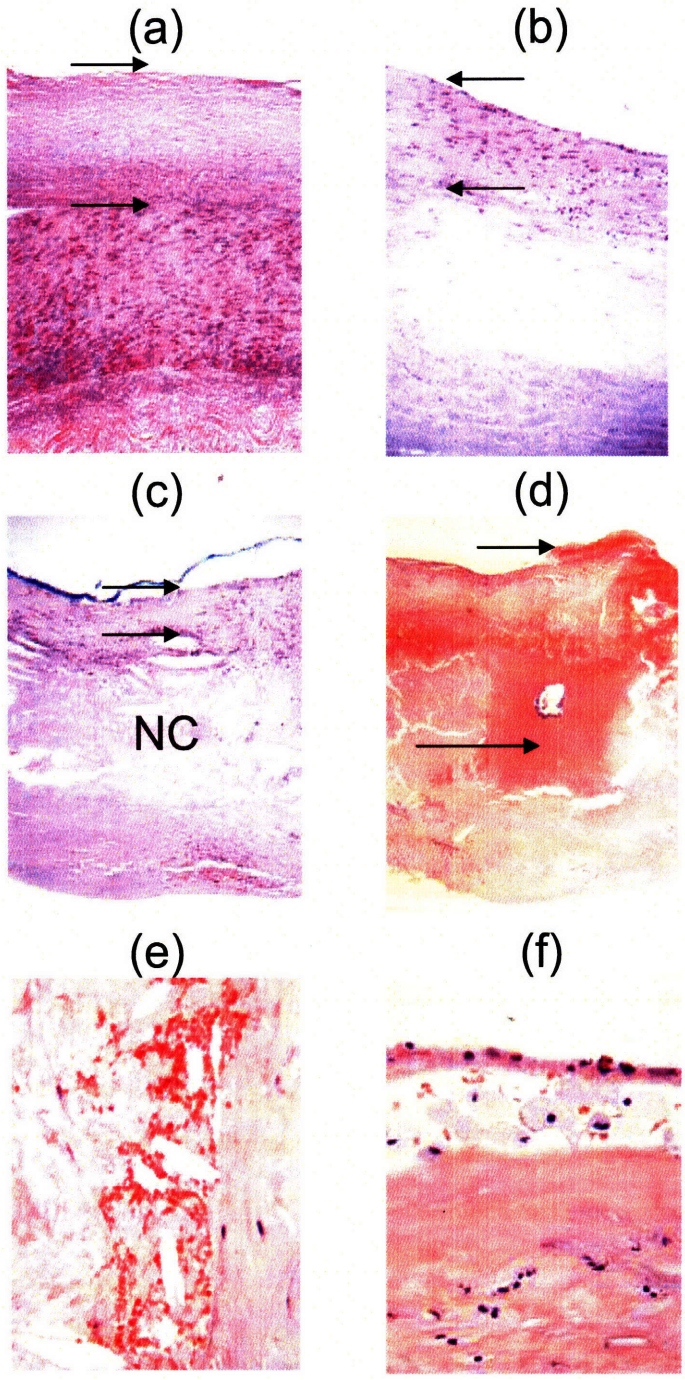

Figure 6-3. Photomicrographs of representative tissue sites: a) intimal fibroplasia (H&E; 10X; intimal thickness indicated by arrows); b) atherosclerotic plaque with thick fibrous cap (H&E; 10X; fibrous cap thickness indicated by arrows); c) thin fibrous cap atheroma (H&E; 10X; fibrous cap thickness indicated by arrows); d) ulcerated thin fibrous cap atheroma, with thrombus (short arrow) and acute intralesional hemorrhage (long arrow) (H&E; 4X); e) acute intralesional hemorrhage (H&E; 40X); f) superficial foam cells 3+ grade (H&E; 40X).

Criteria		Score
1. Thin fibrous cap$^{\Psi}$	ulceration*	10
	$\leq$ 65 μm	5
	65-100 μm	3
	100-120 μm	1
2. Necrotic core	$\geq$ 500 μm	5
	100-500 μm	3
	$\leq$ 100 μm	1
3. Superficial foam cells ($\leq$ 65 μm)	3+	5
	2+	3
	1+	1
4. Acute intralesional hemorrhage*		10
5. Thrombus*		10

Table 6.1. Vulnerable plaque index. The vulnerability of a particular plaque is determined by summing the scores of the individual morphological features determined to be present histologically. *Feature by itself indicates a vulnerable plaque. $^{\Psi}$Applies only to plaques and not to intimal fibroplasias.

the features of TFC, large NC and SFC are plaques that have presumably not ruptured yet and are vulnerable because they are rupture-prone. As such, it is reasonable to come up with two different approaches of using the VPI. In the first class, we can classify "early" or rupture-prone vulnerable plaques by considering only on the first three features of the VPI, by which a plaque is pronounced vulnerable if it has TFC, NC, or SFC that result in VPI $\geq$ 10. In the second class, we can classify "all" vulnerable plaques (rupture-prone or post-ruptured) by utilizing all five features of the VPI and pronouncing a plaque vulnerable if it has TFC, NC, SFC, hemorrhage or thrombus that result in VPI $\geq$ 10.

■ 6.2.5 Diagnosis and classification

In the most general terms, we shall be developing tests to detect the presence of a condition, as ascertained by some "gold standard." In our specific case, we shall be developing a spectroscopic test or classifier to detect the presence of a vulnerable plaque, a condition assessed by the gold standard of histology. To develop the classifier, we shall be utilizing the method of logistic regression

[150]. We shall be evaluating the robustness of the classifier by looking at its receiver operating characteristic (ROC) curve, as well as related metrics such as the sensitivity, specificity, positive predictive value (PPV), and negative predictive value (NVP). In order to show that the classifiers can generalize to prospective data, we shall be utilizing leave-one-out cross validation. More explicit details about the terminology, logistic regression, ROC curves, and cross validation can be found in Appendix B.

■ 6.3 Results

This section overviews the results obtained from this clinical study and can be broken down into three parts: the comparisons of *in vivo* and *ex vivo* spectra, the spectroscopic indications of plaque morphology, and the ability to detect features of vulnerable plaque.

■ 6.3.1 *In vivo* vs. *ex vivo*

We investigated the equivalence of spectroscopic data collected from patients *in vivo* to the spectra collected from approximately the same spectral locations from the excised specimen *ex vivo*. This comparison was performed for excised specimens kept in saline and spectrally analyzed within one hour after surgical excision. A comparison of MMS data taken *in vivo* and *ex vivo* from approximately the same locations of a carotid artery atherosclerotic plaque is given in Fig. 6-4. A few sites exhibited a greater discrepancy between the spectra collected *in vivo* and *ex vivo*, which was attributed to a registration/sampling error.

■ 6.3.2 Spectroscopic information

This section correlates the spectroscopic findings for each MMS modality to histopathology. The following analysis is based on the spectra collected *ex vivo* as only those could be registered to

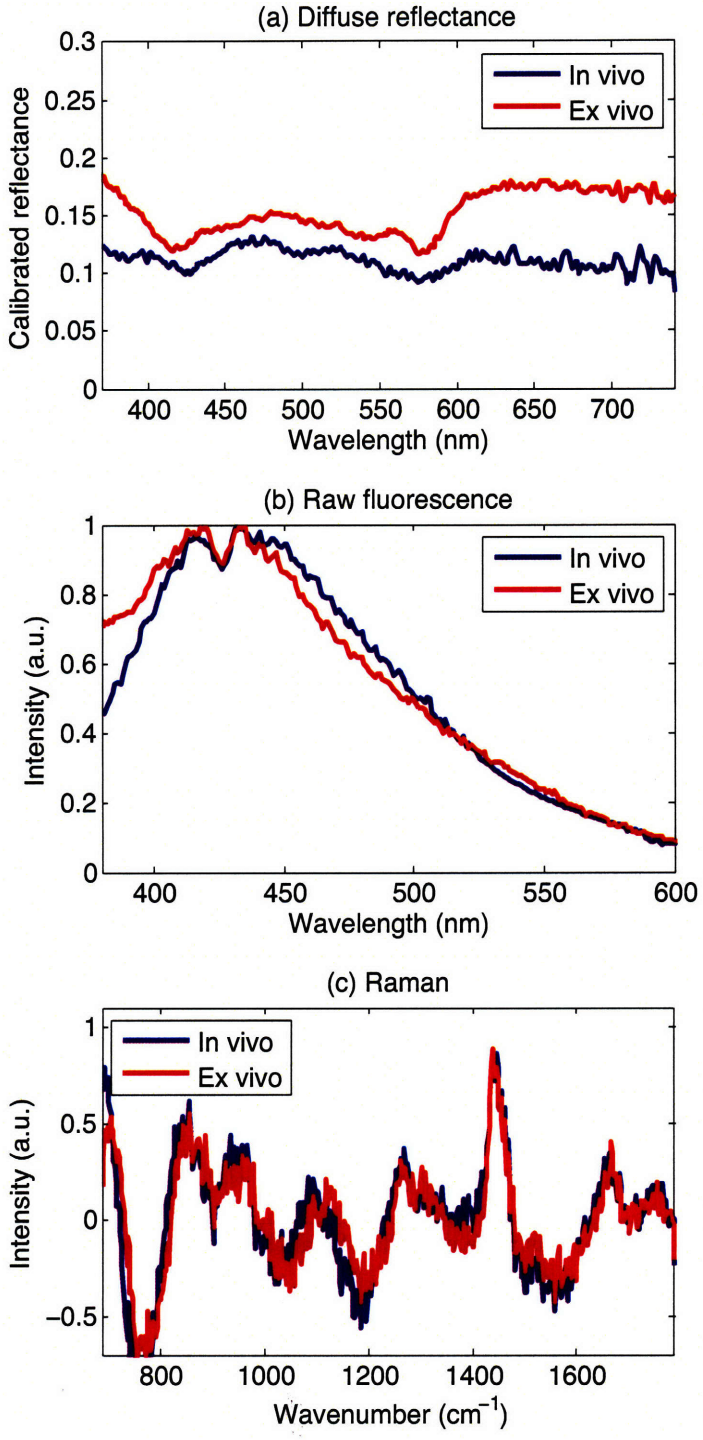

Figure 6-4. A comparison between *in vivo* and *ex vivo* data collected from approximately the same locations on a carotid artery atherosclerotic plaque for (a) DRS, (b) fluorescence, and (c) Raman spectra.

the corresponding histopathology with relatively high certainty. Representative spectra and fits for DRS, IFS, and Raman modalities are displayed in Fig. 6-5, collected from a carotid artery calcified atheromatous plaque. The excellent fits indicate that the spectral modeling is appropriate and adequate in accurately characterizing the experimental spectra. It should be noted that the DRS spectra containing a relatively large amount of β-carotene absorption, such as the spectrum in Fig 6-5b, did not result in a perfect fit because β-carotene has known environment-specific spectrum and is insoluble in aqueous media [64, 63]. This deviation points to an imperfect modeling of the β-carotene extinction spectrum (Fig. 6-5a) or the presence of an unknown absorber.

Occasional spectra were either too noisy, distorted by artifacts, or exhibited structural features that were not found in our existing models. For example, occasional DRS spectra collected from locations with a large amount of blood relative to sampling volume resulted in saturation of the ~420 nm soret band of hemoglobin; a good fit and a reliable extraction of c_{Hb} could not be obtained in some of these cases. Too much absorption in the DRS spectra also manifested itself in the corresponding IFS spectra as the spectral correction to extract IFS could not compensate for this level of absorption. Other IFS spectra simply had too low of a signal-to-noise ratio. Occasional Raman spectra also contained too much noise resulting from a relatively high amount of tissue fluorescence excited in the NIR relative to the Raman signal. If one of the MMS modalities did not have a good spectrum and fit, for the reasons mentioned, the entire lesion was excluded from the study. In total, 8 spectral locations were excluded from the study for reasons relating to the quality of the data and goodness of fit. Therefore, a total of 76 out of 84 spectral locations analyzed *ex vivo* were included in the following analysis.

The following extracted spectral parameters are utilized in the ensuing analysis of tissue characterization vulnerable plaque detection. From DRS, the parameter $c_{\beta-car}$ indicated the contribution

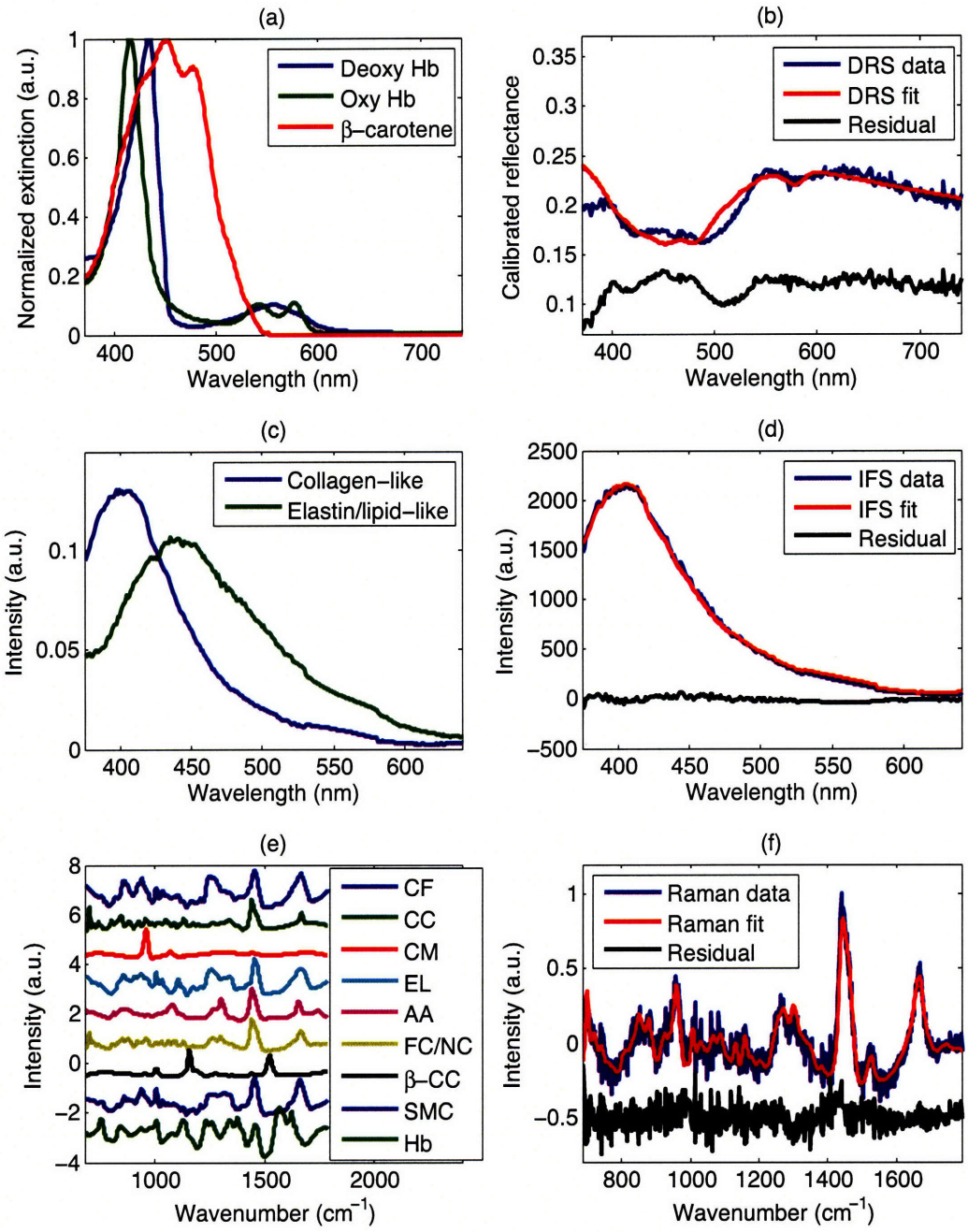

Figure 6-5. (a) Absorption coefficients used to model the tissue absorbers for DRS modeling; (b) representative data and fit for DRS; (c) basis spectra, obtained through MCR, used to model IFS spectra; (d) representative data and fit for IFS; (e) Raman morphological basis spectra; (f) representative data and fit for Raman. The representative spectra in (b), (d), and (f) are collected *ex vivo* from the same tissue location, a carotid artery calcified atheromatous plaque. The residuals in (b) and (f) are offset from zero for clarity.

of β-carotene to the absorption. From IFS, two parameters were defined: C_E as the energy-normalized contribution of the collagen-like spectrum and R_C as the relative amount of collagen specified by:

$$C_E = \frac{C_{337}}{< energy >}, \tag{6.5}$$

$$R_C = \frac{C_{337}}{C_{337} + E_{337}}, \tag{6.6}$$

where C_{337} is the collagen-like contribution, E_{337} is the elastin/lipid-like contribution, and <energy> is the excitation energy (μJ/pulse) used to excite fluorescence. Lastly, two Raman parameters were defined: CM as the extracted contribution by the calcium mineralization constituent spectrum and Σ to characterize the lipid core:

$$\Sigma = CC + FC/NC, \tag{6.7}$$

where CC and FC/NC are the contributions of the cholesterol crystals and the foam cells / necrotic core constituent spectra. As was done previously [86] to compensate for the pre-resonant Raman properties of β-carotene, the CM contribution was extracted by removing the contribution of the Raman β-CC constituent spectrum and renormalizing all other components to sum to unity. Similarly, to compensate the effects of calcification on the Raman spectrum of lipid core, the CC and FC/NC contributions were extracted after removing the contribution of the β-CC and the CM constituent spectra and renormalizing the remaining components to sum to unity [86].

■ 6.3.3 Histological findings

Detailed histological analysis was performed on all specimens. Owing to histological processing difficulties, two of the specimens were excluded from the study. These corresponded to samples that would have been excluded for reasons relating to the quality of data and fits, as discussed above.

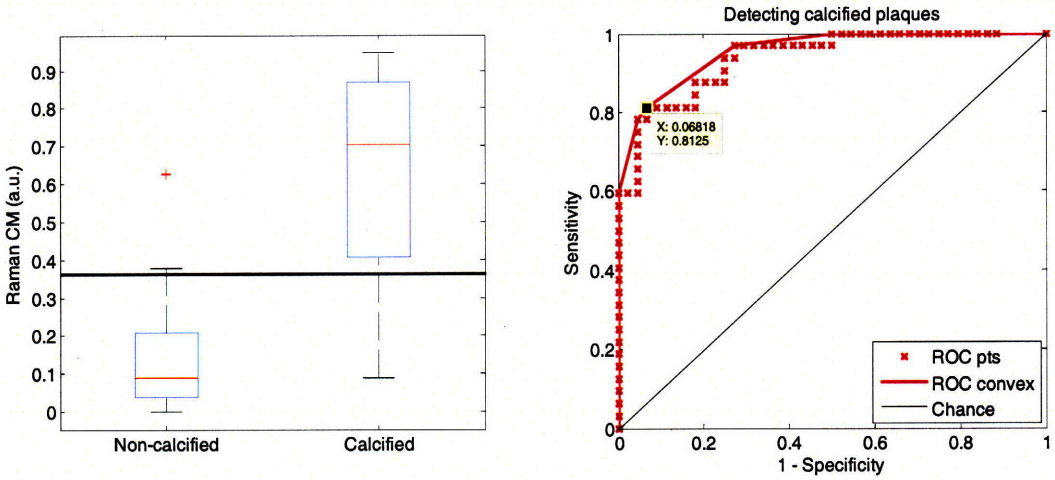

Figure 6-6. Box plot associated with the diagnostic algorithm (left) and ROC curve (right) for detecting calcified plaques using the Raman CM contribution. The chosen point on the ROC curve, represented by the decision threshold line on the left panel, indicates a sensitivity of 81% and a specificity of 93%. Area under the ROC curve = 0.955.

The remaining specimens exhibited a wide variety of morphological, structural, and pathological variations. The detailed morphological assessment following the criteria in Table 6.1 was performed for every lesion. In terms of the "early" vulnerability criteria, 23 specimens resulted in VPI $\geq$ 10 while the remaining 53 specimens had VPI $<$ 10. Using the "all" vulnerability criteria, 36 specimens had VPI $\geq$ 10 and 40 had VPI $<$ 10.

■ 6.3.4 Detecting calcified plaques

The Raman CM parameter was used previously to detect calcified plaques [86, 89]. To compare to those earlier studies, in Fig. 6-6 the box plot of the Raman CM contribution is given for lesions that were assessed to be non-calcified (n=44) and calcified (n=32) histologically. The box has lines at the lower quartile, median, and upper quartile values; the whiskers are lines, with a maximum length of 1.5 times the interquartile range, extending from each end of the box to show the extent of the rest of the data; outliers are data with values beyond the ends of the whiskers. Figure 6-6 also

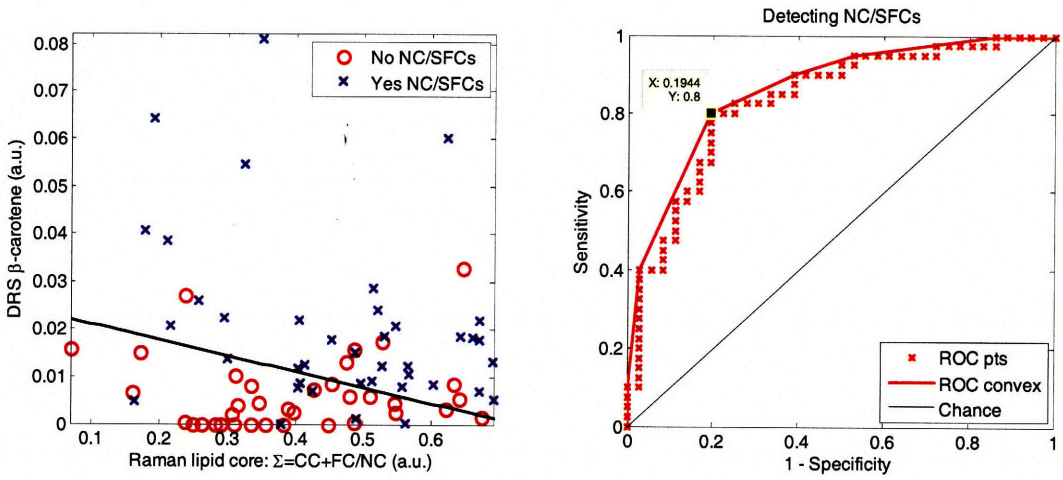

Figure 6-7. Diagnostic algorithm (left) and ROC curve (right) for detecting the presence of necrotic core and/or superficial foam cells using DRS β-carotene and Raman Σ. The chosen point on the ROC curve, specified by the given decision line (left), indicates a sensitivity of 80% and a specificity of 81%. Area under the ROC curve = 0.865.

displays the ROC curve for detecting calcified plaques using Raman CM and logistic regression, indicating that a specific classifier, indicated by the decision threshold line on the left panel, can achieve a sensitivity of 81% and a specificity of 93%. The area under the ROC curve is 0.955 out of a maximum of unity.

■ 6.3.5 Detecting NC/SFCs

Two spectral parameters were shown to have a significant correlation with the histologically confirmed presence of a NC and/or SFCs: the DRS $c_{\beta-car}$ ($p<0.0001$) and Raman Σ ($p<0.1$). Figure 6-7 presents a diagnostic algorithm based on logistic regression and an ROC curve for detecting the presence of a large NC or SFCs, indicating a sensitivity of 80% and a specificity of 81% for one particular classifier. The area under the ROC curve is 0.865. For the purpose of this diagnostic algorithm, 40 out of the 76 lesions were considered to exhibit this feature as they contained a large NC ($\geq$ 500 μm) or if SFCs ($\leq$ 65 μm) with a density of at least 3+ were present. In this way, the

algorithm is detecting at least a VPI contribution of 5 points based on the NC and SFC criteria (Table 6.1).

■ 6.3.6 Detecting a TFC

Two spectral parameters were shown to have a significant ($p<0.005$) correlation with the histologically thin fibrous cap, seen in 22 out of the 76 lesions: the IFS R_C and IFS C_E. Figure 6-8 presents a diagnostic algorithm based on logistic regression and an ROC curve for detecting a TFC, indicating that a sensitivity of 91% and a specificity of 62% can be achieved with a particular classifier. The area under the ROC curve is 0.851. A TFC was considered as such if the fibrous cap thickness was smaller than 65 μm at some location within the sampling area. In this way, the algorithm is detecting at least a VPI contribution of 5 points based on the TFC criterion (Table 6.1). For the purpose of developing the diagnostic algorithm only, the non-atherosclerotic intimal fibroplasia samples were excluded from the analysis as they are not proper plaques. (However, all samples were

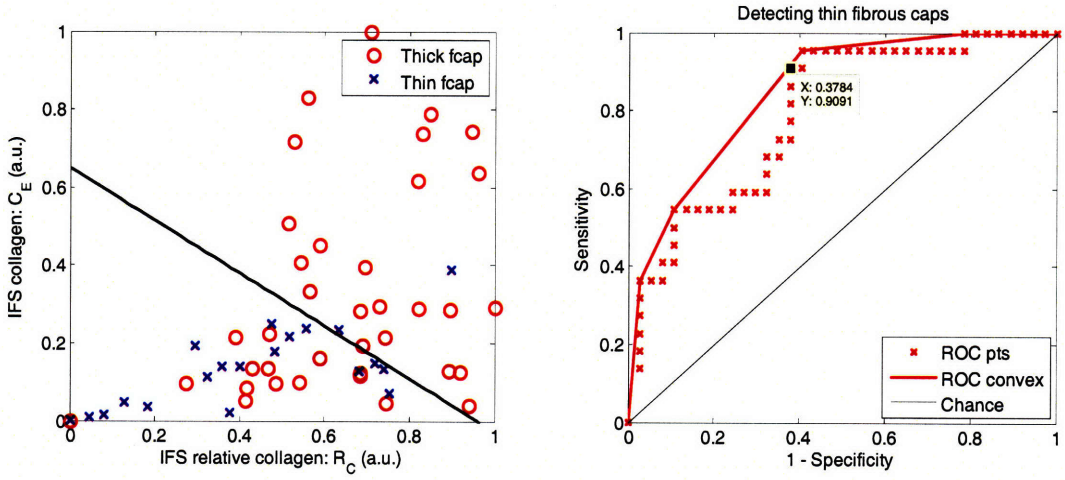

Figure 6-8. Diagnostic algorithm (left) and ROC curve (right) for detecting the presence of a thin fibrous cap ($\leq$ 65 μm) using IFS R_C and IFS C_E. The chosen point on the ROC curve indicates a sensitivity of 91% and a specificity of 62%. Area under the ROC curve = 0.851.

included in the ensuing application of the diagnostic algorithm and vulnerable plaque analysis.)

■ 6.3.7 Detecting thrombus

In the course of the study, we collected spectra from a macroscopically large (> 2 mm thick) thrombus that was excised from the lumen of an artery. The Raman spectrum from this thrombus can serve as a basis spectrum (Fig. 6-9a) to model the spectroscopic presence of a thrombus in other samples. Figure 6-9b shows the Raman spectrum of a thrombotic carotid plaque that was fit using the Raman morphological model. Some structure in the residual indicates that perhaps not all spectroscopic features are properly accounted for in the model. However, if the Raman morphological model is modified to also include the thrombus basis spectrum, a better fit to this thrombotic plaque is achieved (Fig. 6-9c), indicated by less visible structure in the residual as well as a 28% reduction in its magnitude.

All the Raman spectra were refit using a basis spectrum model that includes the thrombus spectrum. Seven specimens had a significant contribution (~10% of normalized Raman signal) from the thrombus basis spectrum. A diagnostic algorithm aiming to detect thrombus was developed using the Raman thrombus contribution and logistic regression. The box plot in the left panel of Fig. 6-10 indicates specimens that contained a histologically confirmed thrombus (n=13) had an elevated distribution of the Raman thrombus parameter. Conversely, specimens with no histologically confirmed thrombus (n=63) had a much reduced distribution of the Raman thrombus parameter, with the exception of several statistical outliers indicated. It should be noted that a thrombus was assessed histologically regardless of its physical size or extent. In this way, the algorithm is detecting a VPI contribution of 10 points based on the thrombus criterion (Table 6.1). The ROC curve is shown on the right panel of Fig. 6-10 with a particular operating point corresponding

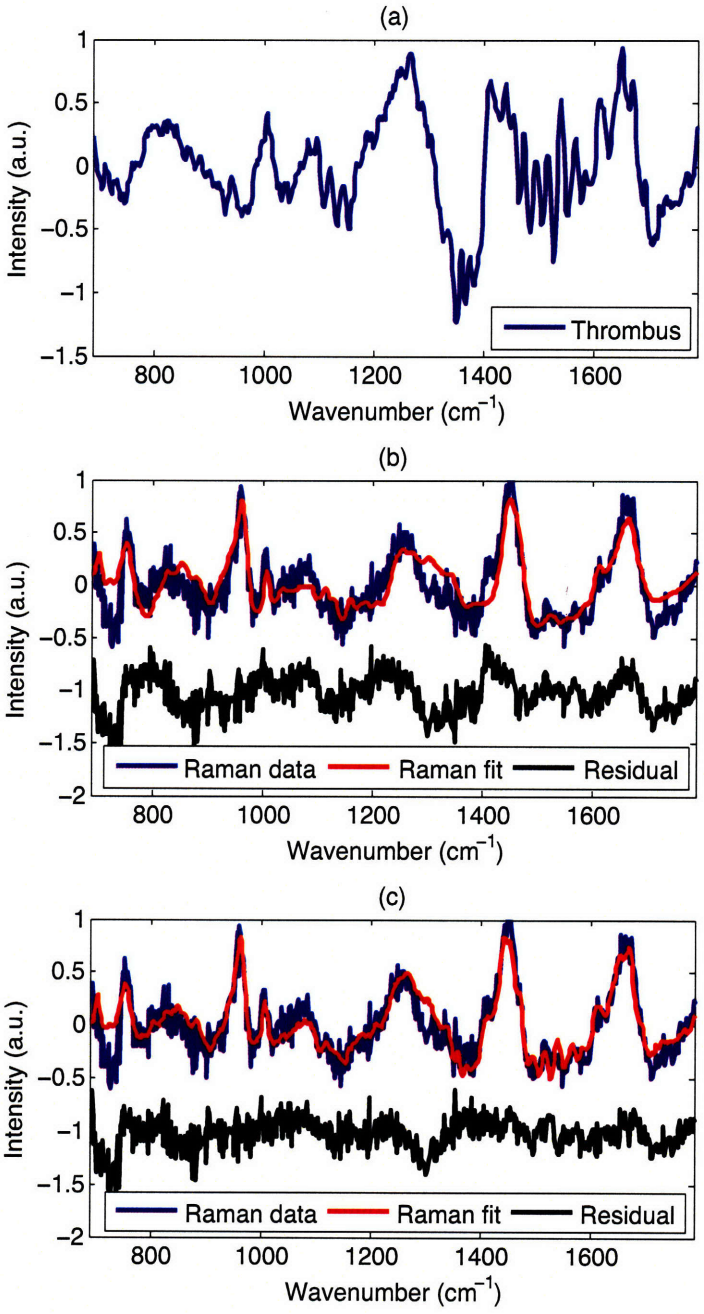

Figure 6-9. a) Raman basis spectrum of a thrombus; b) Raman spectrum of a thrombotic carotid plaque that was fit using the standard Raman morphological model basis spectra; c) Raman spectrum of the same thrombotic plaque fit using the standard Raman model plus the thrombus basis spectrum given in a).

to a sensitivity of 31% and a specificity of 97% associated with the decision threshold given on the left panel. The area under the ROC curve is 0.661.

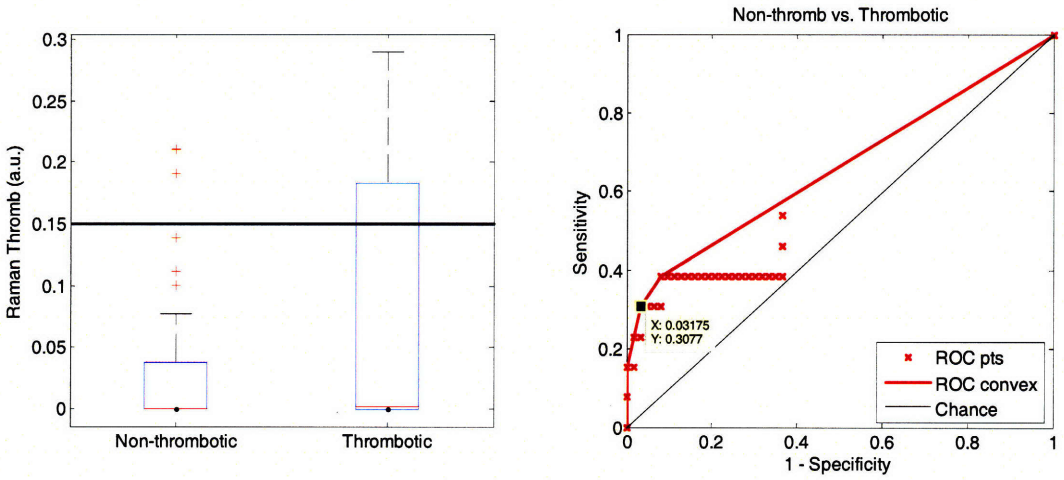

Figure 6-10. Diagnostic algorithm (left) and ROC curve (right) for detecting the presence of a thrombus using the Raman thrombus contribution. The chosen point on the ROC curve indicates a sensitivity of 31% and a specificity of 97%. Area under the ROC curve = 0.661.

■ 6.3.8 Detecting "early" vulnerable plaques

The described spectroscopic diagnostic algorithms were used together to detect the presence of vulnerable plaques based on the "early" vulnerability criteria.

Plaques were considered histologically vulnerable if they had a calculated VPI $\geq$ 10 based on the first three features in Table 6.1, namely TFC, NC, and SFC. The spectroscopic algorithm to detect the presence of "early" vulnerable plaques is presented in Fig. 6-11. The combined diagnostic algorithm uses the two individual spectroscopic algorithms for TFC and NC/SFC as decision stumps, requiring both to be positive for the combined algorithm to return positive. Since each individual algorithm was tuned to detect a 5 point contribution to the VPI, the combined algorithm would thus be detecting lesions with a VPI $\geq$ 10. The specific operating points on

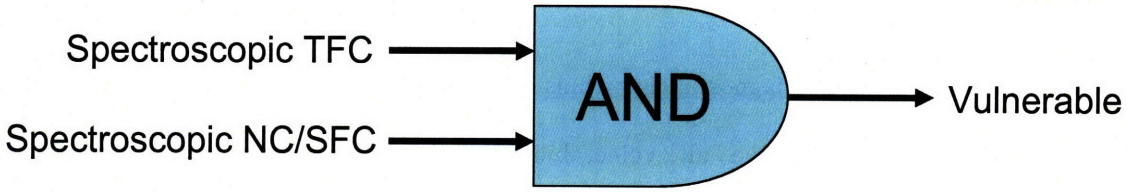

Figure 6-11. Spectroscopic algorithm for the detection of "early" vulnerable plaques. The output of the algorithm classifies a plaques as vulnerable if both of the individual spectroscopic algorithms for TFC and SFC/NC return positive.

the ROC curve of each individual spectroscopic algorithm were chosen to maximize the combined algorithm accuracy of detecting "early" vulnerable plaques. The ROC curve for the combined algorithm, using logistic regression and leave-one-out cross validation, is shown in Fig. 6-12 and the area under the ROC curve is 0.886 out of a maximum of unity. We can select a particular point on the ROC curve (indicated) that achieves a sensitivity of 96% (22/23), specificity of 72% (38/53), PPV of 59% (22/37), and NPV of 97% (38/39). The decision chart including breakdowns among true positives (TP), true negatives (TN), false positives (FP), and false negatives (FN) for that particular operating point is also shown in Fig. 6-12.

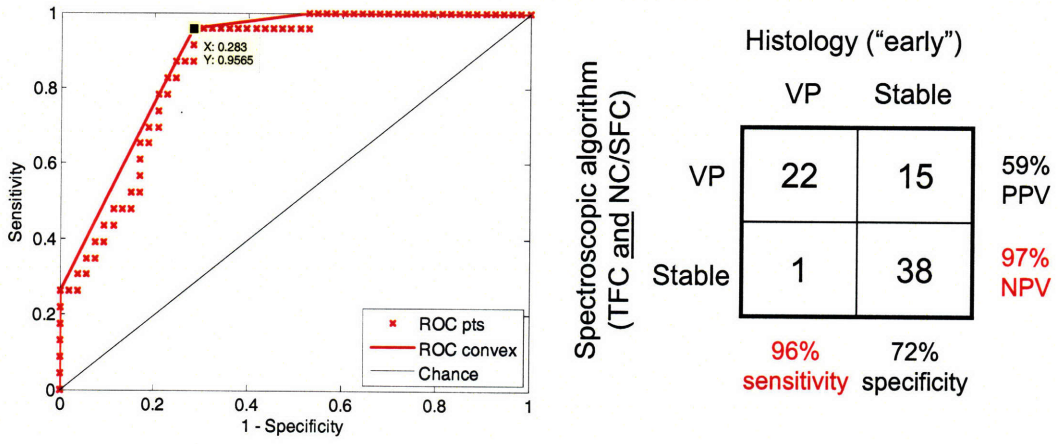

Figure 6-12. ROC curve for the combined algorithm (left) for the detection of "early" vulnerable plaques, and the decision chart (right) for the particular operating point indicated on the ROC. Area under the ROC curve = 0.886.

■ 6.3.9 Detecting "all" vulnerable plaques

The described spectroscopic diagnostic algorithms were also used together to detect the presence of vulnerable plaques based on the "all" vulnerability criteria.

Plaques were considered histologically vulnerable if they had a calculated VPI $\geq$ 10 based on all five features in Table 6.1, namely TFC, NC, and SFC, acute intralesional hemorrhage, and thrombus. If the same spectroscopic algorithm that was used to detect "early" vulnerable plaques (Fig. 6-11) is used here, it achieves a sensitivity of 81% (29/36), specificity of 80% (32/40), PPV of 78% (29/37), and NPV of 82% (32/39). In an effort to improve the classification, the spectroscopic algorithm was modified to include diagnostic information from thrombus. This modified spectroscopic algorithm to detect the presence of "all" vulnerable plaques is presented in Fig. 6-13. The combined diagnostic algorithm uses the three individual spectroscopic algorithms for TFC, NC/SFC, and thrombus as decision stumps, requiring either NC/SFC and TFC to return positive or for thrombus to return positive in order for the combined algorithm to return positive. As a result, the output of this combined algorithm would be detecting lesions with VPI $\geq$ 10. The specific operating points on the ROC curves of each of the three individual spectroscopic algorithm were chosen to maximize the combined algorithm accuracy of detecting "all" vulnerable plaques. The

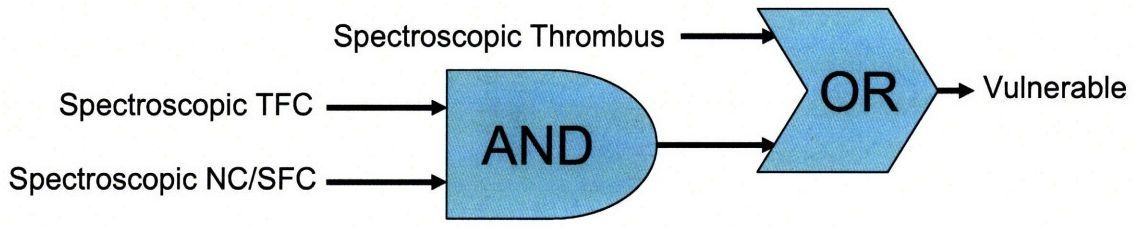

Figure 6-13. Spectroscopic algorithm for the detection of "all" vulnerable plaques. The output of the algorithm classifies a plaques as vulnerable if either the individual spectroscopic algorithms for TFC and SFC/NC return positive or if the spectroscopic algorithm for thrombus returns positive.

ROC curve for the combined algorithm, using logistic regression and leave-one-out cross validation, is shown in Fig. 6-14 and the area under the ROC curve is 0.901 out of a maximum of unity. We can select a particular point on the ROC curve (indicated) that achieves a sensitivity of 89% (32/36), specificity of 78% (31/40), PPV of 78% (32/41), and NVP of 89% (31/35). The decision chart including breakdowns among TP, TN, FP, and FN for that particular operating point is also shown in Fig. 6-14.

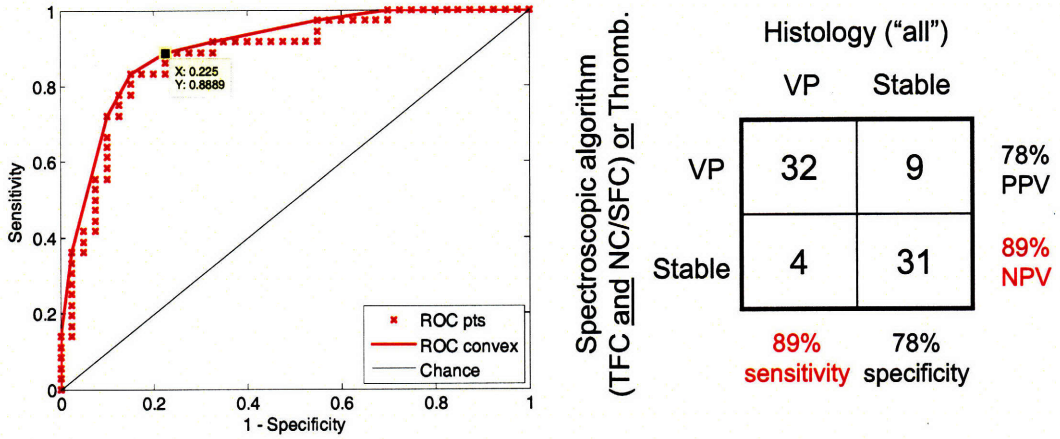

Figure 6-14. ROC curve for the combined algorithm (left) for the detection of "all" vulnerable plaques, and the decision chart (right) for the particular operating point indicated on the ROC. Area under the ROC curve = 0.901.

■ 6.4 Discussion

This section discusses the findings and diagnostic implications of the presented results.

■ 6.4.1 *In vivo* vs. *ex vivo*

The first achievement of this study is the demonstration of the ability to collect MMS data *in vivo* from human patients in clinically acceptable times. This finding underscores the potential future use of the technique for diagnostic applications. Also, given the demonstrated equivalence

of *ex vivo* and *in vivo* spectroscopic data (Fig. 6-4), it is justified to use the *ex vivo* spectral findings correlated to histology on the assumption that the results hold for both *ex vivo* and *in vivo* applications. Any discrepancies between the spectra collected *ex vivo* and *in vivo* are attributable to either registration errors or subtle changes in the experimental environment (e.g. inadequate saline rinse prior to spectral collection *in vivo* compared to *ex vivo*).

■ 6.4.2 Spectroscopic information

The quantitative spectroscopic information provided by MMS correlates with the histology. Moreover, there is sound physical basis and justification for the agreement between spectroscopy and histology rather than simply statistical correlations. For example, the CM parameter indicates the highly specific observed signature of the calcium mineralization that is able to discern hard plaques from soft plaques. Similarly, the absorption attributed to β-carotene indicates the presence of this molecule, which is known to be lipid soluble and thus likely to be found within the NC or foam cells. In addition, the IFS contribution of collagen identifies the main component of the plaque fibrous cap and therefore it is natural for there to be a correlation between the spectroscopic and histologic findings. Lastly, the high molecular specificity of Raman spectroscopy can also be used to detect thrombus on the surface of a plaque through the spectroscopic signature of a pure thrombus.

■ 6.4.3 Detecting calcified plaques

It should be noted that there is no clear consensus in the literature about the impact of calcification on plaque vulnerability. Therefore, this feature was not included in the VPI but we will nevertheless comment on our ability to detect calcifications. The described algorithm for detecting calcified plaques is consistent with previously published algorithms [86, 89]. The high accuracy of detection is testament to the high molecular specificity of Raman spectroscopy relating to calcium deposits.

The misclassified samples are easily explained: the false positive samples are most likely the result of calcium deposits that are missed on histologic examination owing to registration and sampling error associated with processing of slides; the false negative results are caused either by calcium deposits that are too small in physical extent or found too deep in tissue, beyond the probe sampling volume. It should be noted that small or deeply seated calcification may not be clinically relevant as some suggest that it is only the exposed surface calcification that poses a risk of plaque rupture [8].

■ 6.4.4 Detecting NC/SFCs

The described algorithm for detecting NC and SFCs is consistent with previously published work, indicating that the presence of β-carotene from DRS [64] and the Raman Σ contribution [89] are associated with plaque cores and SFCs. However, this is the first time that such an algorithm is proposed that utilizes both DRS and Raman spectral parameters in a joint classification. It makes physical sense that lesions that do not contain large necrotic cores or confluent aggregations of SFCs on average exhibit a low value of DRS β-carotene and Raman lipid core (Σ) contributions. Moreover, looking at Fig. 6-7, one should note that the two contributions compensate for each other. In other words, certain lesions can contain high values of Σ while having low values of β-carotene; this can be explained either by the relatively deeper sampling depth of Raman spectroscopy that can better assess deeper-lying NC than DRS or perhaps simply the absence of lipid-soluble β-carotene in that particular lesion. The reverse argument, having high amounts of β-carotene with low values of Σ is likely caused in the presence of calcification that tends to dominate the Raman signal, even with the compensation described in computing Σ. The misclassified samples in the zone around the boundary line in Fig. 6-7 are best explained by the arbitrary cutoff for defining a large NC ($\geq$ 500

μm) or an accumulation of SFCs (density 3+), or the presence of NC too deep in tissue, beyond the sampling volume of the probe. It should be noted explicitly many of these misclassifications would be expected since spectroscopy may see all the full range of gradual changes in morphology whereas the cutoffs used to call a feature "large" or "small" histologically can create a somewhat unnatural grouping.

■ 6.4.5 Detecting a TFC

Utilizing fluorescence to detect the size of a plaque fibrous cap has been done previously [70, 131]. The diagnostic algorithm presented in Fig. 6-8 makes physical sense as thicker fibrous cap samples had, on average, a larger contribution of collagen, indicated by the high values of both R_C and C_E. Conversely, TFC samples had lower values of those two IFS parameters. The chosen classification boundary exhibits a very high sensitivity at the expense of a low specificity. The false positive samples, the histologically thick fibrous caps that were misclassified spectroscopically as TFCs, are almost all explained by the presence of SFC in the fibrous cap. Since the IFS contributions of elastin and of lipids are similar and represented by the elastin/lipid-like IFS constituent spectrum, an accumulation of SFC can boost the elastin/lipid signal at the expense of the collagen-like signal to give an IFS similar to that of a thin fibrous cap over a necrotic core. The remaining false positive samples are likely explained by the variable size fibrous cap which can be locally thinner though not below the stated 65 μm limit. On the other hand, some of the TFC with relatively higher values of R_C and C_E are explained by observing that a thin or ruptured fibrous cap can also have adjacent regions of much thicker fibrous cap within the sampling volume of the probe. Again, it should be noted that some of these misclassifications would be expected since the thinness of a fibrous cap is based on the discrete 65 μm cutoff whereas the spectroscopy really sees the full range of gradual

changes, given its sampling volume.

■ 6.4.6 Detecting thrombus

Attempting to detect thrombotic plaques using the Raman spectroscopic signature of pure thrombus has not, to our knowledge, been done before. We were able to extract a Raman spectrum from a pure thrombus and verify features of that spectrum in several thrombotic specimens with large thrombi. Moreover, features of the thrombus basis spectrum can be seen in the known Raman spectra of platelets [151], fibrin [152], and hemoglobin (Fig. 6-5e), the physical constituents of thrombus (data not shown). However, several other histologically thrombotic specimens did not contain a contribution from the thrombus basis spectrum; these are most likely explained by the relative small physical size (average thickness $\sim$150 μm) of these thrombi. In addition, several specimens without histologically confirmed thrombi exhibited a significant contribution from the Raman thrombus spectrum. These outliers are most likely explained by a registration issue or other problem during the histology processing that could have perhaps caused a thrombus to be overlooked histologically. Moreover, the Raman thrombus basis spectrum was not able to pick up the presence of an acute intralesional hemorrhage. This may be somewhat surprising since thrombi and hemorrhages are expected to be similar in composition. However, given that thrombi are on the surface of a plaque compared to the deeper lying hemorrhages, the inability to detect hemorrhages is perhaps explained by sampling volume considerations.

■ 6.4.7 Detecting vulnerable plaques

We have demonstrated the ability to use the aforementioned individual diagnostic algorithms to detect vulnerable plaques. The first algorithm (Fig. 6-11) detects "early" vulnerable plaques with an excellent overall accuracy. The one false negative vulnerable plaque is the result of not being

able to detect its thin fibrous cap by the individual TFC algorithm. The 15 false positive results are not a concern diagnostically since six of those samples contained hemorrhage or thrombus from an adjacent plaque which was not counted using the "early" criteria, and one may not see them as real false positives. Moreover, the average VPI of these false positives (using the "all" criteria) was 8, which is very close to the threshold of 10 for defining a vulnerable plaque.

Turning to "all" vulnerable plaques, the combined TFC and NC/SFC algorithm (Fig. 6-11) alone does not achieve as high of a sensitivity. It should be noted that several plaques would be considered vulnerable by the "all" criteria by having a thrombus or hemorrhage but without having a combination of TFC and NC/SFCs. Therefore, it is not surprising that these specimens are missed by the algorithm that is not tuned to the exact criteria for vulnerability. The modified algorithm (Fig. 6-13) for detecting "all" vulnerable plaques by a combination of TFC and NC/SFC or thrombus is able to significantly improve the sensitivity by detecting three additional thrombotic plaques, with only a slight reduction in specificity owing to one additional false positive, a plaque without a histologically confirmed thrombus that is incorrectly classified as thrombotic. The remaining three false negatives are explained by the inability to detect plaques with an acute intralesional hemorrhage. In our first MMS study [131], we claimed the possibility, though based on a single specimen, to detect intralesional hemorrhage through a markedly higher contribution of hemoglobin in DRS. In addition, previous work with Raman spectroscopy *in vivo* [89] indicated the potential to detect thrombotic and hemorrhagic plaques using the Raman hemoglobin contribution. However, the underlying assumption in both cases was that hemoglobin-containing red blood cells would be found at the site of an intralesional hemorrhage or thrombus. Several specimens in the present data set contained intralesional hemorrhage that our spectroscopic technique probably could not detect because the hemorrhage sites were mainly composed of platelets and fibrin with

few, if any, red blood cells. Another explanation for the difficulty in detecting hemorrhage compared to thrombus (since the two should be physically similar) is the fact that hemorrhage, found deeper inside the artery wall, arguably contributes less to the overall signal given the sampling volume and light attenuation in tissue, compared to a surface thrombus.

Finally, we should note that perhaps the most clinically important statistic for these classifiers is the NPV. That is, if the MMS technique is to be used to detect vulnerable plaques and thus indicate locations for treatment, it is of greatest importance to not miss any vulnerable plaques. In other words, false negatives should be minimized even if it comes at the expense of unnecessary false positives. Unnecessarily treating a stable plaque is acceptable as long as all vulnerable plaques are also treated. Therefore, having a high NVP value and being certain that the examined artery location is stable and does not require treatment is arguably the most important criterion. The relatively high demonstrated NPVs of 97% and 89% for the detection of "early" and "all" vulnerable plaques, respectively, attest to the robustness of MMS technique as a diagnostic tool.

■ 6.4.8 Comparison to pilot study

In this section, we compare the ability to detect features of vulnerability of the present study to that of the pilot study from Chapter 2. We shall compare the results from the two studies directly even though there are several substantial differences between the two studies which may render a direct comparison inappropriate. First, the present study utilized fresh specimens whereas the pilot study used previously frozen specimens. Second, the present study utilized a single MMS instrument and probe whereas the pilot study used two clinical instruments and two different probes to collect all MMS modalities. As a result, not only were the chances of registration errors greater in the pilot study, but the different probes sampled slightly different tissue volumes. Third, and perhaps most

importantly, the present study is much larger, with 76 spectral locations from 11 patients whereas the pilot study contained 17 spectral locations from 8 patients.

The pilot study claimed an ability to detect intraplaque hemorrhage using the DRS hemoglobin contribution. However, this was based on a single hemorrhagic specimen and this result is, therefore, not inconsistent with the inability of the much larger present study to detect hemorrhage through DRS. Differences between tissue in the fresh versus post-frozen state may also account for the difference.

The pilot study also claimed the ability to detect foam cells using the scattering parameter A from DRS. However, not much distinction had been made in the pilot study regarding the superficiality of foam cells using the 65 μm criterion as in the VPI. Also, the statistical significance of the scattering parameter A across the two groups was not calculated in the small data set of the pilot study. In the present study, a trend toward increased scattering and a higher scattering parameter A for specimens with SFCs was observed (data not shown), but this trend was not statistically significant and could not be used robustly to detect lesions with SFCs. The two studies are consistent with associating increased scattering with foam cell presence.

The pilot study claimed the ability to detect a TFC using the parameter ρ from IFS excited at 308 nm and 340 nm, or, equivalently, by using the parameter R_C from 340 nm excitation IFS. The present study also used the parameter R_C from 337 nm excitation IFS to detect a TFC. In addition, the present study additionally used the parameter C_E to provide intensity information and improve detection of a TFC, which the pilot study did not as excitation energy information was not available. Therefore, the present study verified the claim of the pilot study to detect a TFC using IFS but went further to utilize two parameters. Also, the present study identified a previously unknown limitation to specificity in detecting a TFC relating to the presence of foam

cells in a thick fibrous cap.

The pilot study claimed the ability to detect a NC using the Raman Σ contribution. The present study also utilized the Σ contribution. However, the present study also additionally utilized the more diagnostic DRS β-carotene contribution to detect the presence of NC/SFCs. The specimens in the pilot study did not contain appreciable amounts of β-carotene, perhaps a sampling limitation in a small data set. Therefore, the present study verified the claim of the pilot study to detect NC using Raman Σ but went further to jointly include DRS β-carotene. The present study also indicated across a larger data set that both of the parameters could not separate contributions of NC from that of SFCs.

The present study demonstrated, for the first time, the ability to detect thrombotic plaques. None of the specimens in the pilot study were thrombotic, which is perhaps another sampling limitation of the small data set. The present study also demonstrated the ability to detect vulnerable plaques, using two criteria, something that the pilot study could not even attempt. In conclusion, the present study used and verified many of the claims of the pilot study, but went significantly further and not only demonstrated a robust ability to detect features of vulnerability in a larger set of specimens, but also the ability to detect vulnerable plaques as defined by the VPI.

■ 6.5 Summary

This is the first demonstration of MMS performed *in vivo* in humans to study arterial lesions. We have demonstrated the clinical feasibility of collecting and analyzing the data in the operating room, giving real-time feedback to the physician. There is good agreement between data taken *in vivo* and *ex vivo* with any differences attributable mainly to registration errors. The extracted spectral parameters and the corresponding histological findings are in good agreement. We demonstrate

the ability to detect calcified plaques, lesions with large necrotic core and/or superficial foam cells, and plaques with thin fibrous caps. In addition, we demonstrated the ability, for the first time, to detect a thrombus on the surface of a plaque using its Raman spectral signature. To achieve this, several parameters from the individual MMS modalities are used, always with a physical basis for comparisons. Most importantly, we demonstrate the ability to detect vulnerable plaques with a sensitivity of 89-96% and a negative predictive value of 89-97%. These encouraging results indicate the ability for MMS to serve as a robust clinical diagnostic technique.

■ 6.6 Addendum: Ceroid, the unknown absorber?

As noted earlier, DRS spectra containing a relatively large amount of β-carotene absorption, such as the spectrum in Fig 6-5b, did not result in a perfect fit using our model. This pointed to an imperfect knowledge of the β-carotene absorption spectrum or the presence of an unknown absorber. There is reason to believe that the unknown absorber is ceroid, a peroxidized lipid-protein complex within which most oxidized LDL is contained in foam cell lysosomes [153]. Ceroid is insoluble in aqueous and organic solvents and its *in vivo* composition remains largely speculative, but it is believed to have toxic properties that result in plaque progression and ultimately plaque irreversibility [154].

The extinction spectrum of ceroid is very similar to that of β-carotene, as indicated in Fig. 6-15a; the extinction spectrum was collected on a ultraviolet-visible spectrophotometer (personal communication from Dr. John Kramer). Figure 6-15b shows the same DRS spectrum and fit from Fig. 6-5b, where the DRS data is fit using the extinction spectra of oxy-hemoglobin, deoxy-hemoglobin, and β-carotene only. However, when the same DRS data is fit using, in addition, the extinction spectrum of ceroid, a much improved fit is obtained, presented in Fig. 6-5c. This observation, true

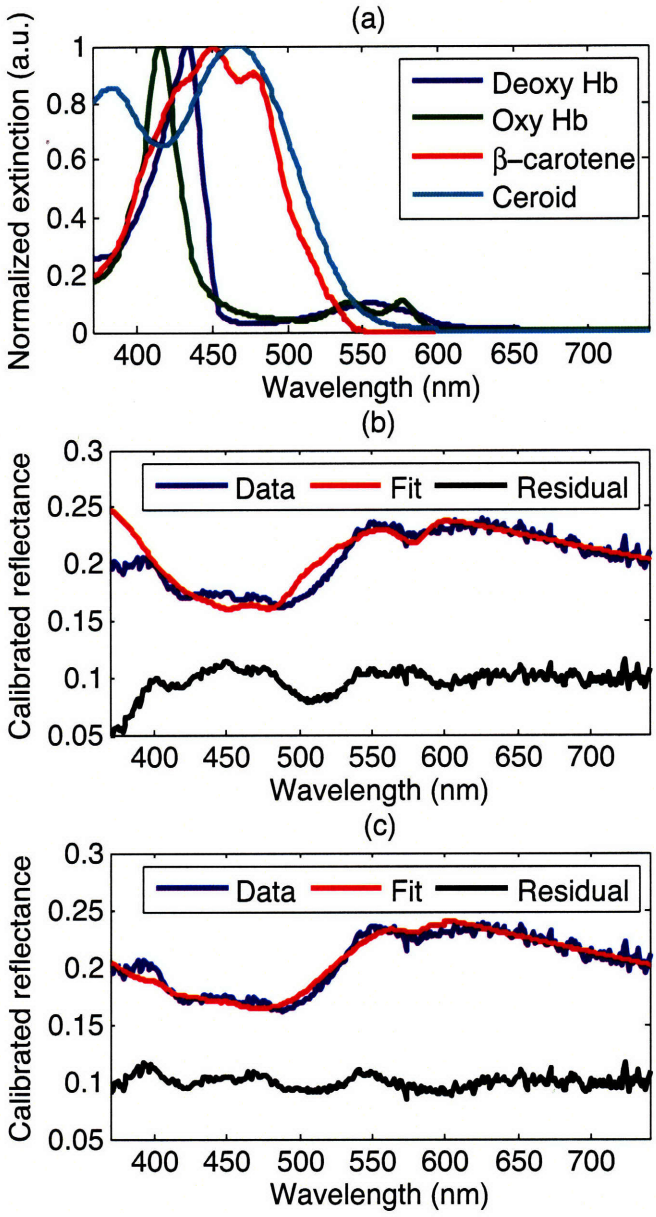

Figure 6-15. (a) Absorption coefficients used to model the tissue absorbers for DRS modeling, including ceroid; (b) DRS data and fit from Fig. 6-5b, where modeling does not include ceroid; (c) DRS data from Fig. 6-5b and fit, where modeling includes ceroid. The residuals in (b) and (c) are offset from zero for clarity.

across the specimens with pronounced β-carotene-like absorption features, indicates that perhaps ceroid is also present in those lesions and detectable through DRS.

All the DRS spectra were re-fit having the ceroid absorption spectrum included in the modeling. The fit coefficients of DRS spectra that were dominated by hemoglobin features (and with little or no β-carotene features), were unchanged. However, the DRS spectra with pronounced β-carotene features usually resulted in a lower relative extracted $c_{\beta-car}$ and a nonzero contribution of ceroid. This effect was expected owing to the substantial spectral overlap between β-carotene and ceroid, which allows the two extinction spectra compensate for one another.

The inclusion of ceroid in the DRS analysis does not have a significant impact on the diagnostic power of MMS and ability to detect vulnerable plaques. The algorithm to detect NC/SFC using only the re-fit $c_{\beta-car}$ and Σ achieves, as anticipated, a poorer performance than described in Sec. 6.3.5. However, if the algorithm is modified to include all three parameters ($c_{\beta-car}$, Σ, and the contribution of ceroid), the performance is improved by a few percent relative to Sec. 6.3.5, achieving an area under the ROC curve of 0.873. The impact of this modified NC/SFC algorithm on the performance of the overall algorithms to detect "early" (Fig. 6-11) and "all" (Fig. 6-13) vulnerable plaques is minimal, resulting in areas under the ROC curves of 0.896 and 0.899, respectively.

■ 6.7 Acknowledgements

Dr. Arnold Miller, a vascular surgeon at MetroWest Medical Center, was the principal collaborator who enabled us to collect MMS spectra from patients undergoing surgeries. Dr. Maryann Fitzmaurice, a pathologist at Case Western Reserve University, performed the detailed histological readings and made key contributions to data interpretation. Chae-Ryon Kong and Zoya Volynskaya assisted with the data collection.

Chapter 7

Accomplishments of this thesis

This chapter summarizes the present work by commenting on the goals that have been achieved and discusses any limitations.

■ 7.1 Diagnostic ability of MMS

This diagnostic potential of MMS was shown through a pilot *in vitro* study. In this study, spectra were collected using two different instruments and two differen probes, all previously developed in our laboratory. This study demonstrated the feasibility of using MMS to detect morphological markers of vulnerable plaque, specifically intraplaque hemorrhage, superficial foam cells, thin fibrous cap and large necrotic core. In view of the small size of the sample set, those promising results were considered preliminary, but they nevertheless provided the motivation to continue pursuing MMS. The subsequent work ultimately led to the development of integrated probes and instrumentation and the ability to apply MMS *in vivo* in a much larger study.

■ 7.2 Quantitative data analysis

We have made a significant advancement in quantitative data analysis by developing a simple and direct method for calculating the uncertainty from a single spectroscopic measurement. The experimental usefulness of the analytic Δc expression was demonstrated both for solution mixtures

and human tissue. In addition to calculating parameter uncertainties, the mathematical framework assesses the calibration and consistency of the experimental apparatus and allows experimentalists to verify that their spectral parameters contain the minimum possible uncertainty. Future work in this field may include developing analytical expressions for characterizing uncertainty in nonlinear models, such as diffuse reflectance.

■ 7.3 Spectral probe development

We have made a significant advancement by developing an integrated MMS probe, capable of efficiently collecting reflectance, fluorescence, and Raman signals from the same location in tissue. This is, to our knowledge, the first probe capable of collecting all three MMS modalities over the wide wavelength range of 300-1000 nm in a clinically acceptable time. We also demonstrated careful understanding of the optical properties of the probe by performing tissue-mimicking phantom experiments. The MMS probe can be used in many diagnostic settings apart from analyzing artery tissue. In fact, it is presently also under investigation in studies of breast cancer. Future probe work may include the development of side-viewing probes capable of intravascular applications as the techniques are being pushed toward more clinical use. To enable intravascular use, several issues would need to be resolved such as registering the probe against the artery wall and removing blood from the field.

■ 7.4 Clinical instrumentation development

We have made a significant instrumentation advancement by developing an integrated MMS system. This instrument is used together with the MMS probe to collect reflectance, fluorescence, and Raman signals and provide real-time diagnostic information. The MMS instrument is ideally

suited for clinical applications as it is compact and portable, taking advantage of technological improvements to reduce the size and cost of the system. Similarly as the probe, the MMS instrument can be used for multiple applications, in addition to studying arterial lesions. Future instrumentation improvements may include further miniaturization of the system by the utilization of a single spectrograph and a single CCD camera, once the technology becomes available.

■ 7.5 Clinical implementation of MMS

Finally, we have achieved a challenging clinical and diagnostic goal with the first demonstration of MMS performed *in vivo* in humans to study arterial lesions. We have shown the clinical feasibility of collecting and analyzing the MMS data from multiple patients and demonstrated the ability to detect calcified plaques, lesions with large necrotic core and/or superficial foam cells, and plaques with thin fibrous caps. In addition, we demonstrated the ability, for the first time, to detect a thrombus on the surface of a plaque using its Raman spectral signature. Most importantly, these results translate into the capability to detect vulnerable plaques with a sensitivity of 89-96%, specificity of 72-78%, and a negative predictive value of 89-97%. Future clinical steps may be toward intravascular demonstration of MMS. Also, understanding the scattering properties of foam cells may improve the ability to discern foam cells from necrotic core spectroscopically. Lastly, improving the detection of post-rupture vulnerable plaques would require a better understanding of the chemical composition of thrombus and intralesional hemorrhage at various stages of disease.

Chapter 8

Future directions

This chapter proposes some future directions that may be explored in light of the results of this thesis.

8.1 Improving detection of VPs

8.1.1 Advanced classification

This work has mainly used logistic regression and a combination of decision stumps to detect vulnerable plaques. However, this is just one method and there are multiple other avenues that can be pursued in an effort to improve classification accuracy [150]. Instead of using "hard thresholding" as has been done in this work, where certain features are either present or absent, one may employ "soft thresholding" to provide a range of variation for certain features. For example, the individual TFC and NC/SFC algorithms can output the actual value associated with the logistic function probability of that features being present, rather than just a binary decision. As we know, histology and pathology is not binary, and thus soft thresholding should be pursued as a method to improve accuracy. Another method that may be explored is that of boosting [150], which would allow different weighting factor to be assigned to each of the individual features rather than equal weights as has been done in this work. The method of boosting may be particularly helping if the scores

of the VPI were to change to favor certain features more heavily. Finally, other more statistical methods, such as support vector machines [150], should also be explored. Although the objective is to identify a physical basis for a medically-related classification, statistical correlations can be used to potentially infer a physical relationship that may have been overlooked.

■ 8.1.2 Thrombus and hemorrhage

The main limitation to detecting all post-ruptured vulnerable plaques (perhaps not vulnerable by the "early" criteria), as described in Sec. 6.4.7, is the inability to always detect thrombus and intralesional hemorrhage. A separate study should be conducted to further analyze the ability to detect thrombus and hemorrhage in plaques. It is to be expected, as mentioned in Sec. 6.4.6, that thrombi are easier to detect spectroscopically than hemorrhages as they appear, by definition, on the luminal surface of the plaque rather than inside the arterial wall and thus provide a larger signal. It should be noted also that the composition of a thrombus or hemorrhage, composed of platelets, fibrin, and red blood cells, varies with the time-sensitive stage of the healing process. Therefore, it would be reasonable to expect that the particular Raman thrombus constituent spectrum extracted may not spectroscopically represent all thrombi at the various stages of the healing process.

■ 8.1.3 SFC vs. NC

Another present limitation of the described spectroscopic method is the inability to separate the contributions of NC and SFC. This is not surprising since both have very similar chemical composition, mainly dominated by lipids, and thus DRS or IFS is not picking up on differences in absorption or fluorophores present. However, as discussed in Sec. 6.4.8, there is reason to believe that SFC provide a more intense contribution to the scattering as compared to NC as the individual lipid vesicles found in foam cells would create a higher heterogeneity in the index of refraction.

Another careful *in vitro* study examining the scattering properties of foam cells would help answer the question whether SFCs can be reliably detected through scattering. The key benefit in identifying foam cells apart from NC is that the specificity of the TFC individual diagnostic algorithm could be improved. In the TFC algorithm, several thick fibrous caps were misclassified as thin as they contained an abundance of SFC that gave the false impression of a NC; if those SFCs could be identified individually, the algorithm could be modified to compensate for this effect and thus boost overall specificity of detecting vulnerable plaques.

■ 8.1.4 Raman background removal

At present, the pre-processing steps for Raman signal extraction include the removal of tissue fluorescence by means of a 6^{th} order polynomial fit. Although that method has been utilized in many different studies, by our group and others, this step may also introduce some unwanted spectral distortions of the extracted Raman spectrum. Another way to remove tissue fluorescence would be by utilizing the method of frequency shifting [145]. Namely, Raman spectra would be collected twice from the same location, using two separate excitation lines, for example 830 nm and 831 nm. Since the Raman spectra are a function of wave number relative to the excitation line, the corresponding Raman peaks will undergo a slight shift in absolute wavelength. However, the tissue fluorescence would change only minimally utilizing two very similar excitation lines. As a result, if one of the two raw spectra is subtracted from the other, the fluorescence would cancel out, leaving the difference between the Raman spectra in absolute wavelength. Through a final deconvolution step, the intended Raman spectrum could be obtained from this difference spectrum, free of tissue fluorescence. This method has the potential to remove tissue fluorescence more accurately, in a way that a 6^{th} order polynomial subtraction may not be able to compensate. Additionally, other

more advanced mathematical methods to remove the background signal [146] may be explored in future work. A more accurate correction would insure more accurate parameter extraction from Raman spectra, particularly relevant in capture critical features of vulnerability such as a thrombus or hemorrhage.

■ 8.2 Intravascular imaging

■ 8.2.1 Side-viewing probe

The studies described in this thesis have utilized a front-viewing probe to collect spectra. We have also designed side-viewing probes, capable of collecting light in a lateral geometry, a schematic of which is given in Fig. 8-1. Although our side-viewing probe prototype has been constructed and tested successfully, it has not been used clinically to date. The main difference between the side-viewing and front-viewing probe is the placement of a half-ball lens and a 45 degree mirror at the probe tip, that channels the light laterally through a sapphire window. This type of probe would be appropriate for intravascular use and its diameter can be made small enough (< 2 mm) to fit through a standard introducer sheath presented at the bottom of Fig. 8-1.

■ 8.2.2 Intravascular constraints

Even with a working side-viewing probe, there are several challenges that need to be overcome in order to demonstrate intravascular viability of MMS. First, the issue of flowing blood and absorption caused by hemoglobin would need to be addressed. One solution to this would be to use a saline flush to remove blood from the field, something which can be done via the same introducer sheath through which the probe is threaded. The second challenge will be to register the probe against the artery wall internally. In order to achieve this, perhaps an inflatable balloon mechanism could

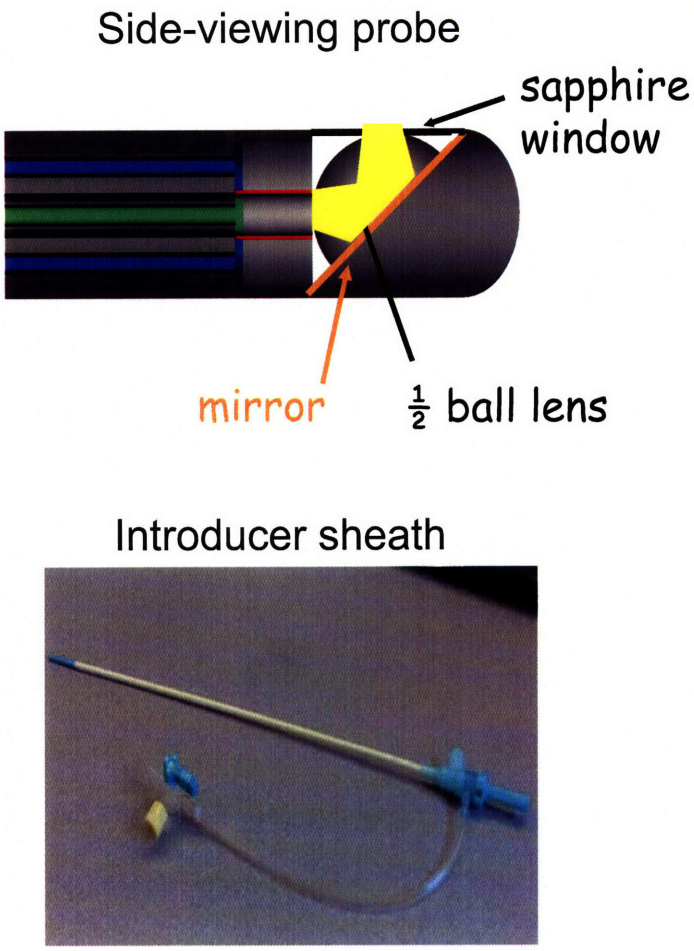

Figure 8-1. A schematic of the side-viewing probe (top) that could be introduced via sheath (bottom) for intravascular use.

be used, similar to that used for angioplasty. A collaboration with a commercial entity with more extensive experience with catheters and balloons may be very useful in this process.

■ 8.2.3 Circumferential imaging

So far, we have only demonstrated point spectroscopy with MMS. In order to provide maximum clinical information, circumferential images of the artery wall would be a great step forward. There are several challenges that need to be overcome. In order to achieve circumferential imaging, a

customized pullback and rotate mechanism would need to be designed and implemented for the side-viewing probe. This would enable the rotation of the probe for circumferential imaging as well as pullback for longitudinal advance through an artery. Another problem is the relatively long exposure time, on the order of several seconds, that is presently needed for MMS signals to exhibit an adequate SNR. The exposure time would need to be reduced and/or optimized for the different MMS modalities. For example, DRS and IFS could serve to rapidly scan through the artery and Raman could be used only in specific locations to boost sensitivity, for example, in locations where a thin fibrous cap is detected with the IFS algorithm.

■ 8.3 Microscopy techniques

Another avenue to be explored, apart from MMS, is the usage of advanced microscopy techniques. These techniques, including confocal microscopy [155], OCT [51], CARS, SHG, and TPEF [58], could be used to study *ex vivo* tissue samples and gain further insight into the morphology of atherosclerotic plaques. Of these, only OCT has been demonstrated as an intravascular technique as well. Since the axial structure of plaques is critical for vulnerability, having a method that provides more specific information about the various depths from which the signals are being generated is crucial for optimal diagnosis. In addition, several of these techniques could be joined together, as in the case of OCT together with SHG or CARS [156], and thus provide even more diagnostic information.

Appendix A

List of abbreviations

Acronym	Meaning
AA	Adventitial adipocytes
β-CC	β-carotene crystals
CAD	Coronary artery disease
CARS	Coherent anti-Stokes Raman scattering
CC	Cholesterol crystals
CCD	Charge-coupled device
CF	Collagen fibers
CLS	Classical least squares
CM	Calcium mineralization
CRLB	Cramér-Rao lower bound
CT	Computed tomography
DRS	Diffuse reflectance spectroscopy

Continued on Next Page...

Table A.1 – Continued

Acronym	Meaning
EEM	Excitation-emission matrix
EL	Elastic lamina
FC	Foam cells
FC/NC	Foam cells / necrotic core
FN	False negative
FP	False positive
FWHM	Full width at half maximum
IFS	Intrinsic fluorescence spectroscopy
IVUS	Intravascular ultrasound
IR	Infrared
LDL	Low-density lipoprotein
MCR	Multivariate curve resolution
ML	Maximum likelihood
MMS	Multimodal spectroscopy
MRI	Magnetic resonance imaging
MVU	Minimum variance unbiased
NA	Numerical aperture
NAS	Net analyte signal

Continued on Next Page...

Table A.1 – Continued

Acronym	Meaning
NC	Necrotic core
NIR	Near-infrared
NPV	Negative predictive value
OCT	Optical coherence tomography
OLS	Ordinary least squares
PCR	Principal components regression
PLS	Partial least squares
PPV	Positive predictive value
ROC	Receiver operating characteristic
SFC	Superficial foam cells
SHG	Second harmonic generation
SMC	Smooth muscle cells
SNR	Signal-to-noise ratio
TFC	Thin fibrous cap
TN	True negative
TP	True positive
TPEF	Two-photon excited fluorescence
UV	Ultraviolet

Continued on Next Page...

Table A.1 – Continued

Acronym	Meaning
VIF	Variance inflation factor
VP	Vulnerable plaque
VPI	Vulnerable plaque index

Appendix B

Classification

This appendix describes the necessary terminology and mathematical tools needed to perform classification of data. The first section defines the standard terminology, such as sensitivity, specificity, positive predictive value, and negative predictive value. The second section describes the method of logistic regression in developing classifiers. The third section describes the generation and significance of receiver operating characteristic (ROC) curves. The final section comments on a cross validation technique to insure that the classifiers generalize to prospective data.

B.1 Performance metrics

The *sensitivity* of a test is a measure of how well the classification test identifies a condition, in other words proportion of true positives of all the vulnerable plaques in the data set. The *specificity* of a test is a measure of how well the classification test identifies the negative case or the absence of a condition, in other words the proportion of true negatives of all the non-vulnerable plaques. The *positive predictive value (PPV)* is a posterior measure that specifies the proportion of data points with a positive test outcome that are correctly classified. The *negative predictive value (NPV)*, is a posterior measure that specifies the proportion of data points with a negative test outcome that are correctly classified. There terms are summarized in Fig. B-1.

Expressed mathematically, the relevant quantities can be defined as:

$$sensitivity \equiv Pr\{test\ positive \mid condition\ true\} = \frac{TP}{TP+FN} \tag{B.1}$$

$$specificity \equiv Pr\{test\ negative \mid condition\ false\} = \frac{TN}{TN+FP} \tag{B.2}$$

$$PPV \equiv Pr\{condition\ true \mid test\ positive\} = \frac{TP}{TP+FP} \tag{B.3}$$

$$NPV \equiv Pr\{condition\ false \mid test\ negative\} = \frac{TN}{TN+FN}, \tag{B.4}$$

where TP = true positives, FN = false negatives, TN = true negatives, and FP = false positives, as defined in Fig. B-1.

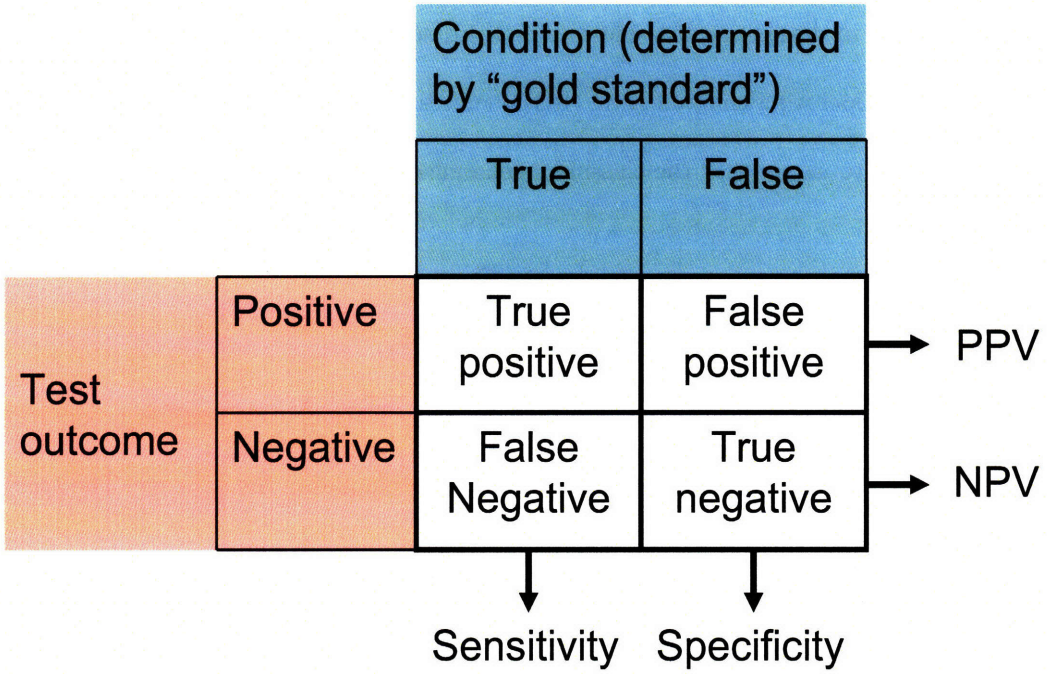

Figure B-1. Binary classifier plot that visually defines the relevant terms: sensitivity, specificity, positive predictive value (PPV) and negative predictive value (NPV).

■ B.2 Logistic regression

There are many methods to classify points in some space [150], but we shall use logistic regression, a commonly used method that relies on maximum likelihood. Logistic regression is a method for finding the optimal classification boundary between two sets of labeled points. Formally, if $\vec{x}_i = \begin{bmatrix} x_{i1} & \dots & x_{id} \end{bmatrix}^T$ is a point in d-space, and $y_i \in \{-1, +1\}$ is the binary label of this point, we wish to find the classification boundary specified by a d-dimensional vector $\vec{\theta}$ and a scalar offset θ_0 that maximizes correct classification. In our diagnostic case, lesions are specified by vectors, whose elements are spectral parameters, and the labels indicate, for example, whether or not the lesion is vulnerable according to histology.

The parameters $\vec{\theta}$ and θ_0 specify a linear classification boundary (the θ_0 parameter allows the boundary surface to lie anywhere within d-space; without this parameter, the boundary is confined to pass through the origin) such that

$$\Delta_i = \vec{x}_i^T \vec{\theta} + \theta_0 \tag{B.5}$$

gives the perpendicular distance of point $\vec{x}_i$ from the boundary. In this manner, the each point has been reduced from d-dimensions ($\vec{x}_i$) to a scalar (Δ_i). Thus, given a classification boundary, we would predict the label of point $\vec{x}_i$ to be $\hat{y}_i = \text{sign}(\Delta_i)$. In other words, a point is classified as $+1$ if it lies above the decision boundary (its projection onto $\vec{\theta}$ is positive), and as -1 if it lies below the decision boundary.

The optimal classification boundary would maximize the number of correctly-classified points: $\sum_{i=1}^{N} y_i \hat{y}_i$ (each term in the sum is $+1$ if y_i and $\hat{y}_i$ match, and -1 if they are different). However, $\hat{y}_i$ contains the sign function that has a discontinuity at 0, which in turn makes it difficult to optimize the above objective. In order to pose a tractable optimization problem, the logistic function is used

within a probabilistic context (maximum likelihood).

The effect of using the logistic function is to assign to each point $\vec{x}_i$ a smoothly-varying probability of belonging to a particular label group. Formally:

$$P(\hat{y}_i = 1|\vec{x}_i, \vec{\theta}, \theta_0) = \frac{1}{1 + e^{-\Delta_i}}, \tag{B.6}$$

where Δ_i is the same perpendicular distance from the decision boundary, as defined in Eq. (B.5). The logistic function has a sigmoidal shape that passes through 0.5 when $\Delta_i = 0$. This implies that when a point $\vec{x}_i$ is on the decision boundary, it is equally likely to have label $+1$ or -1. For points $\vec{x}_i$ for which $\Delta_i \gg 0$, the probability of having the $+1$ label is approximately 1, and for points that have $\Delta_i \ll 0$, the probability of having the $+1$ label is approximately 0. Note that a decision boundary can be placed corresponding to a different threshold probability of correctly classifying a $+1$ label; this translates to specifying $\Delta_i >$ threshold as the necessary criterion to classify a $+1$ label. Due to the symmetry of the logistic function, we can rewrite Eq. (B.6) more generally as

$$P(\hat{y}_i = y_i|\xi, \vec{\theta}, \theta_0) = \frac{1}{1 + e^{-y_i\Delta_i}}, \tag{B.7}$$

where the inclusion of the y_i term in the logistic function appropriately changes the sign in the exponent such that the expression now gives the probability of being *correctly* classified, rather than giving the probability of being classified as a particular label.

To maximize the probability of correctly classifying all the points in the test data set, we wish to find the parameters that maximize the likelihood of estimating the proper labels y_i given the

observations $\vec{x}_i$ and parameters $\vec{\theta}$ and θ_0:

$$\begin{aligned}
\vec{\theta}, \theta_0 &= \arg\max_{\vec{\theta},\theta_0} \prod_{i=1}^{N} P(\hat{y}_i = y_i | \vec{x}_i, \vec{\theta}, \theta_0) \\
&= \arg\max_{\vec{\theta},\theta_0} \ln \left(\prod_{i=1}^{N} P(\hat{y}_i = y_i | \vec{x}_i, \vec{\theta}, \theta_0) \right) \\
&= \arg\max_{\vec{\theta},\theta_0} \sum_{i=1}^{N} -\ln \left(1 + e^{-y_i \Delta_i}\right) \\
&= \arg\min_{\vec{\theta},\theta_0} \sum_{i=1}^{N} \ln \left(1 + e^{-y_i \Delta_i}\right) \qquad \text{(B.8)}
\end{aligned}$$

Equation (B.8) has a well-defined derivative and is convex, which means that a global minimum exists and can be reached in an iterative way (via gradient descent).

■ B.3 Receiver operating characteristic (ROC)

Logistic regression determines an optimal mapping, in the maximum likelihood sense, of each point to a probability of being classified with the correct label. This mapping is performed through a regression vector, $\vec{\theta}$, onto which all points are projected, and the projection is related to a probability through the logistic function, Eq. (B.6). Geometrically, a decision boundary is always orthogonal to the regression vector $\vec{\theta}$. A decision boundary can be associated with any particular threshold probability from the logistic function, not necessarily only a 50% probability, by specifying $\Delta_i >$ threshold as the classification criterion. For certain applications, one may wish to set a lower probability threshold of detecting, for example, a disease even if that comes at a cost of increasing FPs.

Each decision boundary contains an associated value of sensitivity and specificity. As the decision boundaries are changed depending on the probability threshold, so is a tradeoff between

sensitivity and specificity. In one extreme case, a decision boundary that classifies all points as positive exhibits a 100% sensitivity and 0% specificity. Conversely, a decision boundary that classifies all points as negative exhibits 0% sensitivity and 100% specificity. A receiver operating characteristic (ROC) curve represents the tradeoff between sensitivity and specificity. The ordinate axis of an ROC curve contains the sensitivity and the abscissa contains 1 – specificity.

A perfect classifier, if the two sets of points are perfectly separable, is able to achieve a 100% sensitivity and 100% specificity, corresponding to the point in the upper left corner of the ROC space. A classifier corresponding to chance, a coin toss, corresponds to the 45° line connecting points $(0, 0)$ and $(1, 1)$ in the ROC space. A classifier utilizing some useful but imperfect diagnostic information will fall in the ROC space between the perfect classifier and the chance classifier. The area under the ROC curve, out of a maximum of unity, may be used to compare the robustness of a classifier. For example, the chance classifier contains an area of 0.5 while the perfect classifier has an area of 1 since it includes the entire ROC space.

One final remark is that any ROC curve is, by definition, convex as it specifies the frontier of optimal classifiers. In other words, when working with a finite set of data, there may be certain classifiers that are suboptimal in that they give up, say, sensitivity without any gains in the specificity as compared to another classifier. Those particular points in the ROC space should not be included on the ROC frontier curve. Another way to see graphically that the ROC curve has to be convex is to realize that a classifier can be constructed from two separate classifiers (i.e. points on the ROC) through randomization. By varying the probability with which each of the two classifiers is applied, one can achieve any point in the ROC space on the segment joining the two individual classifier points.

■ B.4 Leave-one-out cross validation

A classifier can be determined that works with high accuracy on the given set of points from which it is constructed. However, a critical question is how well that classifier generalizes to prospective data, drawn from the same distribution. There are several ways of testing the generalizability of a classifier. For example, one may divide the entire data set in two, using a training set to develop a classifier and then applying it to the other, testing set. The classifier is evaluated based on its performance on the testing set and in this way the classifier is validated. However, splitting the data in two may not be appropriate for relatively small data sets, when over-fitting may be a concern. As an alternative, a common approach is to use leave-one-out cross validation. In this method, one sample is removed from the data set, a classifier is developed based on the remaining points, and then the classifier is prospectively applied to the sample taken out. This process is repeated sequentially, leaving out each data point and applying to it a classifier obtained by training on the remaining points.

Appendix C

Timeline: 308 nm UV lamp

This appendix summarizes and documents the development, testing, and problems that were encountered with the prototype 308 nm UV lamp. This lamp was initially intended to be used as a second fluorescence excitation source to replace the bulky, heavy, and expensive excimer laser (Lambda Physik, Ft. Lauderdale, FL) that was used in FastEEM instruments to provide 308 nm excitation. This lamp was developed by a start-up company (UV Solutions, Inc., Newark, NJ) in a collaborative effort and with the feedback from our laboratory. Several designs of the lamp were iterated by UV Solutions, each one improving on the previous, but it was finally concluded that, at this time, the 308 nm UV lamp is not robust enough to function on a clinical instrument. As a result, the integration of this lamp in any instrument has been discontinued, for the time being. A photograph of the most recent lamp is given in Fig. C-1. Fortunately, additional analysis indicated that the additional 308 nm fluorescence excitation source is not necessary for application in artery tissue, as described in Sec. 2.6.

The following is a timeline of the development of the 308 nm UV lamp.

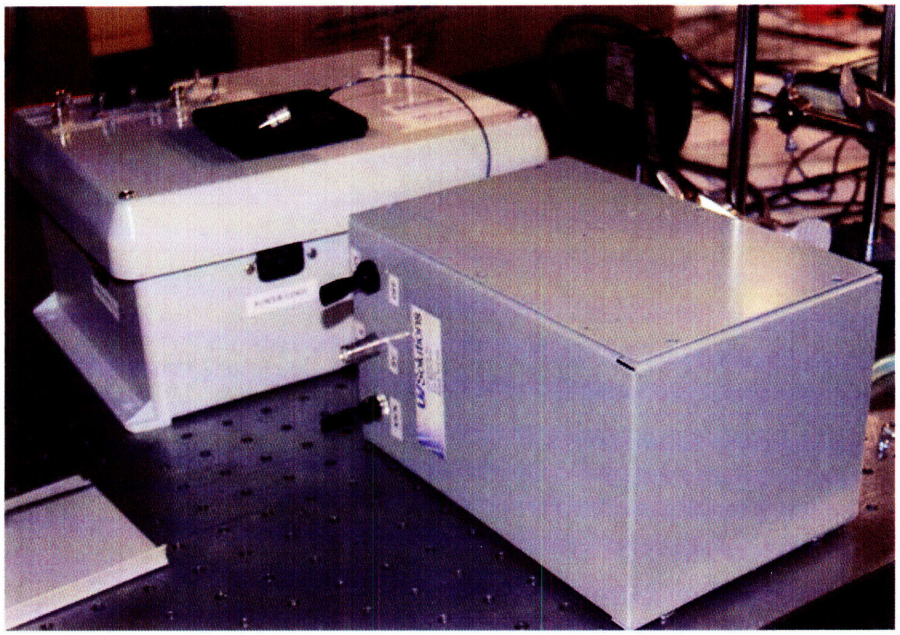

Figure C-1. Photograph of the 308 nm UV lamp by UV Solutions, Inc. The lamp consists of two units: 1) a power supply and control box, and 2) a gas chamber that produces the 308 nm emission, coupled into an optical fiber.

■ C.1 April 11, 2007 (1st iteration)

UV Solutions delivered the lamp and we used our external pump to continuously pump it. The lamp worked in continuous flow mode. When we were preparing to seal the lamp, there was a vacuum pump failure, necessitating restarting again. There was evidence of a vacuum leak in the lamp or contamination as the subsequent pump-down time was longer than anticipated, the maximum output very low, and the sealed lifetime was very short. While it worked, we tested coupling into a fiber using two lenses without much success. UV Solutions took the lamp back with them and promised to refurbish it.

■ C.2 May 18, 2007 (2nd iteration)

UV Solutions delivered the repaired lamp, which we were able to pump and seal. Then we attempted to couple light with an optimized UV grade lens but did not have much success as the output beam was diverging at a skewed angle. We broached the idea of direct fiber coupling and UV Solutions agreed that it was a good idea. We tested the lamp for a few weeks afterwards and noticed the power dropping significantly. As a result, we modified the gas connections to quick-connect as we needed to re-pump the lamp after the power drops.

■ C.3 Circa June 15, 2007

We sent back the lamp, power supply, and an FC connected fiber (20 cm long) to UV Solutions. Since between the last visit and now we had changed the connections to quick-connect type, it seemed that the inside connection between one of the valves and the body of the lamp has been broken and caused the leak. UV Solutions tried to fix the leak externally, but that was not possible since the inside tubes were also broken. In the end, UV Solutions built a new lamp and attached the fiber that we supplied to it.

■ C.4 July 13, 2007 (3rd iteration)

UV Solutions delivered the lamp that was sealed and fiber-coupled using our fiber. Initial tests were promising and adequate energies were recorded with the photodiode. However, the lamp started flickering around 7/25/07 and was not coupling any light to the MMS probe. This probe coupling problem turned out to be cause byhte FC-to-FC connector that was used. Around this time, the lamp took much longer to turn on (4 minutes needed to hold kick switch) and eventually did not even stay on unless the kick switch was held pressed down continuously.

■ C.5 September 5, 2007

We sent the power supply and the lamp back. UV Solutions was supposed to modify the power supply to allow for an external trigger pulse (to be synced with camera gate) and we also sent the lamp back since it still had the flickering problem and would not turn on unless the kick was held pressed continuously.

■ C.6 September 19, 2007 (4th iteration)

We received the lamp and power supply via courier. The lamp did not turn on at all and we felt broken pieces inside the lamp unit. After being instructed by UV Solutions to do so, we opened the lamp and saw the teflon pieces were dislodged; the lamp seemed broken. It was determined that the brakeage was the fault of the shipping courier, who came and took the lamp away, issuing some compensation to UV Solutions and destroying the lamp afterwards.

■ C.7 October 24, 2007

We sent two SMA connected fibers (1 m long) to UV Solutions so that they can build another fiber coupled lamp.

■ C.8 December 6, 2007 (5th iteration)

UV Solutions delivered a new lamp, coupled to an SMA-terminated fiber. Everything seemed to work very well that day, the lamp had high brightness and we were able to get enough energy to collect fluorescence from artery. On 12/11/07, after we moved the lamp to a different location on an optical table, it did not stay on, the problem continued on 12/12/07 during a phone conference with UV Solutions. We kept testing the lamp for a few days after, and the lamp was flickering and

did not stay on longer than 5 minutes, over a wide range of frequencies and pulse widths tested, according to instructions from UV Solutions.

■ C.9 December 18, 2007

We sent the lamp and power supply back to UV Solutions as the lamp was no longer functioning.

■ C.10 January 3, 2008 (6th iteration)

UV Solutions shipped to us the lamp and power supply, saying they only modified the power supply, better matching the driver circuit to the lamp. We tested the lamp for a few days. The lamp would stay on, but we noticed a lot more radio-frequency output than before, manifesting itself in much more noise recorded with the photodiode, to the extent that we were not able to measure the power output with the lamp in the presence of this noise. Visually, the light output from the fiber (and when connected to a probe) was much less intense than we remembered from 12/06/07 testing. Ignoring our inability to measure the energy, we repeated the same experiment from 12/06/07 to measure fluorescence through the probe with our camera. We were not only unable to see the fluorescence but not even the 308 nm laser line. This confirmed the suspicion that the energy output was orders of magnitude smaller than on 12/06/07 and that fluorescence could not be excited with the lamp in its present state.

■ C.11 March 25, 2008

We send the non-functioning lamp back to UV Solutions.

Bibliography

[1] W. Rosamond, K. Flegal, G. Friday, K. Furie, A. Go, K. Greenlund, N. Haase, M. Ho, V. Howard, B. Kissela, S. Kittner, D. Lloyd-Jones, M. McDermott, J. Meigs, C. Moy, G. Nichol, C. J. O'Donnell, V. Roger, J. Rumsfeld, P. Sorlie, J. Steinberger, T. Thom, S. Wasserthiel-Smoller, and Y. L. Hong, "Heart disease and stroke statistics - 2007 update - a report from the American Heart Association Statistics Committee and Stroke Statistics Subcommittee," *Circulation* **115**(5): E69–E171 (2007).

[2] C. J. L. Murray and A. D. Lopez, "Evidence-based health policy - lessons from the global burden of disease study," *Science* **274**(5288): 740–743 (1996).

[3] R. S. Cotran, V. Kumar, T. Collins, and S. L. Robbins, *Robbins pathologic basis of disease* (Saunders, Philadelphia, 1999).

[4] P. Libby, "Current concepts of the pathogenesis of the acute coronary syndromes," *Circulation* **104**(3): 365–372 (2001).

[5] N. V. Guevara, K. H. Chen, and L. Chan, "Apoptosis in atherosclerosis: pathological and pharmacological implications," *Pharmacological Research* **44**(2): 59–71 (2001).

[6] P. Libby, "Inflammation in atherosclerosis," *Nature* **420**(6917): 868–874 (2002).

[7] A. Schmermund, S. Mohlenkamp, and R. Erbel, "The latest on the calcium story," *American Journal of Cardiology* **90**(10C): 12L–14L (2002).

[8] R. Virmani, A. P. Burke, A. Farb, and F. D. Kolodgie, "Pathology of the unstable plaque," *Progress in Cardiovascular Diseases* **44**(5): 349–356 (2002).

[9] M. Rollo, T. Tartaglione, A. Pedicelli, and C. Settecasi, "Atherosclerosis of carotid and intracranial arteries," *Rays* **26**(4): 247–268 (2001).

[10] R. Virmani, A. P. Burke, F. D. Kolodgie, and A. Farb, "Vulnerable plaque: The pathology of unstable coronary lesions," *Journal of Interventional Cardiology* **15**(6): 439–446 (2002).

[11] R. T. Lee and P. Libby, "The unstable atheroma," *Arteriosclerosis, Thrombosis, and Vascular Biology* **17**(10): 1859–1867 (1997).

[12] I. J. Kullo, W. D. Edwards, and R. S. Schwartz, "Vulnerable plaque: Pathobiology and clinical implications," *Annals of Internal Medicine* **129**(12): 1050–1060 (1998).

[13] M. Naghavi, P. Libby, E. Falk, S. W. Casscells, S. Litovsky, J. Rumberger, J. J. Badimon, C. Stefanadis, P. Moreno, G. Pasterkamp, Z. Fayad, P. H. Stone, S. Waxman, P. Raggi, M. Madjid, A. Zarrabi, A. Burke, C. Yuan, P. J. Fitzgerald, D. S. Siscovick, C. L. de Korte, M. Aikawa, K. E. Juhani Airaksinen, G. Assmann, C. R. Becker, J. H. Chesebro, A. Farb, Z. S. Galis, C. Jackson, I. K. Jang, W. Koenig, R. A. Lodder, K. March, J. Demirovic, M. Navab, S. G. Priori, M. D. Rekhter, R. Bahr, S. M. Grundy, R. Mehran, A. Colombo, E. Boerwinkle, C. Ballantyne, J. Insull, W., R. S. Schwartz, R. Vogel, P. W. Serruys, G. K. Hansson, D. P. Faxon, S. Kaul, H. Drexler, P. Greenland, J. E. Muller, R. Virmani, P. M. Ridker, D. P. Zipes,

P. K. Shah, and J. T. Willerson, "From vulnerable plaque to vulnerable patient: A call for new definitions and risk assessment strategies: Part I," *Circulation* **108**(14): 1664–1672 (2003).

[14] M. Naghavi, P. Libby, E. Falk, S. W. Casscells, S. Litovsky, J. Rumberger, J. J. Badimon, C. Stefanadis, P. Moreno, G. Pasterkamp, Z. Fayad, P. H. Stone, S. Waxman, P. Raggi, M. Madjid, A. Zarrabi, A. Burke, C. Yuan, P. J. Fitzgerald, D. S. Siscovick, C. L. de Korte, M. Aikawa, K. E. Airaksinen, G. Assmann, C. R. Becker, J. H. Chesebro, A. Farb, Z. S. Galis, C. Jackson, I. K. Jang, W. Koenig, R. A. Lodder, K. March, J. Demirovic, M. Navab, S. G. Priori, M. D. Rekhter, R. Bahr, S. M. Grundy, R. Mehran, A. Colombo, E. Boerwinkle, C. Ballantyne, J. Insull, W., R. S. Schwartz, R. Vogel, P. W. Serruys, G. K. Hansson, D. P. Faxon, S. Kaul, H. Drexler, P. Greenland, J. E. Muller, R. Virmani, P. M. Ridker, D. P. Zipes, P. K. Shah, and J. T. Willerson, "From vulnerable plaque to vulnerable patient: A call for new definitions and risk assessment strategies: Part II," *Circulation* **108**(15): 1772–1778 (2003).

[15] F. D. Kolodgie, H. K. Gold, A. P. Burke, D. R. Fowler, H. S. Kruth, D. K. Weber, A. Farb, L. J. Guerrero, M. Hayase, R. Kutys, J. Narula, A. V. Finn, and R. Virmani, "Intraplaque hemorrhage and progression of coronary atheroma," *New England Journal of Medicine* **349**(24): 2316–2325 (2003).

[16] R. Virmani, F. D. Kolodgie, A. P. Burke, A. V. Finn, H. K. Gold, T. N. Tulenko, S. P. Wrenn, and J. Narula, "Atherosclerotic plaque progression and vulnerability to rupture - angiogenesis as a source of intraplaque hemorrhage," *Arteriosclerosis, Thrombosis, and Vascular Biology* **25**(10): 2054–2061 (2005).

[17] R. Virmani, F. D. Kolodgie, A. P. Burke, A. Farb, and S. M. Schwartz, "Lessons from sudden coronary death: A comprehensive morphological classification scheme for atherosclerotic lesions," *Arteriosclerosis, Thrombosis, and Vascular Biology* **20**(5): 1262–1275 (2000).

[18] M. J. Kern and B. Meier, "Evaluation of the culprit plaque and the physiological significance of coronary atherosclerotic narrowings," *Circulation* **103**(25): 3142–3149 (2001).

[19] G. S. Mintz, J. J. Popma, A. D. Pichard, K. M. Kent, L. F. Satler, Y. C. Chuang, C. J. Ditrano, and M. B. Leon, "Patterns of calcification in coronary artery disease. A statistical analysis of intravascular ultrasound and coronary angiography in 1155 lesions," *Circulation* **91**(7): 1959–1965 (1995).

[20] E. Topol and S. Nissen, "Our preoccupation with coronary luminology. The dissociation between clinical and angiographic findings in ischemic heart disease," *Circulation* **92**(8): 2333–2314 (1995).

[21] E. Tuczu, B. Berkalp, A. DeFranco, S. Ellis, M. Goormastic, P. Whitlow, I. Franco, R. Raymond, and S. Nissen, "The dilemma of diagnosing coronary classification: Angiography versus intravascular ultrasound," *Journal of the American College of Cardiology* **27**(4): 832–838 (1996).

[22] S. Vallabhajosula and V. Fuster, "Atherosclerosis: Imaging techniques and the evolving role of nuclear medicine," *Journal of Nuclear Medicine* **38**(11): 1788–1796 (1997).

[23] T. Saito, H. Date, I. Taniguchi, S. Nakamura, H. Oka, Y. Mizuno, K. Noda, S. Yamashita, S. Oshima, and H. Yasue, "Angiographic evaluation of culprit lesions in acute coronary syn-

drome: Relation to the original site on previous coronary angiography," *Japanese Circulation Journal* **62**(5): 359–363 (1998).

[24] C. J. White, S. R. Ramee, T. J. Collins, A. E. Escobar, A. Karsan, D. Shaw, S. P. Jain, T. A. Bass, R. R. Heuser, P. S. Teirstein, R. Bonan, P. D. Walter, and R. W. Smalling, "Coronary thrombi increase PTCA risk. Angioscopy as a clinical tool," *Circulation* **93**(2): 253–258 (1996).

[25] M. Asakura, Y. Ueda, O. Yamaguchi, T. Adachi, A. Hirayama, M. Hori, and K. Kodama, "Extensive development of vulnerable plaques as a pan-coronary process in patients with myocardial infarction: An angioscopic study," *Journal of the American College of Cardiology* **37**(5): 1284–1288 (2001).

[26] S. Feld, M. Ganim, and E. Carell, "Comparison of angioscopy, intravascular ultrasound imaging and quantitative coronary angiography in predicting clinical outcome after coronary intervention in high risk patients," *Journal of the American College of Cardiology* **28**(1): 97–105 (1996).

[27] T. Thieme, K. Wernecke, R. Meyer, E. Brandenstein, D. Habedank, A. Hinz, S. Felix, G. Baumann, and F. Kleber, "Angioscopic evaluation of atherosclerotic plaques: Validation by histomorphologic analysis and association with stable and unstable coronary syndromes," *Journal of the American College of Cardiology* **28**(1): 1–6 (1996).

[28] R. Peters, W. Wouter, M. Javenith, H. Rijsterborgh, A. van der Wal, and C. Visser, "Histopathologic validation of intracoronary ultrasound imaging." *Journal of the American Society of Echocardiography* **7**: 230–241 (1994).

[29] S. Nissen, A. DeFranco, E. Tuzco, and D. Moliterno, "Coronary intravascular ultrasound: Diagnostic and interventional applications," *Coronary Artery Disease* **6**(5): 355–367 (1995).

[30] R. Shekhar, R. Cothren, D. Vince, S. Chandra, J. Thomas, and J. Cornhill, "Three-dimensional segmentation of luminal and adventitial borders in serial intravascular ultrasound images," *Computerized Medical Imaging and Graphics* **23**(6): 299–309 (1999).

[31] M.-K. Hong, S.-W. Park, G. Mintz, N.-H. Lee, C. Lee, J.-J. Kim, and S.-J. Park, "Intravascular ultrasonic predictors of angiographic restenosis after long coronary stenting," *American Journal of Cardiology* **85**(4): 441–445 (2000).

[32] R. Mehran, G. Dangas, G. Mintz, A. Lansky, A. Pichard, L. Satler, K. Kent, G. Stone, and M. Leon, "Atherosclerotic plaque burden and CK-MB enzyme elevation after coronary interventions: Intravascular ultrasound study of 2256 patients," *Circulation* **101**(6): 604–610 (2000).

[33] P. Schoenhagen and S. Nissen, "Understanding coronary artery disease: Tomographic imaging with intravascular ultrasound," *Heart* **88**(1): 91–96 (2002).

[34] T. Romer, J. Brennan, G. Puppels, A. Zwinderman, S. van Duinen, A. van der Laarse, A. van der Steen, N. Born, and A. Bruschke, "Intravascular ultrasound combined with Raman spectroscopy to localize and quantify cholesterol calcium salts in atherosclerotic coronary arteries," *Atherosclerosis, Thrombosis, and Vascular Biology* **20**(2): 478–483 (2000).

[35] I. K. Jang, B. E. Bouma, D. H. Kang, S. J. Park, S. W. Park, K. B. Seung, K. B. Choi, M. Shishkov, K. Schlendorf, E. Pomerantsev, S. L. Houser, H. T. Aretz, and G. J. Tearney, "Visualization of coronary atherosclerotic plaques in patients using optical coherence

tomography: Comparison with intravascular ultrasound," *Journal of the American College of Cardiology* **39**(4): 604–609 (2002).

[36] W. Casscells, B. Hathorn, M. David, T. Krabach, W. K. Vaughn, H. A. McAllister, G. Bearman, and J. T. Willerson, "Thermal detection of cellular infiltrates in living atherosclerotic plaques: Possible implications for plaque rupture and thrombosis," *Lancet* **347**(9013): 1447–1451 (1996).

[37] C. Stefanadis, L. Diamantopoulos, C. Vlachopoulos, E. Tsiamis, J. Dernellis, K. Toutouzas, E. Stefandi, and P. Toutouzas, "Thermal heterogeneity within human atherosclerotic coronary arteries detected *in vivo*: A new method of detection by application of a special thermography catheter," *Circulation* **99**(15): 1965–1971 (1999).

[38] T. Hatsukami, R. Ross, N. Polissar, and C. Yuan, "Visualization of fibrous cap thickness and rupture in human atherosclerotic carotid plaque *in vivo* with high-resolution magnetic resonance imaging," *Circulation* **102**(9): 959–964 (2000).

[39] J. M. Serfaty, L. Chaabane, A. Tabib, J. M. Chevallier, A. Briguet, and P. C. Douek, "Atherosclerotic plaques: Classification and characterization with T2-weighted high-spatial-resolution MR imaging - an *in vitro* study," *Radiology* **219**(2): 403–410 (2001).

[40] R. E. Murphy, A. R. Moody, P. S. Morgan, A. L. Martel, G. S. Delay, S. Allder, S. T. MacSweeney, W. G. Tennant, J. Gladman, J. Lowe, and B. J. Hunt, "Prevalence of complicated carotid atheroma as detected by magnetic resonance direct thrombus imaging in patients with suspected carotid artery stenosis and previous acute cerebral ischemia," *Circulation* **107**(24): 3053–3058 (2003).

[41] N. Altaf, L. Daniels, P. S. Morgan, D. Auer, S. T. MacSweeney, A. R. Moody, and J. R. Gladman, "Detection of intraplaque hemorrhage by magnetic resonance imaging in symptomatic patients with mild to moderate carotid stenosis predicts recurrent neurological events," *Journal of Vascular Surgery* **47**(2): 337–342 (2008).

[42] T. Saam, H. R. Underhill, B. C. Chu, N. Takaya, J. M. Cai, N. L. Polissar, C. Yuan, and T. S. Hatsukami, "Prevalence of American Heart Association type VI carotid atherosclerotic lesions identified by magnetic resonance imaging for different levels of stenosis as measured by duplex ultrasound," *Journal of the American College of Cardiology* **51**(10): 1014–1021 (2008).

[43] M. Regenfus, D. Ropers, S. Achenbach, C. Schlundt, W. Kessler, G. Laub, W. Moshage, and W. G. Daniel, "Comparison of contrast-enhanced breath-hold and free-breathing respiratory-gated imaging in three-dimensional magnetic resonance coronary angiography," *American Journal of Cardiology* **90**(7): 725–730 (2002).

[44] J. Post, A. van Rossum, M. Hofman, J. Valk, and C. Visser, "Protocol for two-dimensional resonance coronary angiography studied in three-dimensional magnetic resonance data sets," *American Heart Journal* **130**(1): 167–173 (1995).

[45] W. J. Rogers, J. W. Prichard, Y. L. Hu, P. R. Olson, D. H. Benckart, C. M. Kramer, D. A. Vido, and N. Reichek, "Characterization of signal properties in atherosclerotic plaque components by intravascular MRI," *Arteriosclerosis, Thrombosis, and Vascular Biology* **20**(7): 1824–1830 (2000).

[46] S. G. Worthley, G. Helft, V. Fuster, Z. A. Fayad, M. Shinnar, L. A. Minkoff, C. Schechter, J. T. Fallon, and J. J. Badimon, "A novel nonobstructive intravascular MRI coil: *In vivo*

imaging of experimental atherosclerosis," *Arteriosclerosis, Thrombosis, and Vascular Biology* **23**(2): 346–350 (2003).

[47] S. Achenbach and W. G. Daniel, "Imaging of coronary atherosclerosis using computed tomography: Current status and future directions," *Current Atherosclerosis Reports* **6**(3): 213–218 (2004).

[48] A. Schmermund and R. Erbel, "Unstable coronary plaque and its relation to coronary calcium," *Circulation* **104**(14): 1682–1687 (2001).

[49] S. Rich and V. V. McLaughlin, "Detection of subclinical cardiovascular disease: The emerging role of electron beam computed tomography," *Preventive Medicine* **34**(1): 1–10 (2002).

[50] H. P. Salazar and P. Raggi, "Usefulness of electron-beam computed tomography," *American Journal of Cardiology* **89**(4A): 17B–22B (2002).

[51] G. J. Tearney, I. K. Jang, and B. E. Bouma, "Optical coherence tomography for imaging the vulnerable plaque," *Journal of Biomedical Optics* **11**(2): 021002 (2006).

[52] N. A. Patel, D. L. Stamper, and M. E. Brezinski, "Review of the ability of optical coherence tomography to characterize plaque, including a comparison with intravascular ultrasound," *Cardiovascular and Interventional Radiology* **28**(1): 1–9 (2005).

[53] I. K. Jang, G. J. Tearney, B. MacNeill, M. Takano, F. Moselewski, N. Iftima, M. Shishkov, S. Houser, H. T. Aretz, E. F. Halpern, and B. E. Bouma, "*In vivo* characterization of coronary atherosclerotic plaque by use of optical coherence tomography," *Circulation* **111**(12): 1551–1555 (2005).

[54] H. Yabushita, B. E. Bouma, S. L. Houser, H. T. Aretz, I. K. Jang, K. H. Schlendorf, C. R. Kauffman, M. Shishkov, D. H. Kang, E. F. Halpern, and G. J. Tearney, "Characterization of human atherosclerosis by optical coherence tomography," *Circulation* **106**(13): 1640–1645 (2002).

[55] G. J. Tearney, H. Yabushita, S. L. Houser, H. T. Aretz, I. K. Jang, K. H. Schlendorf, C. R. Kauffman, M. Shishkov, E. F. Halpern, and B. E. Bouma, "Quantification of macrophage content in atherosclerotic plaques by optical coherence tomography," *Circulation* **107**(1): 113–119 (2003).

[56] B. D. MacNeill, I. K. Jang, B. E. Bouma, N. Iftimia, M. Takano, H. Yabushita, M. Shishkov, C. R. Kauffman, S. L. Houser, H. T. Aretz, D. DeJoseph, E. F. Halpern, and G. J. Tearney, "Focal and multi-focal plaque macrophage distributions in patients with acute and stable presentations of coronary artery disease," *Journal of the American College of Cardiology* **44**(5): 972–979 (2004).

[57] M. B. Lilledahl, O. A. Haugen, C. D. Davies, and L. O. Svaasand, "Characterization of vulnerable plaques by multiphoton microscopy," *Journal of Biomedical Optics* **12**(4): 044005 (2007).

[58] T. T. Le, I. M. Langohr, M. J. Locker, M. Sturek, and J. X. Cheng, "Label-free molecular imaging of atherosclerotic lesions using multimodal nonlinear optical microscopy," *Journal of Biomedical Optics* **12**(5): 054007 (2007).

[59] P. R. Moreno and J. E. Muller, "Detection of high-risk atherosclerotic coronary plaques by intravascular spectroscopy," *Journal of Interventional Cardiology* **16**(3): 243–252 (2003).

[60] J. Wang, Y. J. Geng, B. Guo, T. Klima, B. N. Lal, J. T. Willerson, and W. Casscells, "Near-infrared spectroscopic characterization of human advanced atherosclerotic plaques," *Journal of the American College of Cardiology* **39**(8): 1305–1313 (2002).

[61] P. R. Moreno, R. A. Lodder, K. R. Purushothaman, W. E. Charash, W. N. O'Connor, and J. E. Muller, "Detection of lipid pool, thin fibrous cap, and inflammatory cells in human aortic atherosclerotic plaques by near-infrared spectroscopy," *Circulation* **105**(8): 923–927 (2002).

[62] B. J. Feder, "Scanner to find fatty deposits in vessels is approved," *The New York Times* (April 26): Business p.3 (2008).

[63] B. Ye and G. S. Abela, "Beta-carotene enhances plaque detection by fluorescence attenuation in an atherosclerotic rabbit model," *Lasers in Surgery and Medicine* **13**(4): 393–404 (1993).

[64] G. O. Angheloiu, J. T. Arendt, M. G. Muller, A. S. Haka, I. Georgakoudi, J. T. Motz, O. R. Scepanovic, B. D. Kuban, J. Myles, F. Miller, E. A. Podrez, M. Fitzmaurice, J. R. Kramer, and M. S. Feld, "Intrinsic fluorescence and diffuse reflectance spectroscopy identify superficial foam cells in coronary plaques prone to erosion," *Arteriosclerosis, Thrombosis, and Vascular Biology* **26**(7): 1594–1600 (2006).

[65] M. B. Lilledahl, O. A. Haugen, M. Barkost, and L. O. Svaasand, "Reflection spectroscopy of atherosclerotic plaque," *Journal of Biomedical Optics* **11**(2): 021005 (2006).

[66] G. Zonios, L. T. Perelman, V. M. Backman, R. Manoharan, M. Fitzmaurice, J. Van Dam, and M. S. Feld, "Diffuse reflectance spectroscopy of human adenomatous colon polyps *in vivo*," *Applied Optics* **38**(31): 6628–6637 (1999).

[67] T. J. Farrell, M. S. Patterson, and B. Wilson, "A diffusion-theory model of spatially resolved, steady-state diffuse reflectance for the noninvasive determination of tissue optical-properties *in vivo*," *Medical Physics* **19**(4): 879–888 (1992).

[68] A. J. Welch and M. J. C. van Gemert, *Optical-thermal response of laser-irradiated tissue*, Lasers, Photonics, and Electro-optics (Plenum Press, New York, 1995).

[69] M. Fitzmaurice, J. Bordagaray, G. Engelmann, R. Richards-Kortum, T. Kolubayev, M. Feld, N. Ratliff, and J. Kramer, "Argon ion laser-excited autofluorescence in normal and atherosclerotic aorta and coronary arteries: Morphologic studies," *American Heart Journal* **118**(5): 1028–1038 (1989).

[70] K. Arakawa, K. Isoda, T. Ito, K. Nakajima, T. Shibuya, and F. Ohsuzu, "Fluorescence analysis of biochemical constituents identifies atherosclerotic plaque with a thin fibrous cap," *Arteriosclerosis, Thrombosis, and Vascular Biology* **22**(6): 1002–1007 (2002).

[71] R. Richards-Kortum, R. Rava, M. Fitzmaurice, J. Kramer, and M. Feld, "476 nm excited laser-induced fluorescence spectroscopy of human coronary arteries," *American Heart Journal* **122**(4): 1141–1150 (1991).

[72] L. Deckelbaum, J. Scott, M. Stetz, K. O'Brien, and G. Baker, "Detection of calcified atherosclerotic plaque by laser-induced plasma emission," *Lasers in Surgery and Medicine* **12**(1): 18–24 (1992).

[73] A. Christov, R. M. Korol, E. B. Dai, L. Y. Liu, H. Y. Guan, M. A. Bernards, P. B. Cavers, D. Susko, and A. Lucas, "*In vivo* optical analysis of quantitative changes in collagen and elastin during arterial remodeling," *Photochemistry and Photobiology* **81**(2): 457–466 (2005).

[74] L. Marcu, W. Grundfest, and J.-M. Maarek, "Photobleaching of arterial fluorescent compounds: Characterization of elastin, collagen, and cholesterol time-resolved spectra during prolonged ultraviolet irradiation." *Photochemistry and Photobiology* **69**(6): 713–721 (1999).

[75] J.-M. Maarek, L. Marcu, W. Snyder, and W. Grundfest, "Time-resolved spectra of arterial fluorescent compounds: Reconstruction with the Laguerre expansion technique," *Photochemistry and Photobiology* **71**(2): 178–187 (2000).

[76] L. Marcu, M. C. Fishbein, J. M. I. Maarek, and W. S. Grundfest, "Discrimination of human coronary artery atherosclerotic lipid-rich lesions by time-resolved laser-induced fluorescence spectroscopy," *Arteriosclerosis, Thrombosis, and Vascular Biology* **21**(7): 1244–1250 (2001).

[77] A. Christov, E. Dai, M. Drangova, L. Y. Liu, G. S. Abela, P. Nash, G. McFadden, and A. Lucas, "Optical detection of triggered atherosclerotic plaque disruption by fluorescence emission analysis," *Photochemistry and Photobiology* **72**(2): 242–252 (2000).

[78] L. Marcu, Q. Y. Fang, J. A. Jo, T. Papaioannou, A. Dorafshar, T. Reil, J. H. Qiao, J. D. Baker, J. A. Freischlag, and M. C. Fishbein, "*In vivo* detection of macrophages in a rabbit atherosclerotic model by time-resolved laser-induced fluorescence spectroscopy," *Atherosclerosis* **181**(2): 295–303 (2005).

[79] J. Wu, M. S. Feld, and R. P. Rava, "Analytical model for extracting intrinsic fluorescence in turbid media," *Applied Optics* **32**(19): 3585–3595 (1993).

[80] Q. G. Zhang, M. G. Muller, J. Wu, and M. S. Feld, "Turbidity-free fluorescence spectroscopy of biological tissue," *Optics Letters* **25**(19): 1451–1453 (2000).

[81] I. Georgakoudi, B. C. Jacobson, J. Van Dam, V. Backman, M. B. Wallace, M. G. Muller, Q. Zhang, K. Badizadegan, D. Sun, G. A. Thomas, L. T. Perelman, and M. S. Feld, "Fluorescence, reflectance, and light-scattering spectroscopy for evaluating dysplasia in patients with Barrett's esophagus," *Gastroenterology* **120**(7): 1620–1629 (2001).

[82] I. Georgakoudi, E. E. Sheets, M. G. Muller, V. Backman, C. P. Crum, K. Badizadegan, R. R. Dasari, and M. S. Feld, "Trimodal spectroscopy for the detection and characterization of cervical precancers *in vivo*," *American Journal of Obstetrics and Gynecology* **186**(3): 374–382 (2002).

[83] A. Mahadevan-Jansen and R. Richards-Kortum, "Raman spectroscopy for the detection of cancers and precancers," *Journal of Biomedical Optics* **1**(1): 31–70 (1996).

[84] E. B. Hanlon, R. Manoharan, T. W. Koo, K. E. Shafer, J. T. Motz, M. Fitzmaurice, J. R. Kramer, I. Itzkan, R. R. Dasari, and M. S. Feld, "Prospects for *in vivo* Raman spectroscopy," *Physics in Medicine and Biology* **45**(2): R1–R59 (2000).

[85] H. P. Buschman, G. Deinum, J. T. Motz, M. Fitzmaurice, J. R. Kramer, A. van der Laarse, A. V. Bruschke, and M. S. Feld, "Raman microspectroscopy of human coronary atherosclerosis: Biochemical assessment of cellular and extracellular morphologic structures in situ," *Cardiovascular Pathology* **10**(2): 69–82 (2001).

[86] H. P. Buschman, J. T. Motz, G. Deinum, T. J. Romer, M. Fitzmaurice, J. R. Kramer, A. van der Laarse, A. V. Bruschke, and M. S. Feld, "Diagnosis of human coronary atherosclerosis by morphology-based Raman spectroscopy," *Cardiovascular Pathology* **10**(2): 59–68 (2001).

[87] J. T. Motz, M. Hunter, L. H. Galindo, J. A. Gardecki, J. R. Kramer, R. R. Dasari, and M. S. Feld, "Optical fiber probe for biomedical Raman spectroscopy," *Applied Optics* **43**(3): 542–554 (2004).

[88] J. T. Motz, S. J. Gandhi, O. R. Scepanovic, A. S. Haka, J. R. Kramer, R. R. Dasari, and M. S. Feld, "Real-time Raman system for *in vivo* disease diagnosis," *Journal of Biomedical Optics* **10**(3): 031113 (2005).

[89] J. T. Motz, M. Fitzmaurice, A. Miller, S. J. Gandhi, A. S. Haka, L. H. Galindo, R. R. Dasari, J. R. Kramer, and M. S. Feld, "*In vivo* Raman spectral pathology of human atherosclerosis and vulnerable plaque," *Journal of Biomedical Optics* **11**(2): 021003 (2006).

[90] M. Keijzer, R. R. Richards-Kortum, S. L. Jacques, and M. S. Feld, "Fluorescence spectroscopy of turbid media - autofluorescence of the human aorta," *Applied Optics* **28**(20): 4286–4292 (1989).

[91] I. Gueorguieva, L. Aarons, K. Ogungbenro, K. M. Jorga, T. Rodgers, and M. Rowland, "Optimal design for multivariate response pharmacokinetic models," *Journal of Pharmacokinetics and Pharmacodynamics* **33**(2): 97–124 (2006).

[92] M. R. Riley, M. A. Arnold, D. W. Murhammer, E. L. Walls, and N. DelaCruz, "Adaptive calibration scheme for quantification of nutrients and byproducts in insect cell bioreactors by near-infrared spectroscopy," *Biotechnology Progress* **14**(3): 527–533 (1998).

[93] D. A. Benaron, "The future of cancer imaging," *Cancer and Metastasis Reviews* **21**(1): 45–78 (2002).

[94] A. S. Haka, Z. Volynskaya, J. A. Gardecki, J. Nazemi, J. Lyons, D. Hicks, M. Fitzmaurice, R. R. Dasari, J. P. Crowe, and M. S. Feld, "*In vivo* margin assessment during partial mastectomy breast surgery using Raman spectroscopy," *Cancer Research* **66**(6): 3317–3322 (2006).

[95] I. J. Bigio, S. G. Bown, G. Briggs, C. Kelley, S. Lakhani, D. Pickard, P. M. Ripley, I. G. Rose, and C. Saunders, "Diagnosis of breast cancer using elastic-scattering spectroscopy: Preliminary clinical results," *Journal of Biomedical Optics* **5**(2): 221–228 (2000).

[96] G. M. Palmer, C. F. Zhu, T. M. Breslin, F. S. Xu, K. W. Gilchrist, and N. Ramanujam, "Monte Carlo-based inverse model for calculating tissue optical properties. Part II: Application to breast cancer diagnosis," *Applied Optics* **45**(5): 1072–1078 (2006).

[97] H. Kaiser, "Foundations for the critical discussion of analytical methods," *Spectrochimica Acta Part B: Atomic Spectroscopy* **33**(9): 551–576 (1978).

[98] A. C. Olivieri, N. K. M. Faber, J. Ferre, R. Boque, J. H. Kalivas, and H. Mark, "Uncertainty estimation and figures of merit for multivariate calibration," *Pure and Applied Chemistry* **78**(3): 633–661 (2006).

[99] H. Martens, *Multivariate Calibration* (John Wiley & Sons, 1989).

[100] K. E. Shafer-Peltier, A. S. Haka, M. Fitzmaurice, J. Crowe, J. Myles, R. R. Dasari, and M. S. Feld, "Raman microspectroscopic model of human breast tissue: Implications for breast cancer diagnosis *in vivo*," *Journal of Raman Spectroscopy* **33**(7): 552–563 (2002).

[101] A. Lorber, "Error propagation and figures of merit for quantification by solving matrix equations," *Analytical Chemistry* **58**(6): 1167–1172 (1986).

[102] A. Lorber, K. Faber, and B. R. Kowalski, "Net analyte signal calculation in multivariate calibration," *Analytical Chemistry* **69**(8): 1620–1626 (1997).

[103] P. R. Bevington and D. K. Robinson, *Data reduction and error analysis for the physical sciences* (McGraw-Hill, Boston, 2003).

[104] A. Lorber and B. R. Kowalski, "Estimation of prediction error for multivariate calibration," *Journal of Chemometrics* **2**(67): 93–109 (1988).

[105] K. Faber and B. R. Kowalski, "Propagation of measurement errors for the validation of predictions obtained by principal component regression and partial least squares," *Journal of Chemometrics* **11**(3): 181–238 (1997).

[106] D. M. Haaland and D. K. Melgaard, "New prediction-augmented classical least-squares (PACLS) methods: Application to unmodeled interferents," *Applied Spectroscopy* **54**(9): 1303–1312 (2000).

[107] B. Nadler and R. R. Coifman, "The prediction error in CLS and PLS: The importance of feature selection prior to multivariate calibration," *Journal of Chemometrics* **19**(2): 107–118 (2005).

[108] U. Utzinger and R. R. Richards-Kortum, "Fiber optic probes for biomedical optical spectroscopy," *Journal of Biomedical Optics* **8**(1): 121–147 (2003).

[109] R. A. Zangaro, L. Silveira, R. Manoharan, G. Zonios, I. Itzkan, R. R. Dasari, J. VanDam, and M. S. Feld, "Rapid multiexcitation fluorescence spectroscopy system for *in vivo* tissue diagnosis," *Applied Optics* **35**(25): 5211–5219 (1996).

[110] M. G. Muller, A. Wax, I. Georgakoudi, R. R. Dasari, and M. S. Feld, "A reflectance spectrofluorimeter for real-time spectral diagnosis of disease," *Review of Scientific Instruments* **73**(11): 3933–3937 (2002).

[111] J. W. Tunnell, A. E. Desjardins, L. Galindo, I. Georgakoudi, S. A. McGee, J. Mirkovic, M. G. Mueller, J. Nazemi, F. T. Nguyen, A. Wax, Q. G. Zhang, R. R. Dasari, and M. S. Feld, "Instrumentation for multi-modal spectroscopic diagnosis of epithelial dysplasia," *Technology in Cancer Research and Treatment* **2**(6): 505–514 (2003).

[112] R. Cothren, G. Hayes, J. R. Kramer, B. Sacks, C. Kittrell, and M. S. Feld, "A multifiber catheter with an optical shield for laser angiosurgery," *Lasers in the Life Sciences* **1**(1) (1986).

[113] M. G. Muller, T. A. Valdez, I. Georgakoudi, V. Backman, C. Fuentes, S. Kabani, N. Laver, Z. Wang, C. W. Boone, R. R. Dasari, S. M. Shapshay, and M. S. Feld, "Spectroscopic detection and evaluation of morphologic and biochemical changes in early human oral carcinoma," *Cancer* **97**(7): 1681–1692 (2003).

[114] S. Koljenovic, T. C. B. Schut, R. Wolthuis, B. de Jong, L. Santos, P. J. Caspers, J. M. Kros, and G. J. Puppels, "Tissue characterization using high wave number Raman spectroscopy," *Journal of Biomedical Optics* **10**(3): 031116 (2005).

[115] P. J. Caspers, G. W. Lucassen, R. Wolthuis, H. A. Bruining, and G. J. Puppels, "*In vitro* and *in vivo* Raman spectroscopy of human skin," *Biospectroscopy* **4**(5 Suppl): S31–S39 (1998).

[116] P. J. Caspers, G. W. Lucassen, H. A. Bruining, and G. J. Puppels, "Automated depth-scanning confocal Raman microspectrometer for rapid *in vivo* determination of water concentration profiles in human skin," *Journal of Raman Spectroscopy* **31**(8-9): 813–818 (2000).

[117] T. C. Bakker Schut, M. J. H. Witjes, H. J. C. M. Sterenborg, O. C. Speelman, J. L. N. Roodenburg, E. T. Marple, H. A. Bruining, and G. J. Puppels, "*In vivo* detection of dysplastic tissue by Raman spectroscopy," *Analytical Chemistry* **72**(24): 6010–6018 (2000).

[118] U. Utzinger, D. L. Heintzelman, A. Mahadevan-Jansen, A. Malpica, M. Follen, and R. Richards-Kortum, "Near-infrared Raman spectroscopy for *in vivo* detection of cervical precancers," *Applied Spectroscopy* **55**(8): 955–959 (2001).

[119] M. G. Shim, L. M. Song, N. E. Marcon, and B. C. Wilson, "*In vivo* near-infrared Raman spectroscopy: Demonstration of feasibility during clinical gastrointestinal endoscopy," *Photochemistry and Photobiology* **72**(1): 146–150 (2000).

[120] H. P. Buschman, E. T. Marple, M. L. Wach, B. Bennett, T. C. Schut, H. A. Bruining, A. V. Bruschke, A. van der Laarse, and G. J. Puppels, "*In vivo* determination of the molecular composition of artery wall by intravascular Raman spectroscopy," *Analytical Chemistry* **72**(16): 3771–3775 (2000).

[121] A. A. Oraevsky, S. L. Jacques, G. H. Pettit, I. S. Saidi, F. K. Tittel, and P. D. Henry, "XeCl laser ablation of atherosclerotic aorta - optical-properties and energy pathways," *Lasers in Surgery and Medicine* **12**(6): 585–597 (1992).

[122] A. J. Welch, C. Gardner, R. Richards-Kortum, E. Chan, G. Criswell, J. Pfefer, and S. Warren, "Propagation of fluorescent light," *Lasers in Surgery and Medicine* **21**(2): 166–178 (1997).

[123] J. R. Mourant, T. Fuselier, J. Boyer, T. M. Johnson, and I. J. Bigio, "Predictions and measurements of scattering and absorption over broad wavelength ranges in tissue phantoms," *Applied Optics* **36**(4): 949–957 (1997).

[124] J. M. Schmitt and G. Kumar, "Optical scattering properties of soft tissue: A discrete particle model," *Applied Optics* **37**(13): 2788–2797 (1998).

[125] W. H. Lawton, E. A. Sylvestre, and B. J. Youngferraro, "Statistical comparison of multiple analytic procedures - application to clinical-chemistry," *Technometrics* **21**(4): 397–409 (1979).

[126] A. S. Haka, K. E. Shafer-Peltier, M. Fitzmaurice, J. Crowe, R. R. Dasari, and M. S. Feld, "Diagnosing breast cancer by using Raman spectroscopy," *Proceedings of the National Academy of Sciences of the United States of America* **102**(35): 12371–12376 (2005).

[127] J. T. Motz, *Development of* in vivo *Raman spectroscopy of atherosclerosis*, Thesis Ph.D. – Harvard-MIT Division of Health Sciences and Technology, Massachusetts Institute of Technology (2003).

[128] L. Laifer, K. O'Brien, M. Stetz, G. Gindi, T. Garrand, and L. Deckelbaum, "Biochemical basis for the difference between normal and atherosclerotic arterial fluorescence," *Circulation* **80**(6): 1893–1901 (1989).

[129] J. J. Baraga, R. P. Rava, P. Taroni, C. Kittrell, M. Fitzmaurice, and M. S. Feld, "Laser induced fluorescence spectroscopy of normal and atherosclerotic human aorta using 306-310 nm excitation," *Lasers in Surgery and Medicine* **10**(3): 245–261 (1990).

[130] M. L. Higuchi, P. S. Gutierrez, H. G. Bezerra, S. A. Palomino, V. D. Aiello, J. M. Silvestre, P. Libby, and J. A. Ramires, "Comparison between adventitial and intimal inflammation of ruptured and nonruptured atherosclerotic plaques in human coronary arteries," *Arquivos Brasileiros de Cardiologia* **79**(1): 20–24 (2002).

[131] O. R. Scepanovic, M. Fitzmaurice, J. A. Gardecki, G. Angheloiu, S. Awasthi, J. T. Motz, J. R. Kramer, R. R. Dasari, and M. S. Feld, "Detection of morphological markers of vulnerable atherosclerotic plaque using multimodal spectroscopy," *Journal of Biomedical Optics* **11**(2): 021007 (2006).

[132] B. Chance, N. Graham, and V. Legallais, "Low-temperature trapping method for cytochrome-oxidase oxygen intermediates," *Analytical Biochemistry* **67**(2): 552–579 (1975).

[133] G. M. Palmer, C. L. Marshek, K. M. Vrotsos, and N. Ramanujam, "Optimal methods for fluorescence and diffuse reflectance measurements of tissue biopsy samples," *Lasers in Surgery and Medicine* **30**(3): 191–200 (2002).

[134] N. Ramanujam, R. Richards-Kortum, S. Thomsen, A. Mahadevan-Jansen, M. Follen, and B. Chance, "Low temperature fluorescence imaging of freeze-trapped human cervical tissues," *Optics Express* **8**(6): 335–343 (2001).

[135] A. J. Berger and M. S. Feld, "Analytical method of estimating chemometric prediction error," *Applied Spectroscopy* **51**(5): 725–732 (1997).

[136] T.-W. Koo, *Measurement of blood analytes in turbid biological tissue using near-infrared Raman spectroscopy*, Thesis Ph.D. – Deptartment of Mechanical Engineering, Massachusetts Institute of Technology (2001).

[137] H. L. T. Lee, P. Boccazzi, N. Gorret, R. J. Ram, and A. J. Sinskey, "*In situ* bioprocess monitoring of Escherichia coli bioreactions using Raman spectroscopy," *Vibrational Spectroscopy* **35**(1-2): 131–137 (2004).

[138] S. M. Kay, *Fundamentals of statistical signal processing*, Prentice-Hall signal processing series (PTR Prentice-Hall, Englewood Cliffs, N.J., 1993).

[139] R. Manoharan, J. J. Baraga, M. S. Feld, and R. P. Rava, "Quantitative histochemical analysis of human artery using Raman-spectroscopy," *Journal of Photochemistry and Photobiology B-Biology* **16**(2): 211–233 (1992).

[140] J. F. Brennan, T. J. Romer, R. S. Lees, A. M. Tercyak, J. R. Kramer, and M. S. Feld, "Determination of human coronary artery composition by Raman spectroscopy," *Circulation* **96**(1): 99–105 (1997).

[141] D. W. Marquardt, "Generalized inverses, ridge regression, biased linear estimation, and nonlinear estimation," *Technometrics* **12**(3): 591–612 (1970).

[142] J. H. Kalivas, "Variance-decomposition of pure-component spectra as a measure of selectivity," *Journal of Chemometrics* **3**: 409–418 (1989).

[143] R. A. Arndt and M. H. MacGregor, "Nucleon-nucleon phase shift analyses by chi-squared minimization," in B. Adler, S. Fernback, and M. Rotenberg (editors), "Methods in Computational Physics," 253–296 (Academic Press, New York, 1966).

[144] J. Zhao, "Image curvature correction and cosmic removal for high-throughput dispersive Raman spectroscopy," *Applied Spectroscopy* **57**(11): 1368–1375 (2003).

[145] I. Osticioli, A. Zoppi, and E. M. Castellucci, "Fluorescence and Raman spectra on painting materials: Reconstruction of spectra with mathematical methods," *Journal of Raman Spectroscopy* **37**(10): 974–980 (2006).

[146] A. Cao, A. K. Pandya, G. K. Serhatkulu, R. E. Weber, H. Dai, J. S. Thakur, V. M. Naik, R. Naik, G. W. Auner, R. Rabah, and D. C. Freeman, "A robust method for automated background subtraction of tissue fluorescence," *Journal of Raman Spectroscopy* **38**(9): 1199–1205 (2007).

[147] O. R. Scepanovic, K. L. Bechtel, A. S. Haka, W. C. Shih, T. W. Koo, A. J. Berger, and M. S. Feld, "Determination of uncertainty in parameters extracted from single spectroscopic measurements," *Journal of Biomedical Optics* **12**(6): 064012 (2007).

[148] G. J. Puppels, T. C. Bakker Schut, P. J. Caspers, R. Wolthuis, A. van Aken, A. van der Laarse, H. A. Bruining, H. P. J. Buschman, M. G. Shim, and B. Wilson, "*In vivo* Raman spectroscopy," in I. R. Lewis and H. G. M. Edwards (editors), "Handbook of Raman Spectroscopy," 549–574 (Dekker, New York, 2001).

[149] R. L. P. van Veen, W. Verkruysse, and H. J. C. M. Sterenborg, "Diffuse-reflectance spectroscopy from 500 to 1060 nm by correction for inhomogeneously distributed absorbers," *Optics Letters* **27**(4): 246–248 (2002).

[150] R. O. Duda, P. E. Hart, and D. G. Stork, *Pattern classification* (Wiley, New York, 2001).

[151] D. Aslanian, H. Vainer, and J. P. Guesdon, "Thermotropic state transition in isolated platelet membranes studied by Raman spectroscopy," *European Journal of Biochemistry* **131**(3): 555–558 (1983).

[152] M. Jelinek, R. Cristescu, T. Kocourek, V. Vorlicek, J. Remsa, L. Stamatin, D. Mihaiescu, I. Stamatin, I. N. Mihailescu, and D. B. Chrisey, "Thin films growth in MAPLE; application to fibrinogen," *Journal of Physics: Conference Series* **59**: 22–27 (2007).

[153] R. Y. Ball, J. P. Bindman, K. L. H. Carpenter, and M. J. Mitchinson, "Oxidized low-density-lipoprotein induces ceroid accumulation by murine peritoneal-macrophages *in vitro*," *Atherosclerosis* **60**(2): 173–181 (1986).

[154] P. Gupta, A. A. Soyombo, A. Atashband, K. E. Wisniewski, J. M. Shelton, J. A. Richardson, R. E. Hammer, and S. L. Hofmann, "Disruption of PPT1 or PPT2 causes neuronal ceroid lipofuscinosis in knockout mice," *Proceedings of the National Academy of Sciences of the United States of America* **98**(24): 13566–13571 (2001).

[155] P. J. Caspers, G. W. Lucassen, and G. J. Puppels, "Combined *in vivo* confocal Raman spectroscopy and confocal microscopy of human skin," *Biophysical Journal* **85**(1): 572–580 (2003).

[156] C. H. Yang, "Molecular contrast optical coherence tomography: A review," *Photochemistry and Photobiology* **81**(2): 215–237 (2005).